Department of Physics
Institute of Nuclear Physics

Master Thesis

Determination of the Branching Ratio of the Decay $\eta_c \to \eta' K^+ K^-$ and Search for Glueball Content in $K^+ K^-$ Intermediate States at BESIII

Name: Anja Brüggemann
First Supervisor: Apl. Prof. Dr. Alfons Khoukaz
Second Supervisor: Apl. Prof. Dr. Christian Klein-Bösing
Date of Submission: 27th July 2021

Contents

1 Introduction

Since ancient times people have dealt with the question of the fundamental constituents of our surrounding matter. In the 5th century before Christ, Leucippus and its student Democritus developed a concept of invisible, infinite small and indivisible particles as the fundamental constituents of matter and called them "atomos" (ancient Greek for indivisible). However, the atomic theory did not gain wide acceptance until increasing experimental evidence were found in the 19th century. [1] Furthermore, with the discovery of the electron by Thomson in 1897 [2, 3] and the results of Rutherford's scattering experiments in 1911 [4] the modern picture of the atom found its beginning. An atom is composed of a dense nucleus that is surrounded by an electron cloud. The presumption, that the nucleus itself is built up of sub-constituents called nucleons, was confirmed as Chadwick discovered the neutron in 1932 [5]. Thus, in the 1930s the two nucleons proton and neutron as well as the electron and neutrino, that was postulated by Pauli in 1930 [1], were considered as the four fundamental elementary particles. But this picture was soon after proved to be incomplete.
In numerous experiments at particle accelerators and colliders since the 1950s more and more "fundamental" particles were discovered and called the "particle zoo" [6]. However, due to their large number they were soon expected not to be elementary but rather to have an inner structure. Via the quark model, which was developed by Gell-Mann in the 1960s [7], they were classified into compositions of quarks and denoted as hadrons, soon after. The conventional quark model distinguished hadrons either composed of a quark-antiquark pair (mesons), or built up of three quarks (baryons), like proton and neutron. Meanwhile, it has been proved, that the strong interaction effects the binding of quarks into hadrons. The underlying theory is quantum chromodynamics QCD, whose constituents are quarks and gluons. Both carry so called color charge. The gluons mediate the strong interaction between quarks and themselves. Furthermore, only colour neutral compound systems of quarks (and gluons) are expected. [8] Thus, due to the gluon self-interaction and the constraint of color neutrality a couple of further hadron states besides mesons and baryons are predicted via QCD, that lie beyond the conventional quark model. QCD suggests for example hadrons built up of four quarks (tetraquarks), or hadrons that solely incorporate gluons (glueballs). Also mixed states between a conventional hadron and a glueball are supposed to exist. These complex systems are called exotic hadrons. However, their theoretical description and experimental investigation is still challenging. [9]
Thus, one main focus of current experimental particle physics is the study of hadrons and the search for exotic candidates. Several experiments, like the BESIII experiment at the electron-positron collider BEPCII in Beijing, China, have already provided important research results and contributions in (exotic) hadron spectroscopy. For example, recently in 2021 the heavy tetraquark meson state $Z_{cs}(3985)$ has been found at BESIII [10].
However, also in the light meson sector below 2 GeV/c^2 highly interesting exotic candidates have been found, that are supposed to include in particular admixtures of the lightest predicted glueball. Here, especially the $f_0(1370)$, $f_0(1500)$ and $f_0(1710)$ resonances must be mentioned, as they lie in the same mass region as the predicted glueball. The available experimental and theoretical studies provide controversial results. Some suggest the $f_0(1500)$ to be mostly the glueball, others favour the $f_0(1710)$. [9]
Experimentally, it is a common approach to search for these glueball candidates in gluon-rich environments of decaying mesons, like the η_c meson decaying via two gluons into hadrons. An example is the mesonic reaction $\eta_c \to \eta' K^+ K^-$ that is studied in this thesis. It offers a promising experimental access to investigate the three f_0 resonances, as they are possible intermediate states, that decay into the K^+K^- system.
Furthermore, a theoretical link between decays of the type $\eta_c \to \eta' f_0$ and the possible glueball content of the $f_0(1370)$, $f_0(1500)$ and $f_0(1710)$ states has already been established via several mixing matrices [11]. Thus, the comparison of experimental results concerning the f_0 contributions to the

K^+K^- system with the theory predictions might provide a further hint for answering the question whether one of the three resonances is mainly a glueball.
Moreover, the analysis of the $\eta_c \to \eta' K^+ K^-$ reaction is additionally motivated by the aspect, that the corresponding η_c branching ratio is still unlisted in the particle data group PDG database [12]. However, theoretical predictions for the branching ratio are already available [11].
Thus, the analysed η_c decay in this work is two-side motivated and will be studied using the world's largest J/ψ data sample provided by the BESIII experiment by exploiting the radiative J/ψ decay into $\gamma\eta_c$. A partial wave analysis is carried out to determine the branching ratio of the reaction $\eta_c \to \eta' K^+ K^-$ and to qualitatively investigate intermediate states decaying into K^+K^-. The final evaluation of the experimental results in comparison with the theory predictions provides a first hint regarding possible exotic content in the $f_0(1370)$, $f_0(1500)$ and $f_0(1710)$ resonances and might provide a framework for further studies of related η_c decay modes.

2 Theory

The Standard Model of particle physics describes the fundamental constituents of our surrounding matter, known as leptons and quarks, and their interactions with each other. Three fundamental interactions are united, the electromagnetic, weak and strong force. Each is mediated by the exchange of gauge bosons, that couple to the interaction specific charge. Whereas the electromagnetic force couples to the electric charge of particles via the exchange of a photon, the weak interaction is mediated by the heavy W^+, W^- or Z^0 bosons. [6]
However, the underlying force of the decay, that is studied in this work, is the strong interaction. It couples via gluons to the color charge of quarks and hence, explains the binding of quarks into hadrons within the quark model [6]. Thus, starting with a short introduction into the concept of the quark model in section 2.1, followed by the consideration of mesons as a subtype of hadrons in section 2.2, the fundamental theoretical nature of the studied mesonic decay can be understood.
Additionally, the analysis is based on theoretical predictions presented in section 2.3. They will be compared to the experimental results, which are obtained using the analysis technique partial wave analysis. Hence, in section 2.4 a short introduction into partial wave analysis is given.

2.1 Quark Model

The underlying theory of the strong interaction is **Q**uantum **C**hromo**D**ynamics QCD. Its constituents are certain elementary fermions and gauge bosons, known as quarks and gluons. [8]
Gluons are bosons with spin 1 that mediate the strong interaction between quarks, whereby they couple on the quarks' so called color charge, which can be either **r**ed, **b**lue or **g**reen. Since gluons carry colour charge combinations themselves they also interact with each other, which is known as gluon self-interaction. Eight massless gluons are predicted via QCD, whereas a set of six quarks is known so far, that includes in ascending mass order the **u**p u, **d**own d, **s**trange s, **c**harm c, **b**ottom b and **t**op t quark. [6, 8, 13, 14]
Quarks are fermions, that carry spin 1/2, and are distinguished via their flavor quantum numbers I_3, S, C, B and T. The third component I_3 of the isospin is the half-integer flavor quantum number corresponding to the u and d quark. The strangeness S, charmness C, bottomness B and topness T are the flavor quantum numbers of the name-giving s, c, b and t quark flavors, respectively. Besides the flavor quantum numbers, quarks carry an electric charge Q of one or two thirds. The quarks' charges as well as their flavor quantum numbers are summarised in Table 1, whereby the sign of each flavor quantum number is chosen by convention to be the same as for the electric charge. [13]

	Quarks					
	u	d	c	s	t	b
Electric Charge Q	$+\frac{2}{3}$	$-\frac{1}{3}$	$+\frac{2}{3}$	$-\frac{1}{3}$	$+\frac{2}{3}$	$-\frac{1}{3}$
Third Isospin Component I_3	$+\frac{1}{2}$	$-\frac{1}{2}$	0	0	0	0
Charmness C	0	0	1	0	0	0
Strangeness S	0	0	0	-1	0	0
Topness T	0	0	0	0	1	0
Bottomness B	0	0	0	0	0	-1

Table 1: The electric charge Q and flavor quantum numbers (I_3, C, S, T, B) of the six known quarks up u, down d, charm c, strange s, top t and bottom b. [13]

In addition, there exists a complementary antiquark to each quark with opposite charge-like quantum numbers (Q, I_3, S, C, B and T), but otherwise carrying the same properties. [6]
However, no isolated, free quark has been observed so far. Instead, it is widely accepted that quarks

only exist in colour neutral, compound systems. These are called hadrons, whose structure and properties are described within the generic quark model [8].
The confinement of quarks can be understood as an effect of the gluon self-interaction due to their colour charge and is explained in QCD. To realise colour neutrality either one colour (**r**ed, **b**lue or **g**reen) and its corresponding anti-colour ($\bar{\mathbf{r}}$ed, $\bar{\mathbf{b}}$lue, $\bar{\mathbf{g}}$reen) or all three colours have to be combined. Within the conventional quark model, the lightest hadrons consist of two quarks: a colour neutral quark-antiquark pair ($q\bar{q}$), which is known as a meson. An example for a meson is the charged pion π^+, which is composed of an u and $\overline{d}$ quark. Another important type of hadrons combines three quarks (qqq) of different colour charges and is called a baryon. The most prominent baryons are the nucleons: neutron and proton. Theoretically, colour neutral combinations of more than three quarks (like tetraquarks $qq\overline{qq}$), or hadrons composed solely of gluons (glueballs), or systems of a hadron and an excited gluon (hybrids) are also possible solutions in QCD [9]. Such hadrons have already been seen experimentally, however, their theoretical description remains still complex and controversial. They are called exotic hadrons. [6, 8, 14]
The studied reaction in this work considers the hadronic η_c decay to $\eta' K^+ K^-$, whereby all participating hadrons are mesons. Furthermore, within possible K^+K^- intermediate states of this reaction, exotic mesons are searched in particular. Thus, a more detailed description of (exotic) mesons is given in the following section.

2.2 Mesons

Mesons are bosons, that are composed of a quark-antiquark pair. Essentially, all colour neutral combinations of the u, d, s, c and b quarks and antiquarks form a meson. However, combinations with a t quark are expected not to exist in $q\bar{q}$ systems, since the top quark is too massive and hence short-living to form bound states. [6]
In the following, some essential properties of mesons, described by the quantum numbers J, P and C, are introduced, as they allow to characterise and classify mesons.
Since quarks and antiquarks carry spin 1/2, the spin S of a meson can either be $S = 1$ for parallel aligned quark spins or $S = 0$ for anti-parallel spins. If L is the relative orbital angular momentum between the two bound quarks, then the total angular momentum J of the meson is determined via the relation $|L - S| \leq J \leq |L + S|$ [8]. Furthermore, quarks carry the intrinsic parity $P = +1$ and antiquarks $P = -1$ per convention [6]. Therefore, being a multiplicative quantum number and following the Dirac equation, the parity of a $q\overline{q}$ system is given by $P = (-1)^{L+1}$ [8]. These are the eigenvalues of the parity operator for a fermion/antifermion system, whereby the parity operator corresponds to a spatial point reflection of the particle's wave function. A further property of mesons, which consist of a $q\overline{q}$ pair of the same flavor and hence, are neutral ($Q = 0$), is described by the quantum number C-parity or charge conjugation. It is given by $C = (-1)^{L+S}$ [8], which are the eigenvalues of the charge conjugation operator for neutral mesons. The charge conjugation operator transfers a particle into its antiparticle by inverting the signs of all charge-like quantum numbers. [6, 15]
Via the notation $J^{P(C)}$ mesons can be classified. Considering mesons with a vanishing orbital angular momentum $L = 0$, the so called pseudoscalar mesons with $J^{P(C)} = 0^{-(+)}$ (for $S = 0$) as well as the spin-excited vector mesons with $1^{-(-)}$ (for $S = 1$) are obtained. For $L = 1$ one gets the scalar mesons with $0^{+(+)}$ (for $S = 1$), the axial vector mesons with $1^{+(+)}$ (for $S = 1$) or $1^{+(-)}$ (for $S = 0$) and the tensor mesons with $2^{+(+)}$ (for $S = 1$). [8]

2.2.1 Pseudoscalar Mesons

The analysed decay $\eta_c \to \eta' K^+ K^-$ in this work includes solely pseudoscalar mesons with $J^{P(C)} = 0^{-(+)}$, whereby the η_c meson consists of a $c\bar{c}$ quark pair. These states are called charmonia and considered in more detail in section 2.2.2. The three η_c daughter particles K^+, K^- and η' are $q\bar{q}$ systems composed of the three lightest quarks u, d and s. Further candidates of these lightest pseudoscalar mesons are the η state, the three pions π^0 and $\pi^\pm$ and the two kaons K^0 and $\overline{K}^0$. Thus, in total nine pseudoscalar mesons are obtained as possible combinations of u, d, s quarks and antiquarks. [6]
Mesons are often arranged and visualised in so called $J^{P(C)}$ multiplets. In Figure 1 the corresponding $0^{-(+)}$ nonet of the nine lightest pseudoscalar mesons as a function of the meson's strangeness S and its third component of isospin I_3 is pictured. As can be seen, the $q\bar{q}$ combinations $|u\bar{u}\rangle$, $|d\bar{d}\rangle$ and $|s\bar{s}\rangle$ have the same quantum numbers strangeness and isospin I_3 equal to zero. Thus, they mix forming the physically observed mass eigenstates π^0, η and η'. [6]

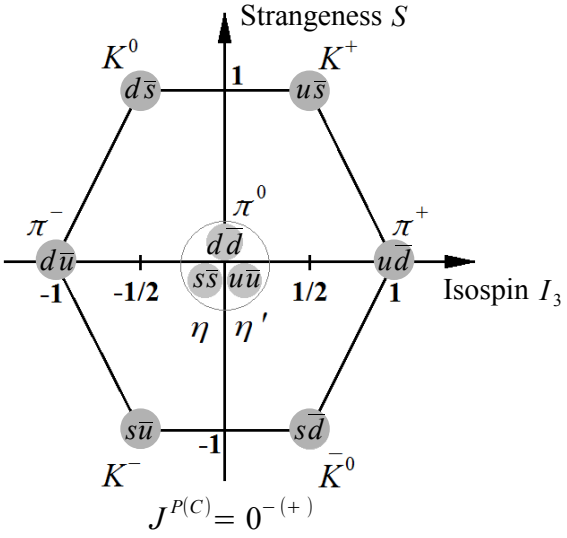

Figure 1: The pseudoscalar meson nonet with $J^{P(C)} = 0^{-(+)}$ that includes all mesons composed of the three lightest quarks u, d and s. The mesons are arranged concerning their strangeness S and their third component of isospin I_3. (Figure adapted from [16])

In Table 2 a detailed list of the lightest pseudoscalar mesons of concern in this work is given along with their mass, mean lifetime, quantum numbers $J^{P(C)}$ and special decay modes of interest.

2.2.2 Charmonia

The pseudoscalar η_c meson is classified also as a charmonium. Charmonia are composed of a heavy $c\bar{c}$ quark pair.
Due to the high mass of the c quark, the relative velocity between the c and $\bar{c}$ quark within a charmonium is approximately non-relativistic. Thus, the charmonium can be similarly described to the compound system of a hydrogen atom. A hydrogen atom consists of an electron that is bound to a proton via the electrostatic Coulomb potential $V_C \propto 1/r$, where r is the electron-proton distance.

Particle	**Mass** / MeV/c^2	**Mean Lifetime** / s	$J^{P(C)}$	**Decay Modes** (BR)
η'	957.78 ± 0.06	$(3.501 \pm 0.112) \cdot 10^{-21}$	0^{-+}	$\eta\pi^+\pi^-$ $(42.5 \pm 0.5)\%$ $\gamma\pi^+\pi^-$ $(29.5 \pm 0.4)\%$
η	547.862 ± 0.0017	$(5.025 \pm 0.192) \cdot 10^{-19}$	0^{-+}	$\gamma\gamma$ $(39.41 \pm 0.20)\%$
$K^{\pm}$	493.677 ± 0.016	$(1.238 \pm 0.002) \cdot 10^{-8}$	0^{-}	"detector stable"
$\pi^{\pm}$	139.5704 ± 0.0002	$(2.6033 \pm 0.0005) \cdot 10^{-8}$	0^{-}	"detector stable"
π^0	134.9768 ± 0.0005	$(8.52 \pm 0.18) \cdot 10^{-17}$	0^{-+}	$\gamma\gamma$ $(98.82 \pm 0.03)\%$

Table 2: Properties of selected pseudoscalar mesons. Besides the mass, mean lifetime and quantum numbers $J^{P(C)}$, also special decay modes of interest in this analysis along with their branching ratios are given. The indication "detector stable" is used for particles with mean lifetimes large enough to be directly measured in a particle detector. All values are taken from [12].

Solving the corresponding non-relativistic Schrödinger equation, the discrete energy eigenstates of the compound electron-proton system are obtained. [6]
Analogous considerations are possible for the charmonium $c\bar{c}$, whereby an additional potential term σr is taken into account. In sum, the Cornell potential [17] is received

$$V(r) = -\frac{\kappa}{r} + \sigma r \tag{1}$$

with the proportionality factors κ and σ, that are determined experimentally based on the so far known charmonia. The Coulomb like $-\frac{\kappa}{r}$ term of the Cornell potential dominates for small distances between the c and $\bar{c}$ quark, whereas for large distances the linear σr term leads to an attractive potential, that serves for the confinement of quarks in the charmonium, since $V(r \to \infty) \to \infty$. [6, 14]
Taking additionally relativistic corrections as well as the spin-spin and spin-orbit coupling between the quarks into account the discrete energy spectrum of the charmonium $c\bar{c}$ is obtained. It is pictured in Figure 2, whereby a single energy level is identified with a corresponding charmonium state.
The pseudoscalar η_c meson is the charmonium ground state with $J^{PC} = 0^{-+}$. The next heavier charmonium is the spin-excited vector meson J/ψ with $J^{PC} = 1^{--}$. In Table 3 important properties of the two charmonia are summarised.

Particle	**Mass** / MeV/c^2	**Mean Lifetime** / s	J^{PC}	**Decay Modes** (BR)
J/ψ	3096.900 ± 0.006	$(7.108 \pm 0.131) \cdot 10^{-21}$	1^{--}	$\gamma\eta_c$ $(1.7 \pm 0.4)\%$
η_c	2983.9 ± 0.5	$(2.057 \pm 0.045) \cdot 10^{-23}$	0^{-+}	$\eta' K^+K^-$ (seen [18])

Table 3: Properties of the two charmonia states J/ψ and η_c. Besides the mass, mean lifetime and quantum numbers J^{PC}, special decay modes of interest in this analysis along with their branching ratios are given, if known. All values are taken from [12].

The considered η_c reaction in this work results from a decaying J/ψ charmonium. Thus, in the following the production mode of the J/ψ charmonium, the analysis is based on, as well as the J/ψ decay into an η_c meson is described more precisely. Afterwards, the hadronic η_c decay into $\eta' K^+K^-$ is also considered in more detail.

Production of the J/ψ Charmonium and its Decay into an η_c Meson. The J/ψ charmonium can be effectively produced at electron positron colliders with center-of-mass energies above $\sqrt{s} > 3$ GeV, since the J/ψ state has an invariant mass of 3.0969 GeV/c^2 [12].

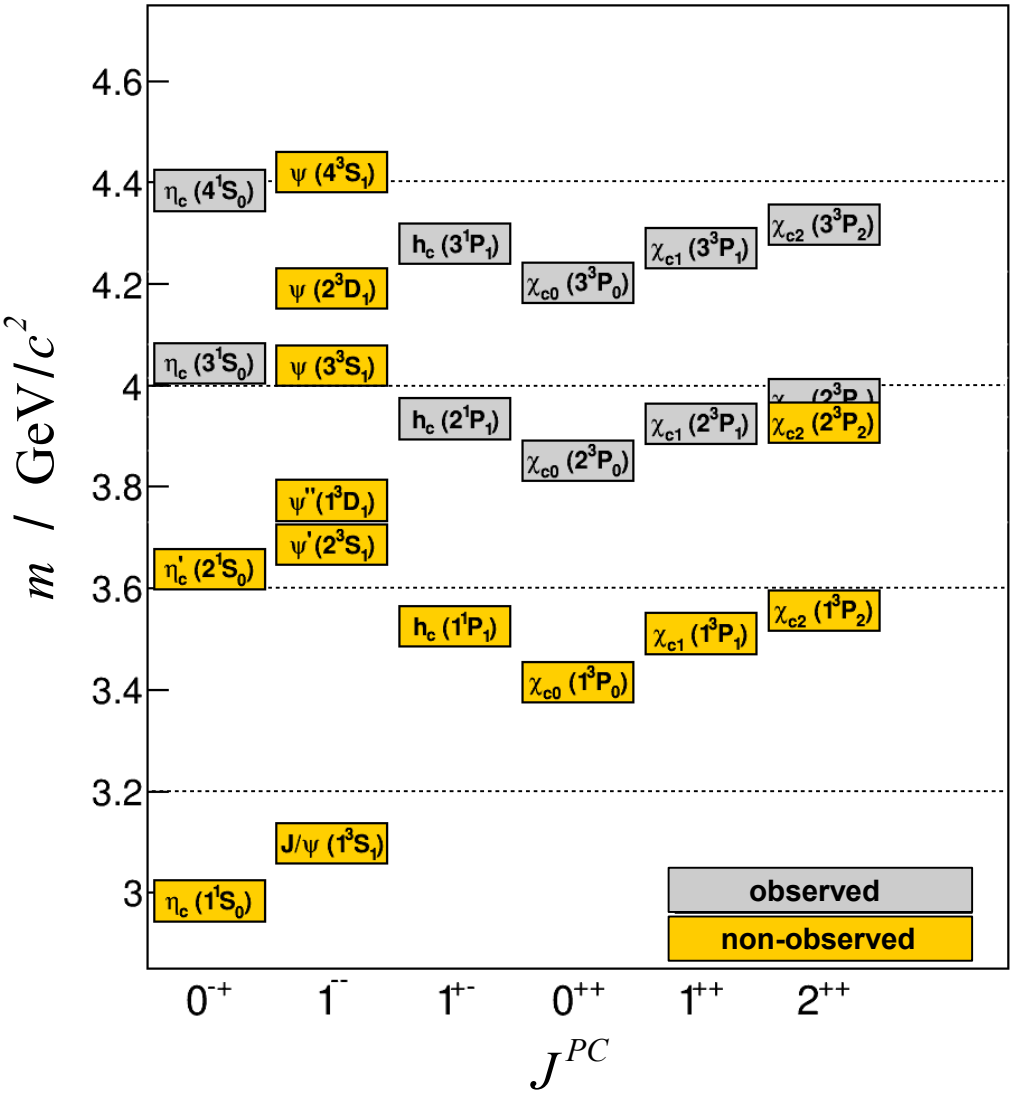

Figure 2: Charmonium spectrum as a function of the invariant mass m and the quantum numbers J^{PC}. The spectrum shows the theoretically predicted charmonium states within the quark model. The experimentally already confirmed states are coloured in yellow, the still non-observed ones in grey. (Based on the predictions in [19])

The colliding electrons and positrons annihilate into a virtual photon, that decays instantaneously into a pair of charged fundamental fermions f and $\overline{f}$, like a $c\bar{c}$ quark pair. Since the produced $c\bar{c}$ state has to carry the same quantum numbers as the virtual photon with $J^{PC} = 1^{--}$, only the vector charmonia, like the J/ψ charmonium, can be produced via the annihilation and coupling to a virtual photon within e^+e^- collisions (see Fig. 2). The production of η_c states that have $J^{PC} = 0^{-+}$ is impossible. [6, 14]
Nevertheless, a particular decay mode of the J/ψ offers an adequate access to the η_c meson.
Around 30% of the J/ψ decay modes are electromagnetic ones into hadrons or charged leptons. For instance, the charmonium ground state η_c is produced via a radiative magnetic dipole $M1$ transition

from a decaying J/ψ into $\gamma_r\eta_c$. [6]
The charmonia J/ψ (with $S = 1$) and η_c (with $S = 0$) have both a vanishing orbital angular momentum $L = 0$. Thus, it is $\Delta L = 0$ and $\Delta S = 1$ between the two states, which are the selection rules for magnetic $M1$ and electric $E1$ dipole radiation. Since, additionally, both charmonia carry the same negative parity $P = -1$, the J/ψ decays into an η_c meson through a magnetic $M1$ transition via a spin flip of one charm quark and the emission of a radiative photon γ_r. Furthermore, since the radiative photon energy E_{γ_r} depends on the magnetic dipole transition rate, the line shape of the invariant η_c mass is asymmetric. [6, 20]
The radiative J/ψ decay to $\gamma_r\eta_c$ is observed with a branching ratio of $(1.7 \pm 0.4)\%$ [12]. Hence, it offers an effective experimental access to η_c mesons. If a sufficiently large sample of J/ψ events is available, a large number of η_c mesons can be observed.

The η_c Decay into $\eta' K^+K^-$. Only around 60% of the η_c decay modes are known so far [12]. Besides the radiative reaction into two photons, the η_c charmonium decays via the strong interaction into at least two gluons, while conserving colour charge and parity. Afterwards the gluons form new hadrons. An example is the strong η_c decay into $\eta K\overline{K}$, whereby the notation includes the possible neutral kaon combinations K^+K^- and $K^0\overline{K}^0$ and hence, also K_SK_S and K_LK_L. The corresponding observed branching ratio is $(1.36 \pm 0.15)\%$ [12]. As the pseudoscalar mesons η and η' have the same quantum numbers and invariant masses of the same order of magnitude (see Tab. 2), the analogues decay mode $\eta_c \to \eta' K\overline{K}$ should be also observed with a branching ratio in the same order of 1.0%. However, the studied $\eta_c \to \eta' K^+K^-$ decay considers solely the K^+K^- kaon combination, which supposes a lower branching ratio by half, as for $\eta_c \to \eta' K\overline{K}$.

2.2.3 Scalar Mesons

Besides the considered charmonium states and the pseudoscalar mesons, also certain light scalar mesons with $J^{PC} = 0^{++}$ and invariant masses below 2 GeV/c^2 are of special interest here, namely the so called isoscalar[1] scalar f_0 resonances, that carry strangeness S and isospin I_3 equal to zero. Satisfying the conservation of CP and the total angular momentum J, they are possible intermediate states decaying into K^+K^- in the $\eta_c \to \eta' K^+K^-$ reaction as the K^+K^- system lies in the $1 - 2$ GeV/c^2 mass regime. [11]
However, the theoretical and experimental description and investigation of the scalar meson sector $0^{+(+)}$ is highly complex and controversial. Whereas some candidates are experimentally already well established, it is difficult to determine the properties of other ones. Furthermore, some are even supposed to have exotic content, since experimental data does not coincide with conventional $q\overline{q}$ models in these cases. [21]
So far five isoscalar scalar f_0 resonances below 2 GeV/c^2 have been found, which assumes more than one scalar $0^{+(+)}$ nonet to arrange them. In some scenarios two scalar nonets are supposed, whereby the lighter nonet contains the two resonances $f_0(500)$ and $f_0(980)$. [12, 21, 22]
Around 1.5 GeV/c^2 the three resonances $f_0(1370)$, $f_0(1500)$ and $f_0(1710)$ are observed and accomodated all together in the second scalar $0^{+(+)}$ nonet of higher masses. This nonet is composed of the triplet $a_0(1450)$, $a^{\pm}(1450)$, the excited kaons $K_0^*(1430)$, $\overline{K}_0^*(1430)$ and $K^{*\pm}(1430)$ and the three isoscalar resonances $f_0(1370)$, $f_0(1500)$ and $f_0(1710)$, as it is visualised in Figure 3. These are in total ten states and hence, one state is redundant, namely a f_0 resonance, since only two f_0 states are predicted to build with the triplet state $a_0(1450)$ the three states with strangeness and third component of isospin equal to zero. However, the existence of a redundant f_0 state in the mass region of 1.5 GeV/c^2 supports the suggestion, that at least one of them is mainly an exotic state.

[1] Mesons with a third component of isospin $I_3 = 0$ are denoted as isoscalar.

This aspect is considered in more detail in the following section 2.2.4. [22, 8, 21]

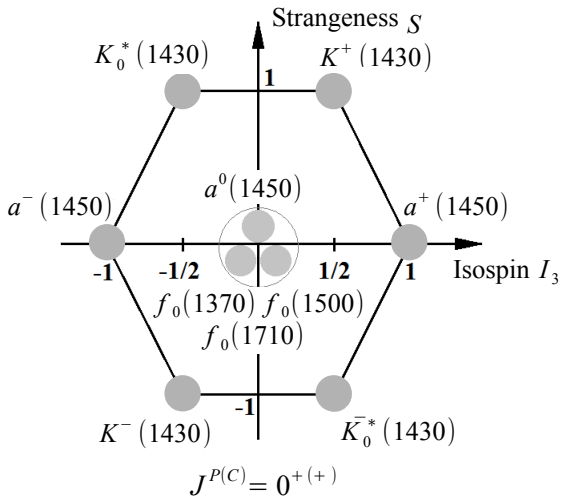

Figure 3: Supposed scalar meson nonet with $J^{P(C)} = 0^{+(+)}$ between 1 and 2 GeV/c^2. The mesons are arranged concerning their strangeness S and their third component of isospin I_3. (Figure adapted from [16])

2.2.4 Exotic Mesons

Within the static quark model a meson is defined as a colour neutral, bound $q\bar{q}$ system in general. But theoretically, meson-like multiquark combinations beyond the conventional $q\bar{q}$ states are also possible in QCD, like tetraquarks $qq\overline{qq}$ or six-quark states $qqq\overline{qqq}$. These states are called non-$q\bar{q}$ mesons or exotic mesons. Further types of exotic mesons arise as a result of the gluon self-interaction. QCD predicts so called glueballs G, that are built up solely of bound gluons. QCD solutions also predict hybrids $q\bar{q}g$, which contain an excited gluon g that is bound to a conventional meson. Furthermore, a glueball and meson state, that carry equal quantum numbers and have nearby masses, mix and form mixed states of $|q\bar{q}\rangle$ and $|G\rangle$. Within this work, in particular the lightest predicted glueball in QCD that mixes with light quark-antiquark states plays a role. [8, 9]
Via lattice QCD the mass of the lightest predicted glueball has been estimated to be about $(1.5 - 1.7)$ GeV/c^2 [23, 24, 25]. It includes two gluons gg and carries the quantum numbers $J^{PC} = 0^{++}$ with $I_3 = 0$. Thus, this isoscalar scalar glueball lies in the mass range of the isoscalar scalar resonances $f_0(1370)$, $f_0(1500)$ and $f_0(1710)$, that have the same quantum numbers. Therefore, the three resonances are possible candidates for carrying at least admixtures of this glueball. [9]
In Table 4 essential properties of the $f_0(1370)$, $f_0(1500)$ and $f_0(1710)$ mesons are summarised.
The broad resonance $f_0(1370)$ decays mainly into neutral pions [9], however, the decay mode into two kaons $K\overline{K}$ has also been seen [12]. The narrower resonance $f_0(1500)$ decays with a branching ratio of $(8.5 \pm 1.0)\%$ into a kaon pair $K\overline{K}$ [12], whereas the decays into two and four pions dominate significantly (around 85%) [12]. Unlike the also comparatively narrow resonance $f_0(1710)$, it decays mainly into two kaons $K\overline{K}$ [9]. Hence, as kaons carry strangeness, the $f_0(1710)$ resonance is naively supposed to contain mainly $s\bar{s}$ contribution. The other two resonances are presumably dominated by an $u\bar{u} + d\bar{d}$ content [9]. In different experiments, like BESIII, Belle, BaBar or LHCb, and in theoretical papers, like [26] or [27] these naive assumptions of the resonances' structure have been either approved or negated. If deviations to the predictions occur, the studied resonance is considered to

Particle	**Mass** / MeV/c^2	**Width** / MeV/c^2	J^{PC}	**Decay Modes** (BR)
$f_0(1370)$	1200 to 1500	200 to 500	0^{++}	$n(\pi\pi)$ (dominant [9]) $K\overline{K}$ (seen [12])
$f_0(1500)$	1506 ± 6	112 ± 9	0^{++}	4π $(48.9 \pm 3.3)\%$ $\pi\pi$ $(34.5 \pm 2.2)\%$ $K\overline{K}$ $(8.5 \pm 1.0)\%$
$f_0(1710)$	1704 ± 12	123 ± 18	0^{++}	$K\overline{K}$ (dominant [9]) $\pi\pi$ (seen [12])

Table 4: Properties of the three isoscalar scalar mesons $f_0(1370)$, $f_0(1500)$ and $f_0(1710)$. Besides the mass, width and quantum numbers J^{PC}, their decay modes into pion and kaon pairs along with their branching ratios are given, if known. All values are taken from [12].

be mainly gluonic. Often the $f_0(1500)$ is suggested to be mostly a glueball [28, 29], other results predict the $f_0(1710)$ to be (purely) the scalar glueball [26, 30]. Thus, further theoretical modelling is needed and experimental analyses, to clear up the resonances' content. [9]

Experimentally, it is a common approach to search for these (exotic) mesons in gluon-rich environments of decaying mesons. This is done in this work via the investigation of intermediate states decaying into K^+K^- within the gluon-rich strong decay of the η_c meson into the hadrons $\eta' K^+K^-$. Furthermore, corresponding experimentally results are directly comparable with theoretical predictions, which are presented in the following section 2.3.

2.3 Theoretical Predictions for the Reaction $\eta_c \to \eta' KK$

In [11] the authors W. I. Eshraim and C. S. Fisher study theoretically the η_c decay to $\eta' K\overline{K}$ amongst others and estimate for instance the corresponding branching ratio. Additionally, possible glueball content in intermediate states decaying to $K\overline{K}$ is analysed. For that, the authors theoretically establish a link between decays of the type $\eta_c \to \eta' f_0$ and the glueball content of the three resonances $f_0(1370)$, $f_0(1500)$ and $f_0(1710)$ decaying into $K\overline{K}$. They assume the f_0 resonances to be a mixing of the lightest scalar glueball $|gg\rangle$ and the quark-antiquark states $\left|u\bar{u} + d\bar{d}\right\rangle / \sqrt{2}$ and $|s\bar{s}\rangle$. Additionally, they use the mixing matrix U_1, which has been determined via the extended Linear Sigma Model in [30] as its best result. The extended Linear Sigma Model is a $U(N_f)_r \times U(N_f)_l$ symmetric, effective model[2] (here $N_f = 4$) that is based on a global chiral symmetry and the classical dilation symmetry. The resulting mixing matrix U_1 is given by

$$\begin{pmatrix} |f_0(1710)\rangle \\ |f_0(1500)\rangle \\ |f_0(1370)\rangle \end{pmatrix} = U_1 \begin{pmatrix} |gg\rangle \\ |s\bar{s}\rangle \\ \frac{|u\bar{u}+d\bar{d}\rangle}{\sqrt{2}} \end{pmatrix}, \quad U_1 = \begin{pmatrix} 0.93 & 0.26 & -0.27 \\ -0.17 & 0.94 & 0.30 \\ -0.33 & 0.24 & -0.91 \end{pmatrix}. \tag{2}$$

The relation (2) predicts, that obviously the resonance $f_0(1710)$ is identified for the most part with the scalar glueball. But there are other possible mixing matrices taken from other references [29, 31], which the authors consider for comparison:

[2] It enables the description of several (pseudo)-scalar and (axial)-vector mesons as well as the estimation of masses and (strong) decays of open and hidden charm mesons, like the hidden charm mesons η_c and χ_{c0}, which are investigated in [11]. Additionally, the two lightest scalar and pseudoscalar glueballs are implemented, which are built up of two gluons, respectively.

$$U_2 = \begin{pmatrix} 0.36 & 0.93 & 0.09 \\ -0.84 & 0.35 & -0.41 \\ 0.40 & -0.07 & -0.91 \end{pmatrix}, \quad U_3 = \begin{pmatrix} 0.859 & 0.302 & 0.413 \\ -0.128 & 0.908 & -0.399 \\ -0.495 & 0.290 & 0.819 \end{pmatrix},$$
$$U_4 = \begin{pmatrix} -0.06 & 0.97 & -0.24 \\ 0.89 & -0.06 & -0.45 \\ 0.45 & 0.24 & 0.86 \end{pmatrix}, \quad U_5 = \begin{pmatrix} -0.68 & 0.67 & -0.30 \\ 0.49 & 0.72 & -0.49 \\ 0.54 & 0.19 & 0.81 \end{pmatrix}. \tag{3}$$

Considering all five matrices U_1 - U_5 the mixing between the lightest scalar glueball and the quark-antiquark states is quite different. For example, the matrices U_1 and U_3 predict that the resonance $f_0(1710)$ is mainly a glueball. However, according to the mixing matrices U_2 and U_4 the scalar glueball content dominates significantly in the resonance $f_0(1500)$.

Using the mixing matrix U_1 the authors determine via the extended Linear Sigma Model the branching ratios $BR_{\eta_c \to f_0 \eta'}$ for the three resonances $f_0(1370)$, $f_0(1500)$ and $f_0(1710)$. The estimated values are summarised in Table 5, which also includes the resulting branching ratios of the other four mixing matrices.

Decay channel	U_1 ([30])	U_2 ([29])	U_3 ([31])	U_4 ([31])	U_5 ([31])
$BR_{\eta_c \to f_0(1370)\eta'}$ / %	$6.25 \cdot 10^{-1}$	$6.25 \cdot 10^{-1}$	$6.25 \cdot 10^{-1}$	$6.25 \cdot 10^{-1}$	1.25
$BR_{\eta_c \to f_0(1500)\eta'}$ / %	$3.13 \cdot 10^{-1}$	$3.13 \cdot 10^{-2}$	$3.13 \cdot 10^{-5}$	$1.56 \cdot 10^{-1}$	$9.38 \cdot 10^{-2}$
$BR_{\eta_c \to f_0(1710)\eta'}$ / %	$1.25 \cdot 10^{-2}$	$1.25 \cdot 10^{-1}$	$1.56 \cdot 10^{-1}$	$1.88 \cdot 10^{-2}$	$2.81 \cdot 10^{-1}$

Table 5: Branching ratios of the η_c decays to $\eta' f_0$ for the three resonances $f_0(1370)$, $f_0(1500)$ and $f_0(1710)$. [11]

As can be seen in Table 5 the decay mode $\eta_c \to f_0(1500)\eta'$ is highly sensitive to the mixing matrix with deviations up to four orders of magnitudes between the different matrices. The other two η_c decay channels show much less sensitivity with differences not more than one order of magnitude. The sensitivity to the mixing matrix and the results for the branching ratios for each mixing matrix provide an access for the comparison with results of experimental data analysis. This access will be exploited in this work by analysing resonances in the invariant K^+K^- mass spectrum of experimental data.

In [11] the authors also present a theoretical estimation for the η_c decay to $\eta' K\overline{K}$ of

$$BR^{\text{theo}}_{\eta_c \to \eta' K\bar{K}} = (1.34 \pm 0.13)\%. \tag{4}$$

The prediction is also calculated via the extended Linear Sigma Model, whereby the authors consider different η_c decays. As the model provides results with partly high systematic model uncertainties for the considered η_c decays, the predicted value has to be understood as an order of magnitude prediction.

2.4 Partial Wave Analysis

The investigation of resonances in the K^+K^- system and the determination of the branching ratio of the decay $\eta_c \to \eta' K^+ K^-$ in this work is based on **P**artial **W**ave **A**nalysis PWA.
PWA is a commonly used method for the determination and identification of possible short-lived intermediate states of a decaying particle, since it gives access to the properties of contributing resonances. It is based on the partial wave decomposition. The amplitude of a process $a + b \to c + d$

or $a \to b + c$ can be described by a partial wave expansion. [32, 33]
In this analysis, partial waves from the decay of a resonance a into two daughter particles b and c is identified by the total angular momentum J of a, the spin S of the system $b + c$ and the orbital angular momentum L between b and c.
For the implementation of the PWA approach a description of the decay amplitude of the $a \to b + c$ process as a series expansion of sub-decay amplitudes is required. But before this formalism is presented, a short theoretical introduction of partial waves via scattering processes is given (sect. 2.4.1). Afterwards the isobar model for the description of a decay process is presented (sect. 2.4.2). This model is used to construct the angular part of a decay amplitude within the helicity formalism (sect. 2.4.3). The dynamical part of the amplitude is considered in section 2.4.4. At the end of this section in 2.4.5 the basic, total decay amplitude the PWA is based on in this work, is presented.

2.4.1 Partial Waves and the Scattering Amplitude

The partial wave approach is based on scattering theory. Consider a free spinless particle with mass m_1 and momentum $\vec{p}$ that moves in z direction. It is described by the incoming plane wave function $\psi_i = e^{ikz}$ with the wave vector $\vec{k} = \vec{p}/\hbar$. On a second spinless particle with mass m_2, the incoming particle is scattered, whereby the scattering process can be described using a spherically symmetric scattering potential $V(r)$. The outgoing wave function ψ_f is determined by solving the time-independent Schrödinger equation [15, 32]

$$-\frac{\hbar^2}{2\mu^2}\Delta^2\psi_f + V(r)\psi_f = E\psi_f \tag{5}$$

with $\mu = m_1 m_2/(m_1 + m_2)$ being the reduced mass. The difference between the incoming wave ψ_i and the scattered, outgoing wave ψ_f defines the scattering wave function ψ_s

$$\psi_s = \psi_f - \psi_i. \tag{6}$$

In order to further determine ψ_s the incoming wave function is decomposed using the Legendre polynomials $P_l(\cos\theta)$ and the radial functions $U_l(r)$. Then ψ_i is given by

$$\psi_i = \sum_{l=0}^{\infty} U_l(r) P_l(\cos\theta), \tag{7}$$

where θ is the scattering angle between the particles. Using an equation for the functions $U_l(r)$ that provides a dependence on the l-dependent scattering phases δ_l and inelasticities η_l, one gets with equation (6) and (7) for the scattered wave function

$$\begin{aligned}\psi_s &= \sum_{l=0}^{\infty}(2l+1)\frac{e^{ikr}}{kr}T_l(\delta_l,\eta_l)P_l(\cos\theta)\\ &\equiv f(\theta)\frac{e^{ikr}}{r}\end{aligned} \tag{8}$$

with the so called scattering amplitude

$$f(\theta) = \frac{1}{k}\sum_{l=0}^{\infty}(2l+1)T_l(\delta_l,\eta_l)P_l(\cos\theta). \tag{9}$$

Thus, ψ_s is expanded into an infinite number of partial waves with regard to the relative orbital angular momentum l between the two scattering particles. Furthermore, from equation (8) and (9) follows that the crucial physical information about the two-particle scattering process is contained in the scattering amplitude $f(\theta)$. In addition, the scattering amplitude itself is defined as a series expansion of factorized amplitudes $T_l(\delta_l, \eta_l)P_l(cos\theta)$, which are composed of an angular part (described by the Legendre polynomials P_l) and a dynamical part (described by T_l), respectively.[15] [32, 33]
This description of a two-particle scattering process via partial waves also serves for the description of a two-body decay process and thus the determination of the line shape of the decaying particle [32]. In this term equation (9) is understood as an expansion of a two-particle decay amplitude $f(\theta)$ into sub-decay amplitudes $T_l(\delta_l, \eta_l)P_l(cos\theta)$, whereby the dynamical and angular contributions $T_l(\delta_l, \eta_l)$ and $P_l(cos\theta)$ have to be evaluated. In simplified terms, this is done via the PWA method, expanded to particles with non-zero spin. But for that, an appropriate formalism for the amplitude $f(\theta)$ is required, that enables the practical application of the PWA method. This formalism will be briefly derived in the following, starting with the isobar model, that is used for the description of a decay chain. It has been empirical proved to be particularly appropriate for performing PWA studies. [32]

2.4.2 The Isobar Model

Within the isobar model a decay process is split subsequently into solely two-body decays, that factorize. Each two-body reaction is assigned a node in the decay chain and each node is described by a sub-decay amplitude. These amplitudes all have the same structure. They are composed of an angular part and a dynamical part (see eq. (9)). The product of the sub-decay amplitudes of all nodes provides the total amplitude of the decay chain, whereby a summation over all unobserved quantum numbers has to be taken into account. [32]
In this work the angular part of all two-body decay amplitudes will be described in the so called helicity formalism, which will be introduced next. The dynamical part will be considered afterwards.

2.4.3 Angular Amplitudes in the Helicity Formalism

The helicity formalism is one of the three basic spin-projection formalisms for describing the angular part of a two-body decay amplitude, beside the canonical and transversity ones [32]. All three formalisms define the quantisation axis (in general the z-axis) into a certain direction and utilize specific rotations in order to formulate the angular amplitude of a two-body decay. Within the helicity formalism the quantisation axis, respectively the spin axis is quantized along the axis of the direction of motion of a particle. Thus, the helicity λ that describes the projection of the particle's total spin $\vec{J}$ onto the direction of motion $\vec{p}$ of the particle

$$\lambda = \vec{J} \cdot \frac{\vec{p}}{|\vec{p}|} \tag{10}$$

becomes diagonal and invariant. [6, 32, 34]
In order to define the angular amplitude of a two-body decay in the helicity formalism, two-particle states are required, which are derived from products of one-particle states [32]. Thus, the construction of an one-particle state in the helicity frame is presented in the following.

One-Particle States in the Helicity Formalism. In general a particle at rest with spin j and the spin projection m onto the quantisation axis is assigned the vector $|j, m\rangle$. By applying a Lorentz

transformation that is composed of a sequence of so called Lorentz boosts $\hat{l}(\vec{p})$ and rotations $\hat{r}(\alpha, \beta, \gamma)$ (with the Euler angles α, β and γ) the particle in the rest frame is transformed into another frame, where it has the momentum $\vec{p}$ [32, 33]. A single rotation of the state $|j, m\rangle$ is given by [35]

$$\hat{r}(\alpha, \beta, \gamma) \, |j, m\rangle = \sum_{m'} D^{j}_{mm'}(\alpha, \beta, \gamma) \, |j, m'\rangle \tag{11}$$

with the Wigner-D-matrices

$$D^{j}_{mm'}(\alpha, \beta, \gamma) = \langle j, m' | \, \hat{r}(\alpha, \beta, \gamma) \, |j, m\rangle = e^{-im'\alpha} \; d^{j}_{m'm}(\beta) \; e^{-im\gamma}. \tag{12}$$

The $d^{j}_{m'm}$ are the Wigner-d-matrices which are tabulated for instance in [36].
Transforming the one-particle state into the helicity frame explicitly, the helicity λ is used as spin projection. Thus, the one-particle state at rest is assigned the vector $|j, \lambda\rangle$. Additionally, the Lorentz boost $\hat{l}_z(\vec{p})$ is chosen in z direction, which is the quantisation axis. Thus, the Euler angle γ, that rotates a state around the z-axis, can be set to $\gamma = 0$, whereas $\alpha = \varphi$ and $\beta = \vartheta$ are set to the azimuthal and polar angles. The transformation is done by applying at first the rotation $\hat{r}(\varphi, \vartheta, 0)$, which rotates the z-axis into the particle's direction of movement $\vec{p}$. Secondly the Lorentz boost $\hat{l}_z(\vec{p})$ is applied. Thus, the direction of movement of the particle is always aligned parallel to the z direction. Hence, the transformation

$$|\vec{p}, j, \lambda\rangle = \hat{l}_z(\vec{p}) \hat{r}(\varphi, \vartheta, 0) \, |j, \lambda\rangle \tag{13}$$

of the state $|j, \lambda\rangle$ in the rest frame represents a one-particle state $|\vec{p}, j, \lambda\rangle$ with momentum $\vec{p}$ in the helicity frame. [32, 33]
Now the angular part of the two-body decay amplitude in the helicity formalism can be formulated.

The Two-Body Decay Amplitude in the Helicity Formalism. Consider the decay of the particle a into the two particles b and c. The particle a carries the total angular momentum J_a and the helicity λ_a, whereas J_b and J_c as well as λ_b and λ_c are the total angular momenta and helicities of the two daughter particles a and b, respectively. [32]
The angular part of the decay amplitude of the two-body decay $a \to b + c$ can be constructed from two-particle states in the helicity frame. The two-particle states themselves are written as product states of the one-particle states $|\vec{p_b}, j_b, \lambda_b\rangle$ and $|\vec{p_c}, j_c, \lambda_c\rangle$. Furthermore, a summation over the unobserved helicities λ_b and λ_c has to be taken into account. Thus, the angular part of the two-body decay amplitude of the $a \to b + c$ process is given by the following expansion

$$A(a \to b + c) = \sum_{\lambda_b, \lambda_c} \langle \vec{p_b}, j_b, \lambda_b | \, \langle \vec{p_c} = -\vec{p_b}, j_c, \lambda_c | \, U \, |J_a, \lambda_a\rangle \equiv \sum_{\lambda_b, \lambda_c} A^{J_a, \lambda_a}_{\lambda_b \lambda_c} \tag{14}$$

with the decay operator U [32].
The contributing helicity amplitudes $A^{J_a, \lambda_a}_{\lambda_b \lambda_c}$ can be expressed by (see a detailed derivation in [35, 37])

$$A^{J_a, \lambda_a}_{\lambda_b \lambda_c}(a \to b + c) = \sqrt{\frac{2J_a + 1}{4\pi}} D^{*J_a}_{\lambda_a, \lambda_b - \lambda_c}(\varphi, \vartheta, 0) F^{J_a}_{\lambda_b \lambda_c}. \tag{15}$$

In the following the coefficients $F^{J_a}_{\lambda_b \lambda_c}$, which are called complex helicity amplitudes, are further specified depending on the considered two-body decays of concern in this work.
In this analysis the η_c is produced in the radiative magnetic dipole $M1$ transition of J/ψ to $\gamma\eta_c$. Thus, the expansion of the helicity amplitude (15) into radiative multipoles with regard to the total angular momentum J_γ of the radiative photon is an appropriate approach. In the so called radiative multipole basis the complex helicity amplitudes $F^{J_a}_{\lambda_b \lambda_c}$ with $J_a = J_{J/\psi}$, $\lambda_b = \lambda_\gamma$ and $\lambda_c = \lambda_{\eta_c}$ can be written as [33, 38]

$$F^{J_{J/\psi}}_{\lambda_\gamma \lambda_{\eta_c}} = \sum_{J_\gamma} \sqrt{\frac{2J_\gamma + 1}{2J_{J/\psi} + 1}} \left\langle J_\gamma, \lambda_\gamma; J_{J/\psi}, \lambda_{\eta_c} - \lambda_\gamma \middle| \, J_{\eta_c}, \lambda_{\eta_c} \right\rangle \cdot \alpha^{J_{J/\psi}}_{J_\gamma}. \tag{16}$$

Since the pseudoscalar η_c meson carries $J_{\eta_c} = 0$ and $\lambda_{\eta_c} = 0$, while $J_\gamma = 1$ is given for the photon and $J_{J/\psi} = 1$ for the vector meson J/ψ, the complex helicity amplitude simplifies to

$$F^1_{\lambda_\gamma 0} = \langle 1, \lambda_\gamma; 1, -\lambda_\gamma | \, 0, 0 \rangle \cdot \alpha^1_1. \tag{17}$$

Regarding the further two-body decays $a \to b + c$ of concern in this work, the total spin S and the relative orbital angular momentum L between the daughter particles b and c are good quantum numbers. Thus, the complex helicity amplitude can be modified using the so called LS basis (a detailed derivation can be found in [32]). In the LS basis it is given

$$F^{J_a}_{\lambda_b \lambda_c} = \sum_{L,S} \sqrt{\frac{2L + 1}{2J_a + 1}} \left\langle L, 0; S, \lambda_b - \lambda_c \middle| \, J_a, \lambda_b - \lambda_c \right\rangle \left\langle J_b, \lambda_b; J_c, -\lambda_c \middle| \, S, \lambda_b - \lambda_c \right\rangle \cdot \alpha^{J_a}_{LS}. \tag{18}$$

The coefficients $\langle 1, \lambda_\gamma; 1, -\lambda_{\gamma_r} | \, 0, 0 \rangle$ in (17) and $\langle J_b, \lambda_b; J_c, -\lambda_c \, | \, S, \lambda_b - \lambda_c \rangle$ in (18) are Clebsch-Gordan coefficients, which are tabulated for example in [36]. The complex coefficient α^1_1 in the multipole basis (16) and $\alpha^{J_a}_{LS}$ in the LS basis (18) are the complex fit parameters of a PWA fit. [33]

Now the formalism for the angular amplitudes of the two-body decays $a \to b + c$ of concern in this work are derived as series expansions of the helicity amplitudes $A^{J_a, \lambda_a}_{\lambda_b \lambda_c}$. By multiplying each included coefficient $F^{J_a}_{\lambda_b \lambda_c}$ with the dynamical contribution of the decay the angular amplitude is extended to the total two-body decay amplitude. Thus, in the following the dynamical contributions used in this analysis are described in more detail.

2.4.4 The Dynamical Part of the Two-Body Decay Amplitude

To parameterise the (mass-dependent) dynamical part, respectively the line shape, of a resonance different approaches are possible, for example the parameterisation with relativistic Breit-Wigner functions or with a K-matrix formalism. Both are implemented in this work and hence briefly introduced in the following.

The Breit-Wigner Parameterisation. The mass-dependent relativistic Breit-Wigner amplitude $BW(m)$ that describes the line shape of a resonance with the nominal mass m_0 and partial decay width Γ, which decays into two daughter particles with masses m_a and m_b is given by [33]

$$BW(m) = \frac{m_0 \; \Gamma \; B_L(q, q_0)}{m_0^2 - m^2 - i \; \frac{\rho}{\rho_0} \; m_0 \; \Gamma \; B_L^2(q, q_0)}, \tag{19}$$

with the phase space factors ρ and ρ_0. They follow the definitions

$$\begin{aligned} \rho_0 &\equiv \rho(m_0) \\ \rho(m) &= \sqrt{\left(1 - \left(\frac{m_b + m_c}{m}\right)^2\right) \cdot \left(1 - \left(\frac{m_b - m_c}{m}\right)^2\right)}. \end{aligned} \tag{20}$$

The L-dependent factors $B_L^2(q, q_0)$ are the so called Blatt-Weisskopf barrier factors. These factors take centrifugal barriers and thus the L-dependent distorted line shape of a resonance near a

threshold into account. They can be written as $B_L^2(q/q_0) = b_L(q)/b_L(q_0)$ with the damping functions $b_L(q)$, that depend on the momentum q of the resonance's daughter particles. Utilizing the transformation $x \equiv (q/q_R)^2$ with the momentum parameter $q_R \equiv \hbar c/R$ and the interaction radius R ("meson radius") set to $R = 0.66$ fm the corresponding damping functions $b_L(x)$ up to $L = 2$ are given by[3] [39]

$$\begin{aligned} b_0(x) &= 1 \\ b_1(x) &= \sqrt{\frac{2x}{x+1}} \\ b_2(x) &= \sqrt{\frac{13x^2}{(x-3)^2+9x}}. \end{aligned} \tag{21}$$

Theoretically, the Breit-Wigner parameterisation of a resonance is appropriate only, if the unitarity is not violated. This is given, if the resonance does not overlap with other resonances with the same quantum numbers, does not decay into another channel than the considered one and if it is not located directly next to a threshold. These conditions are strictly speaking unfulfilled in general. But especially in cases of sufficient separated resonances, of low statistics or of too many fit parameters, so that alternative parameterisations fail, the Breit-Wigner parameterisation is of special interest. Furthermore, the fit results for masses and partial decay widths of a Breit-Wigner parameterisation can easily be extracted from the PWA fit result. [32, 33]

The *K*-Matrix Formalism. Another approach to parameterise the dynamic of resonances is the K-matrix formalism. It avoids some of the main disadvantages of the Breit-Wigner parameterisation, since it is appropriate also for strongly overlapping resonances and conserves two-body unitarity already per construction. But the implementation is markedly more complicated and results commonly in a high number of fit parameters [32, 33].
In the following, a short introduction into the K-matrix formalism is given by presenting the main relevant definitions. The K-matrix formalism in general provides the description of two-particle scattering processes $a + b \to c + d$. But through a generalisation also the production process of resonances is included, which is of central concern in this work and described at the end.
Considering an initial state $|i\rangle$ that is transformed through a scattering process into the final state $|f\rangle$, then the corresponding transition amplitude S_{fi} is given by [33]

$$S_{fi} = \langle i | \, S \, | f \rangle \tag{22}$$

with the unitary scattering operator S (or S-matrix). The S-matrix can be separated into a part that describes the interaction between the initial and final state (expressed by the operator T, or T-matrix) and a part that contains the probability of no interacting states (expressed by the identity $\mathbb{1}$-matrix). Thus, the S-matrix can be written as

$$S = \mathbb{1} + 2iT. \tag{23}$$

Using the unitarity of the S-matrix, that means $SS^\dagger = S^\dagger S = \mathbb{1}$, one further gets in the Lorentz-invariant form [40]

$$(T^{-1} + i\rho \, \mathbb{1})^\dagger = T^{-1} + i\rho \, \mathbb{1}, \tag{24}$$

with the phase space factor ρ that is given in (20). By defining the operator

[3] In this work only orbital angular momenta $L = J \leq 2$ occur for intermediate resonances decaying to K^+K^- (see sect. 4.3.1 for details).

$$K^{-1} \equiv T^{-1} + i\rho\ \mathbb{1} \tag{25}$$

the so called Lorentz-invariant K-operator (or K-matrix) is introduced. It is a hermitian, symmetric operator (see eq. (24)) and hence, the K matrix can be chosen to be symmetric and real-valued with the elements [41]

$$K_{ij}(m) = \left(\sum_{\alpha=1}^{n} \frac{g_{\alpha i}\ g_{\alpha j}}{m_\alpha^2 - m^2} \ + \ f_{ij}^{\text{scatt}}\ \frac{m_0^2 - s_0^{\text{scatt}}}{m^2 - s_0^{\text{scatt}}} \right) f_{A0}(m), \tag{26}$$

whereby over all n resonances α with mass m_α is summed. The indices i and j indicate the corresponding matrix element, which corresponds to a certain channel of an initial state j into a final state i. Hence, if N is the number of channels and if in total n resonances are incorporated into the K-matrix, one gets a $N \times N$ matrix with n poles. But in general, the pole positions do not coincide with the resonances' masses, as it is for example for the T-matrix. [40]
The factors f_{ij}^{scatt} describe channel-dependent coupling constants and serve as free fit parameters. The factors $g_{\alpha i}$ are called g-factors and measure the coupling strength between the channel i and the resonance α, that has the partial decay width $\Gamma_{\alpha i}$ in the channel i. The g-factors can be expressed as [33]

$$g_{\alpha i} = \sqrt{\frac{m_\alpha\ \Gamma_{\alpha i}}{\rho_i(m_\alpha)}} \tag{27}$$

with the phase space factors $\rho_i(m_\alpha)$ that are defined in (20). The mass-dependent so-called Adler zero factors $f_{A0}(m)$ are given by [40]

$$f_{A0}(m) = \left(\frac{1\text{GeV}^2/c^4 - s_{A0}}{m^2 - s_{A0}} \right) \left(m^2 - \frac{1}{2} s_A m_\pi^2 \right) \tag{28}$$

and suppress an incorrect kinematic singularity near the threshold for $\pi\pi$ production. While m_π corresponds to the pion mass, the different real constants in equation (26) and (28) are set to $m_0^2 = 1.0\ \text{GeV}^2/c^4$, $s_0^{\text{scatt}} = -3.92637\ \text{GeV}^2/c^4$, $s_{A0} = -0.15\ \text{GeV}^2/c^4$ and $s_A = 1.0$ [40].
Up to this point, the K-matrix formalism only describes two-particle scattering processes. To generalise the formalism, so that it incorporates also production processes of resonances, the following extensions have to be done, which are known as the P-vector approach (see [42] for a detailed description). The T-operator has to be replaced by the so called F-operator (or transition amplitude) that is given by [40]

$$F = (\mathbb{1} - i\rho K)^{-1} P \tag{29}$$

with the production vector [41]

$$P_i(m) = \sum_{\alpha=1}^{n} \frac{\beta_\alpha\ g_{\alpha i}}{m_\alpha^2 - m^2} \ + \ f_i^{\text{prod}}\ \frac{m_0^2 - s_0^{\text{prod}}}{m^2 - s_0^{\text{prod}}}. \tag{30}$$

The factor $\beta_\alpha = \tilde{\beta}_\alpha \sqrt{m_\alpha \Gamma_\alpha}$ contains the information about the production strength $\tilde{\beta}_\alpha$ of the resonance α [33], that is commonly used as a fit parameter as well as the complex production constants f_i^{prod}. The real constant s_0^{prod} is chosen to be $-3.0\ \text{GeV}^2/c^4$ [40].
Applying the K-matrix formalism solely onto a single resonance, that decays only into a single final state, the relativistic Breit-Wigner parameterisation is received.

Now, the total two-body decay amplitude A of a single two-body decay is described. It is composed of the angular part (see eq. (14)) and the dynamical part (here Breit-Wigner function or K-matrix

formalism), that are decomposed into partial waves.

2.4.5 The Total Decay Amplitude

Consider now a decay chain, which is split into subsequent two-body decays. In Figure 4 the corresponding basic decay tree is pictured, the PWA is based on in this work.

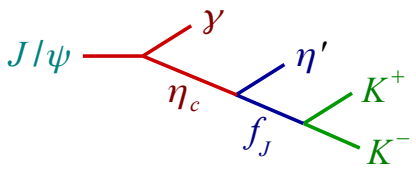

Figure 4: Illustration of the J/ψ decay tree in the isobar model of sub-sequent two-body decays. The J/ψ decays radiatively into $\gamma\eta_c$, that decays further to η' and the intermediate resonance f_J of the K^+K^- system.

The decay tree is composed of three two-body decays. By multiplying the three corresponding two-body decay amplitudes and summation over all unobserved quantities, the total amplitude A of the decay tree is derived. Using equation (15), (17) and (18) for the angular parts and the variables $g_i(m)$ to describe the dynamical parts of the two resonances η_c and f_J the total amplitude A is given by (the colors indicate the sub-decays as pictured in Figure 4)

$$
\begin{aligned}
A = \sum_{\lambda_{J/\psi}=-1,1,\lambda_\gamma=-1,1} \Bigg| & \sum_{\lambda_{\eta_c}} \sqrt{\frac{2J_{J/\psi}+1}{4\pi}} D^{*J_{J/\psi}}_{\lambda_{J/\psi},\lambda_{\eta_c}-\lambda_\gamma}(\varphi_{\eta_c},\vartheta_{\eta_c},0)\ \langle 1,\lambda_\gamma;1,-\lambda_\gamma \mid 0,0\rangle \alpha_1^1 \\
& \times \sum_{\lambda_{f_J},\lambda_{\eta'},L,S} \sqrt{\frac{2J_{\eta_c}+1}{4\pi}} \sqrt{\frac{2L+1}{2J_{\eta_c}+1}} D^{*J_{\eta_c}}_{\lambda_{\eta_c},\lambda_{f_J}-\lambda_{\eta'}}(\varphi_{f_J},\vartheta_{f_J},0) \\
& \times \langle L,0;S,\lambda_{f_J}-\lambda_{\eta'} \mid J_{\eta_c},\lambda_{f_J}-\lambda_{\eta'}\rangle \langle J_{f_J},\lambda_{f_J};J_{\eta'}-\lambda_{\eta'} \mid S,\lambda_{f_J}-\lambda_{\eta'}\rangle \alpha_{LS}^{J_{\eta_c}} \cdot g_{\eta_c}(m_{f_J\eta'}) \\
& \times \sum_{\lambda_{K^-},\lambda_{K^+},L',S'} \sqrt{\frac{2J_{f_J}+1}{4\pi}} \sqrt{\frac{2L'+1}{2J_{f_J}+1}} D^{*J_{f_J}}_{\lambda_{f_J},\lambda_{K^-}-\lambda_{K^+}}(\varphi_{K^-},\vartheta_{K^-},0) \\
& \times \langle L',0;S',\lambda_{K^-}-\lambda_{K^+} \mid J_{f_J},\lambda_{K^-}-\lambda_{K^+}\rangle \langle J_{K^-},\lambda_{K^-};J_{K^+},-\lambda_{K^+} \mid S',\lambda_{K^-}-\lambda_{K^+}\rangle \alpha_{L'S'}^{J_{f_J}} \cdot g_{f_J}(m_{K^+K^-}) \Bigg|^2,
\end{aligned}
\tag{31}
$$

whereby over the helicities $\lambda_{J/\psi}$ and λ_γ has to be summed incoherently. Furthermore, the two helicities are restricted to $\lambda_{J/\psi} = -1, 1$ and $\lambda_\gamma = -1, 1$, since a vanishing spin projection is denied for a photon and hence, for the J/ψ likewise, as it is produced in e^+e^- collisions through a decaying virtual photon.
However, the total decay amplitude (31) can be considerably simplified, since the helicities λ and the total angular momenta J for the pseudoscalar mesons η_c, η' and $K^\pm$ can be set to zero and the spin $J_{J/\psi}$ of the J/ψ vector meson to 1. Furthermore, the spin S' between the spinless kaons K^+ and K^- vanishes, which leads to $S' = 0$ and $L' = J_{f_J}$. Thus, the total decay amplitude simplifies to

$$
\begin{aligned}
A = \sum_{\lambda_{J/\psi}=-1,1,\lambda_{\gamma=-1,1}} \Bigg| \sum_{J_{f_J},\lambda_{f_J},L,S} & \sqrt{\frac{3(2J_{f_J}+1)(2L+1)}{(4\pi)^3}}\ \alpha_1^1\ \alpha_{LS}^0\ \alpha_{J_{f_J}0}^{J_{f_J}}\ \ g_{\eta_c}(m_{f_J\eta'})\ g_{f_J}(m_{K^+K^-}) \\
& \times D^{*1}_{\lambda_{J/\psi},-\lambda_\gamma}(\varphi_{\eta_c},\vartheta_{\eta_c},0)\ \langle 1,\lambda_\gamma;1,-\lambda_\gamma\ |0,0\rangle \\
& \times\ D^{*0}_{0,\lambda_{f_J}}(\varphi_{f_J},\vartheta_{f_J},0)\,\langle L,0;S,\lambda_{f_J}\ |0,\lambda_{f_J}\rangle\,\langle J_{f_J},\lambda_{f_J};0,0\ |S,\lambda_{f_J}\rangle \\
& \times\ D^{*J_{f_J}}_{\lambda_{f_J},0}(\varphi_{K^-},\vartheta_{K^-},0)\ \langle\, J_{f_J},0;0,0\mid J_{f_J},0\rangle|^{\,2}.
\end{aligned}
\tag{32}
$$

3 Experimental Setup

The study of the $\eta_c \to \eta' K^+ K^-$ decay in this work is based on data sets taken with the **BE**ijing **S**pectrometer BESIII at the **B**eijing **E**lectron **P**ositron **C**ollider BEPCII at the **I**nstitute of **H**igh **E**nergy **P**hysics IHEP in Beijing, China. In Figure 5 an aerial view of the BEPCII facility is pictured with the BESIII detector, which is red framed.
BEPCII is a double-ring e^+e^- collider. In two storage rings electrons and positrons circulate within bunches and are brought to collision at center-of-mass energies between $\sqrt{s} = 2.00 - 4.95$ GeV [43] with a peak luminosity of 1×10^{33} cm^{-2}s^{-1} at $\sqrt{s} = 2 \times 1.89$ GeV. Around the collision's **I**nteraction **P**oint IP the BESIII detector is located. The detector is designed and optimised for data taking at BEPCII and started operating in 2009. Utilizing the energy region, high luminosity and multi-bunch mode of BEPCII, the BESIII detector enables to study physics within the tau-charm energy region via high precision measurings with high statistical accuracy. [44, 45, 46]
In this section BEPCII is be briefly described (sect. 3.1). Afterwards, the BESIII detector and its sub-components are considered more precisely (sect. 3.2). Finally, the analysed data sets in this work are introduced (sect. 3.3).

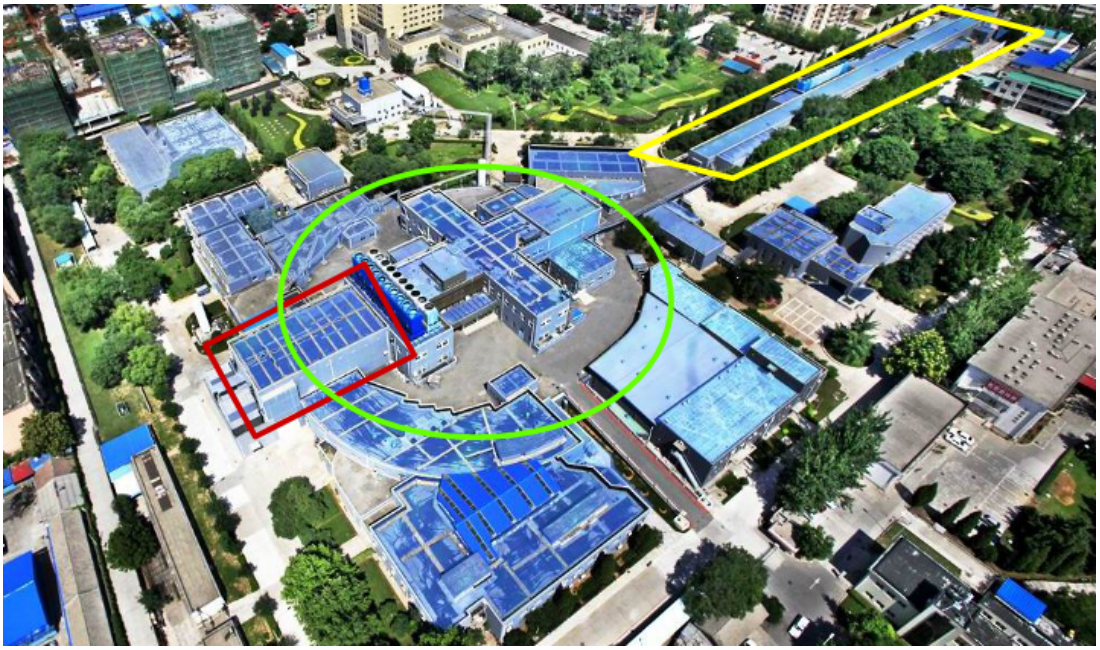

Figure 5: Aerial view of BEPCII in Beijing, China. Pre-accelerated electrons and positrons of the LINAC (framed in yellow) circulate in two storage rings of 237.5 m length (marked in green) and collide at the interaction point, where the BESIII experiment is located (framed in red). Figure taken from [47].

3.1 BEPCII

The initiation of the BEPCII/BESIII program dates back to the year 2003, whereby BEPCII replaced the former BEPC, that operated from 1989 to 2004. As a double-ring e^+e^- collider, BEPCII stores electrons and positrons in two rings with 237.5 m circumference, respectively. The **LIN**ear **AC**celerator LINAC of 202.4 m length (see Fig. 5 yellow frame) pre-accelerates the electrons and positrons up to 1.89 GeV and injects them into BEPCII in bunch mode. Thus, in total 2×93

bunches of electrons and positrons are stored in the two rings with a bunch spacing of 8 ns and a bunch size of 1.5 cm length, ≈ 380 µm width and ≈ 5.7 µm height. At the interaction point the electrons and positrons collide with a horizontal crossing angle of ±11 mrad. Due to its multi-bunch mode amongst other upgrades BEPCII reaches a circa 100 times higher design luminosity of 1×10^{33} cm^{-2}s^{-1} at beam energies of 2×1.89 GeV, than the former BEPC. Originally, BEPCII operated in the tau-charm energy region of $2.0 - 4.2$ GeV [44]. However, the maximum center-of-mass energy has been subsequently increased over the years up to 4.95 GeV recently [43]. [44, 45]

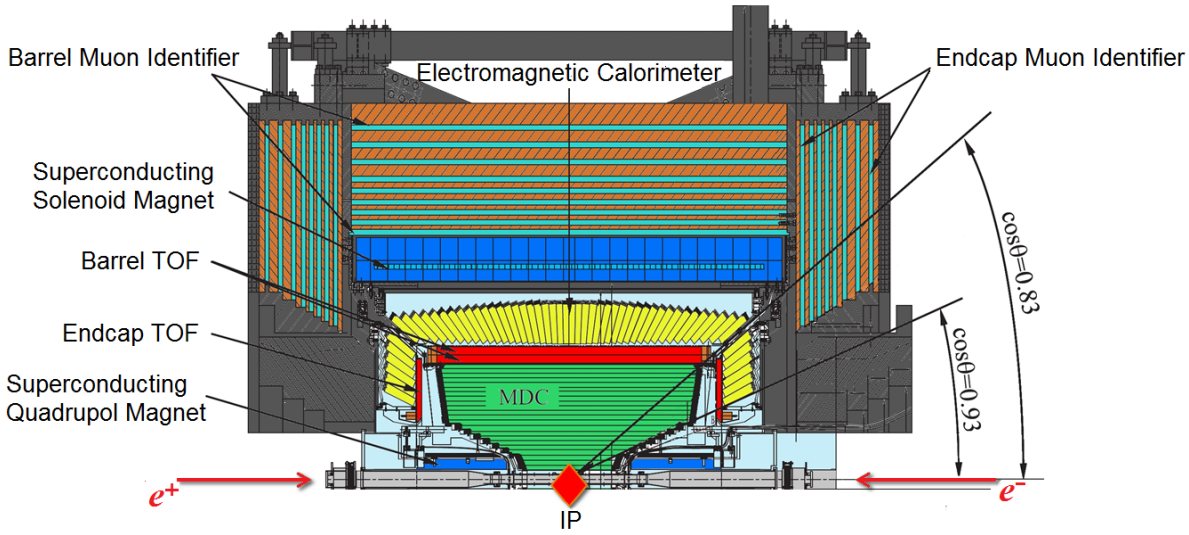

Figure 6: Schematical cross section of the BESIII detector that surrounds cylindrically the interaction point of the electron e^- and positron e^+ beams of BEPCII. Figure adapted from [48].

3.2 BESIII-Detector

The BESIII detector is the current replacement of the detectors BES and BESII, that ran from 1989 to 2004, while the BESIII experiment began data taking in 2009. The detector surrounds the interaction point of the electron and positron beams of BEPCII cylindrically and detects particles within a solid angle of 93% of 4π. A schematic cross section of the BESIII detector is shown in Figure 6. It contains a superconducting solenoid magnet of 1.0 T and several sub-detectors, that are used for particle identification, particle trajectory reconstruction as well as energy, momentum and energy loss per distance measurings of "stable" charged and neutral decay products of e^+e^- annihilations. The inner sub-detectors, surrounded by the superconducting solenoid magnet, are the **M**ultilayer **D**rift **C**hamber MDC, the **T**ime-**O**f-**F**light System TOF and the **E**lectro**M**agnetic **C**alorimeter EMC. While the MDC and TOF both detect charged particles, the EMC detects in particular photons and electrons. A Muon Identifier, that is located outside the solenoid magnet, is used to detect and discriminate muons and charged pions, in particular. All four sub-detectors as well as the solenoid magnet are described in more detail in the following. [44, 45, 46]

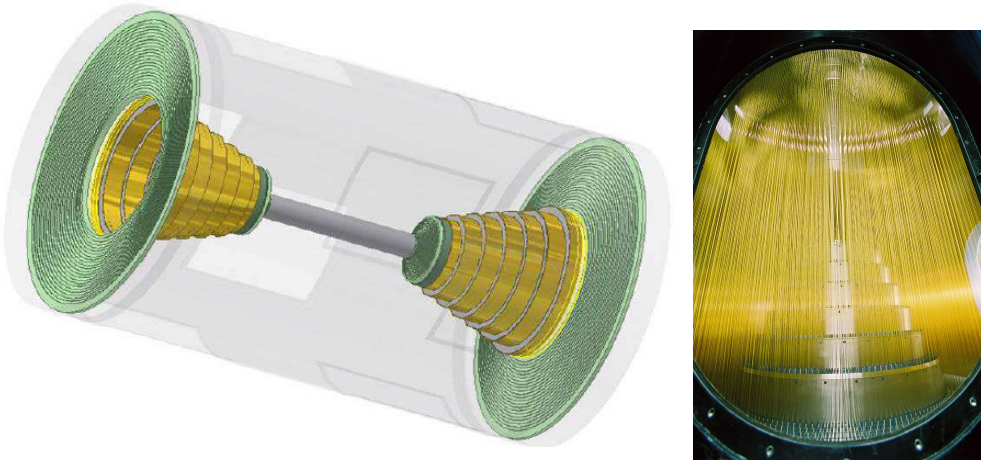

(a) (b)

Figure 7: The Multilayer Drift Chamber of the BESIII detector. (a) Schematical view (Figure taken from [44]). (b) A side view, that shows gold plated signal wires and the stepped region of the inner chamber underneath (Figure taken from [49]).

3.2.1 Multilayer Drift Chamber

The Multilayer Drift Chamber is the closest sub-detector of BESIII to the e^+e^- storage rings of BEPCII. It consists of an inner and an outer carbon chamber of 0.06 m, respectively 0.81 m diameter and of 2.58 m length. The chambers are filled with the working gas He:C_3H_8 with a ratio of 60:40. To position a quadrupol magnet for final beam focusing nearest to the e^+e^- interaction point (see Fig. 6), the MDC has conical endcaps. They are followed by a stepped like part that merges into the thinnest region of the inner chamber, like it is schematically shown in Figure 7 (a). Thus, the MDC provides a polar angle coverage of $|\cos\theta| < 0.93$. The two chambers contain in total 6796 gold plated signal wires embedded in 43 drift cell layers, that are aligned coaxial to the e^+e^- beams (see Fig. 7 (b)). [45]
If a charged particle enters the MDC it ionises gas molecules in all drift cell layers, that are passed through by the particle. The generated primary gas ions and free electrons further ionise gas molecules and hence, cause the generation of electron avalanches. These electron avalanches are detected via the signal wires with a high spatial resolution of 2.0 mm in beam direction and 0.13 mm in the corresponding vertical plane. Thus, the three dimensional particle trajectory is reconstructable. Due to the axial magnetic field of the soleonid magnet this trajectory is helical. Therefore, the MDC measures the helical trajectory of charged particles, that have in particular low momenta < 1.0 GeV/c. Low momenta are typical for hadronic decay products of e^+e^- annihilations at BESIII. Additionally, the particles' momenta and energy losses per distance are determined along the points of their trajectories via their deflection within the magnetic field and the measured intensities of the electron avalanches. Evaluating the measurement results, the MDC also offers particle identification capabilities of charged particles. [44, 45, 46]

3.2.2 Time Of Flight System

The Time-of-Flight System surrounds the MDC. It is built up of a barrel of 0.81 m to 0.93 m radius with two endcaps of 0.41 m to 0.89 m radius, as it is schematically pictured in Figure 8 (a). Thus, the TOF reaches a solid angle coverage of $|\cos\theta| < 0.82$ for the barrel. It is extended by the coverage

of the two endcaps of $0.85 < |\cos\theta| < 0.95$. Whereas the barrel contains 176 plastic scintillator bars of 2.38 m length arranged cylindrically in two layers (see Fig. 8 (b)), the endcaps consist of 48 scintillators within a single layer, respectively. The endcap scintillators are fanned out over the conical endcaps of the MDC and read out by a photomultiplier attached on the upper end of each scintillator element. In contrast, the barrel scintillator bars have a photomultiplier tube on both end faces. [45, 46]
If a charged particle crosses one of the TOF scintillators, a stop signal is sent, whereas the particle's time of origin (start signal) is determined by the known e^+e^- collision point of time. Thus, the particle's flight time from its origin at the e^+e^- interaction point to its point of registration in the TOF is calculated, whereby a time resolution up to 100 ps is reached. Based on the flight time measurement, the TOF also provides information about the particle's identity and is able to send trigger signals. [44, 45, 46]

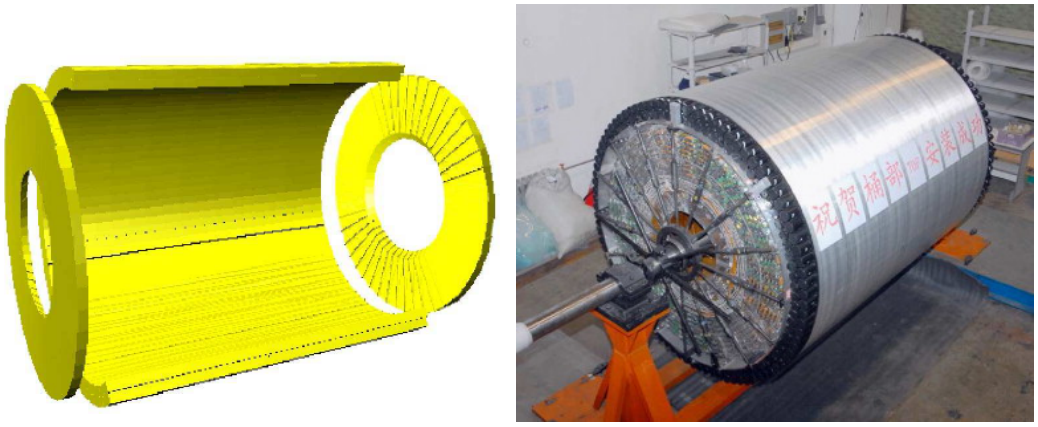

(a) (b)

Figure 8: The Time-of-Flight System of the BESIII detector. (a) Schematical view (Figure taken from [46]). (b) View of the barrel TOF consisting of 176 two layered scintillator bars (black bars), that surround the MDC. The TOF endcaps are assembled in this picture (Figure taken from [50]).

3.2.3 Electromagnetic Calorimeter

The Electromagnetic Calorimeter counts to the last inner sub-detectors of BESIII, that lies inside the solenoid magnet. It entirely covers the TOF and again is built up of a barrel with two endcaps on the end faces, like it is schematically shown in Figure 9 (a). With a length of 2.75 m and an inner radius of 0.94 m the barrel EMC provides a polar angle coverage of $|\cos\theta| < 0.83$. Due to the endcaps with an inner radius of 0.5 m an additional polar angle coverage of $0.85 < |\cos\theta| < 0.95$ is reached, which is the same as for the TOF. The barrel and the endcaps consist of in total 6240 CsI(Tl) crystals with photo-diodes at their rear face, respectively. The subset of 120 crystals are fan-shaped aligned in each of the 44 rings the barrel is composed of (see Fig. 9 (b)). The two endcaps contain in total 960 crystals within six rings, respectively. Due to the high amount of crystals, that have a dimension of (5.2×5.2) cm^2 in the front face and 0.28 m of length respectively, the entire EMC weights approximately 24 tons. [44, 45, 46]
The EMC is used to determine the total energy of electrons and photons as well as their position. For that, the incoming electrons or photons have to deposit their entire kinetic energy in the EMC via interactions with the crystals' material CsI(Tl). This happens for instance by emission of bremsstrahlung (electrons) or due to pair production (photons). The interactions generate electro-

magnetic showers in the crystals that are detected via the photo-diodes with a position resolution up to 0.6 cm and an energy resolution of 2.5% at 1 GeV. Thus, the EMC provides precise measurings of the position and the kinetic energy of photons and electrons within an energy range of 20 MeV to 2 GeV. [1, 44, 45, 46]

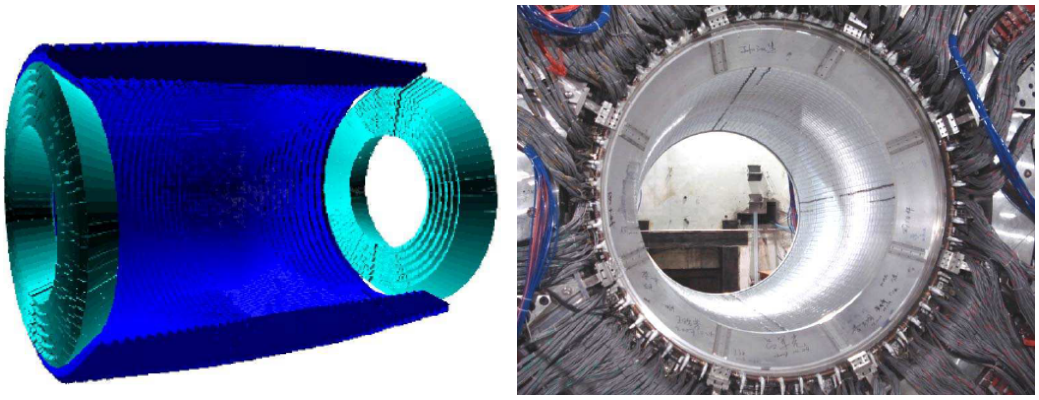

(a) (b)

Figure 9: The Electromagnetic Calorimeter of the BESIII detector. (a) Schematical view (Figure taken from [46]). (b) View inside the barrel EMC with its 5280 CsI(Tl) crystals. The EMC endcaps, the TOF and MDC are assembled in this picture (Figure taken from [44]).

3.2.4 Superconducting Solenoid Magnet

The BESIII detector contains a superconducting, single layered Solenoid Magnet (see Fig. 10 (b)), whereby the coil dimensions are: 3.52 m of length, 1.48 m of mean radius and 15 tons of total weight. The magnet separates the EMC from the Muon Identifier and provides a well-known, uniform and axial magnetic field of 1.0 T (0.9 T in 2012 [43]) within the MDC. Thus, it allows precise measurements of the momenta of charged particles via the MDC. [44, 45]

3.2.5 Muon Identifier

The Muon Identifier is the outermost sub-detector of the BESIII experiment. As the other three sub-detectors the Muon Identifier is built up of a barrel and two endcaps. Both, the barrel and endcap parts consist of layers of steel absorbers and of **R**esistive **P**late **C**hambers RPC in a sandwich-like composition as it is shown in Figure 10. While the barrel contains nine layers of RPC, the endcaps have eight RPC layers, respectively. Each RPC is filled with the gas mixture Ar:$C_2H_2F_4$:Isobutane with a ratio of 50 : 42 : 8. [44]
An entering charged muon or hadron ionises gas molecules in the passed through RPC layers and thus, generates charge carrier avalanches, which are detected as hits in the corresponding RPC layers. The combination of several parameters, like the amount of fired RPC layers, the penetration depth into the Muon Identifier and the measurement results of the MDC allows a muon/hadron differentiation. Especially, the identification and differentiation of muons and charged pions is of high interest. Having almost similar masses, pions and muons are mainly distinguished via their significantly different penetration depth into the Muon Identifier. Whereas pions are distinctly slowed down within the steel absorbers, the muons pass through with nearly no energy loss. For effective muon/hadron analysis the momentum of an entering muon in the Muon Identifier has to be larger than 0.4 GeV/c, as muons belong to minimum ionizing particles. [44, 45, 46]

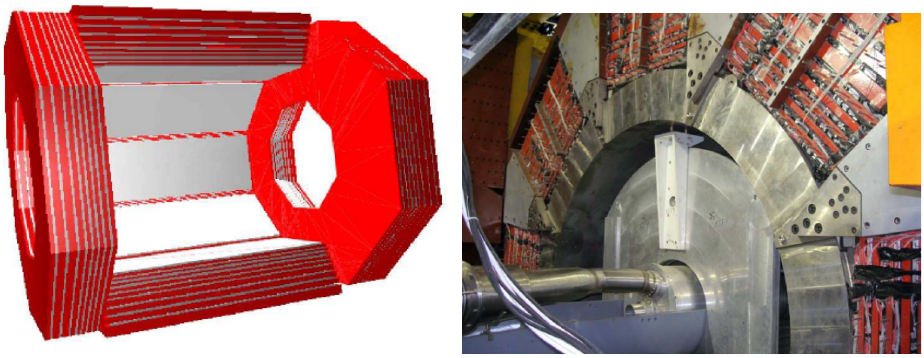

(a) (b)

Figure 10: The Muon Identifier as the outermost sub-detector of BESIII. (a) Schematical view (Figure taken from [46]). (b) A cross-sectional view of the barrel of the Muon Identifier, that shows the sandwich-like arranged nine layers of steel absorbers (red bars) and Resistive Plate Chambers between the absorbers. The endcaps of the Muon Identifier are exposed in this picture. Hence, the Superconducting Solenoid Magnet, that is covered by the Muon Identifier, is also visible (iron ring) (Figure taken from [44]).

3.2.6 Parameters and Performance of the BESIII Detector

In Table 6 all relevant parameters and resolution factors of the four described sub-detectors and of the Solenoid Magnet are summarized.

	Detector Parameters and Performance	
BESIII	solid angle coverage $\Delta\Omega/4\pi$	93%
MDC	spatial resolution σ_z in beam-(z) direction	2 mm
	spatial resolution $\sigma_{r\phi}$ in vertical-($r\phi$) plane	0.13 mm
	momentum resolution σ_p/p at 1.0 GeV/c	0.5%
	energy deposit resolution $\sigma_{dE/dx}$ at 1.0 GeV/c	6.0%
TOF	time resolution σ_t for the barrel	100.0 ps
	time resolution σ_t for the endcaps	110.0 ps
EMC	energy resolution σ_E/E at 1.0 GeV	2.5%
	position resolution at 1.0 GeV	0.6 cm
Solenoid Magnet	magnetic field B	1.0 T (0.9 in 2012)
Muon Identifier	minimal muon momentum required p_{min}	0.4 MeV/c

Table 6: Parameters and performance of the components of the BESIII detector (values are taken from [43, 45, 46]).

3.3 Datasets

The analysis of the $\eta_c \to \eta' K^+ K^-$ decay in this work is based on the J/ψ data sample, that is provided by the BESIII experiment.

The J/ψ Data Sample
From 2009 to 2019 J/ψ data has been taken at BESIII during four periods, whereby in total $(10.087 \pm 0.044) \cdot 10^9$ J/ψ events have been collected. The determination of the J/ψ number is

based on inclusive J/ψ decays and the method presented in [51]. Thus, the BESIII experiment provides the world's largest J/ψ data sample so far and all included J/ψ events are taken into account to study the η_c decay to $\eta' K^+K^-$ via the decay chain, that is presented next.

The studied Decay Chain
The reaction $\eta_c \to \eta' K^+K^-$ is analysed in this work by using the following J/ψ decay tree:

$$\boxed{J/\psi \to \gamma\,\eta_c \to \gamma\,\eta'\,K^+K^- \begin{cases} \to \gamma\,\gamma\pi^+\pi^-\,K^+K^- & \text{for} \quad \eta' \to \gamma\pi^+\pi^- \\ \to \gamma\,(\eta \to \gamma\gamma)\pi^+\pi^-\,K^+K^- & \text{for} \quad \eta' \to \eta\pi^+\pi^- \end{cases}} \tag{33}$$

It takes the two main decay channels of η' into account, since the η' meson has decayed before it is detectable by the BESIII detector:

$$\begin{aligned} \eta' \to \gamma\pi^+\pi^- \quad &\text{with} \quad BR_{\eta' \to \gamma\pi^+\pi^-} = (28.9 \pm 0.5)\%\ [12] \\ \eta' \to \eta\pi^+\pi^- \quad &\text{with} \quad BR_{\eta' \to \eta\pi^+\pi^-} = (42.6 \pm 0.7)\%\ [12], \end{aligned} \tag{34}$$

whereby the short-living η meson is reconstructed via its main decay into two photons:

$$\eta \to \gamma\gamma \quad \text{with} \quad BR_{\eta \to \gamma\gamma} = (39.41 \pm 0.20)\%\ [12]. \tag{35}$$

Thus, the $\eta_c \to \eta' K^+K^-$ reaction is analysed via two final state channels. The final states consist of two respectively three photons and the charged pseudoscalar mesons $\pi^\pm$ and $K^\pm$.
In the following, the distinction between both final states will be made by indicating the corresponding η' decay channel, either as the $\eta' \to \gamma\pi^+\pi^-$ channel or the $\eta' \to \gamma\pi^+\pi^-$ channel.

Besides the J/ψ data sample to study the η_c reaction via the presented decay chain, also precise **M**onte **C**arlo MC simulations of data are crucial and used for different purposes in this work. They are presented in the following.

Monte Carlo Simulations
MC simulations provide simulated data, that contain random calculated events generated via a MC algorithm on the base of the decay tree the user has specified before. For the BESIII experiment the specific and adapted MC generators KKMC [52] and BesEvtGen [53] are available, which are designed for simulating data in the tau-charm energy region. [46]
For the simulation of J/ψ events in this work the KKMC generator is used, that creates the charmonium state via simulated e^+e^- annihilations [46]. All further sub-decays of concern according to equation (33) are modelled with the BesEvtGen generator. BesEvtGen is a BESIII specific further development of the EvtGen generator, since the original has been designed for simulating data of decaying B mesons [54] and not for data in the tau-charm energy region of BESIII. Involving several models the BesEvtGen generator calculates random events of decaying charmonia states and light hadronic daughter particles precisely and of high quality. [46]
The purely generated MC events are treated with a detector simulation software, that leaves over the fraction of so called accepted MC events, which have been "detected" (or "accepted") by the detector simulation, as if they were real data. For instance, the detector simulation of BESIII, realised with the GEANT4 package [55], contains a precise description of the BESIII detector, particle tracking processes and of the detector response. [46]
Within this work two different MC simulations are used. Each contains solely events, that are evenly distributed in phase space. The datasets are presented in the following by specifying the corresponding decay chain and stating the relevant purposes. Additionally, a so called inclusive MC

simulation of J/ψ decays is introduced at the end of this section.

Signal MC Simulation. The signal MC simulation consists of $4.5 \cdot 10^6$ signal events, as it is given by the following decay chain (the percentage values above the arrows are the branching ratios used for the included decays)

$$\begin{aligned} J/\psi &\xrightarrow{100\%} \gamma\eta_c \\ \eta_c &\xrightarrow{100\%} \eta' K^+K^- \\ \eta' &\xrightarrow{42.6\%,\,[12]} \pi^+\pi^- \ (\eta \xrightarrow{100\%} \gamma\gamma) \\ \eta' &\xrightarrow{28.9\%,\,[12]} \gamma \ (\rho_0 \xrightarrow{100\%} \pi^+\pi^-), \end{aligned} \tag{36}$$

whereby the branching ratios of the two η' decays in combination are scaled to 100% via the generator. This simulation is chiefly used for the optimisation of event selection criteria and for comparison purposes with real data.

PWA MC Simulation. A partial wave analysis model in general includes solely the physics of the processes present in data. But it contains no information about the detector response, characteristics or the detector efficiency. Thus, the PWA solution would not fit experimental data correctly in general. Hence, a PWA MC simulation is required as additional PWA input, since this simulation incorporates and therefore provides the whole detector information for the PWA solution.
For a sufficient number of events the PWA MC simulation in this work includes around $2 \times 30 \cdot 10^6$ events for the final state channels $\eta' \to \gamma\pi^+\pi^-$ and $\eta' \to \eta\pi^+\pi^-$.
In order to account for non-resonant background in the invariant η_c mass spectrum, that remains after applying the event selection procedures presented in section 4.1, the PWA MC simulation is modelled excluding the η_c meson

$$\begin{aligned} J/\psi &\xrightarrow{100\%} \gamma\eta' K^+K^- \\ \eta' &\xrightarrow{42.6\%,\,[12]} \pi^+\pi^- \ (\eta \xrightarrow{100\%} \gamma\gamma) \\ \eta' &\xrightarrow{28.9\%,\,[12]} \gamma \ (\rho_0 \xrightarrow{100\%} \pi^+\pi^-). \end{aligned} \tag{37}$$

Inclusive MC Simulation. Additionally, an inclusive MC simulation at the J/ψ resonance is utilised in this work. It is provided by BESIII and used for background studies and the definition of selection conditions for the event selection (see sect. 4.1). Utilizing several generators the inclusive MC simulation at the J/ψ resonance includes the J/ψ generation, continuum production and the processes of the decaying J/ψ charmonium. The corresponding branching ratios are either taken from the **P**article **D**ata **G**roup PDG database [12] (if they are known), or they are modelled using the LUNDCHARM model [56] (if they are yet unknown). [46]
The intrinsic advantage of the inclusive MC simulation is, that it offers access to any included reaction. Thus, it is a highly effective simulation to study background components, as the total background can be split into all entering reactions and hence studied separately.

4 Analysis

The J/ψ data sample and MC simulations contain a large number of events. Via event selection criteria the searched signal reaction $\eta_c \to \eta' K^+ K^-$ is filtered out. However, in view of the upcoming PWA the datasets have to be further prepared, since a high significance of signal above background and a background level as low as possible optimise the PWA fit results.
Thus, in this chapter at first the subsequent data filtering process via several event selection procedures is presented (see sect. 4.1). Afterwards, their results are evaluated concerning the achieved background reduction and significance for the $\eta_c \to \eta' K^+ K^-$ reaction (see sect. 4.2). Finally, in section 4.3 the implemented PWA hypotheses and their results are presented and compared to the theoretical predictions given in section 2.3.

4.1 Event Selection

In this section the applied event selection procedures to select the $\eta_c \to \eta' K^+ K^-$ reaction in the J/ψ data sample are presented. Using the **F**inal **S**tate **Filter** package FSFilter running on BOSS version 7.0.5 all datasets, introduced in section 3.3, are initially pre-filtered via various implemented rough selection conditions [57]. In addition, further general criteria are added in this work, in order to suppress background reactions and increase the significance. A summary of the applied general event selection procedures are given in section 4.1.1. Based on the results of background studies using the inclusive MC simulation (see sect. 4.1.2) further specific event selection criteria are identified, which are presented in section 4.1.3. In section 4.1.4 the event selection procedure is discussed.

4.1.1 General Event Selection

The general event selection conditions used in this work for a rough pre-filtering of data and MC simulation is introduced in the following, starting with the final state reconstruction. Afterwards, further applied conditions regarding specific detector characteristics as well as charged and neutral particles are presented.

Final State Reconstruction. The pre-selection and identification of final state particles, that fulfil the user given final state hypothesis, is done by the FSFilter package while analysing data or MC simulation at BESIII. Here, the two final states $\gamma\gamma K^+ K^- \pi^+ \pi^-$ (for the $\eta' \to \gamma\pi^+\pi^-$ channel) and $\gamma\gamma\gamma K^+ K^- \pi^+ \pi^-$ (for the $\eta' \to \eta\pi^+\pi^-$ channel) are implemented in the FSFilter framework. That means, two charged kaons $K^\pm$ and two pions $\pi^\pm$ are required for both final states. Besides, two additional random charged tracks are allowed for each event via the FSFilter algorithm. Furthermore, for each event up two ten detected photons are stored, whereby for the $\eta' \to \gamma\pi^+\pi^-$ channel only two photons are needed as final state photons. Three final state photons are required for the $\eta' \to \eta\pi^+\pi^-$ channel.
Hence, a large number of different combinations of the up to ten stored photons and six charged tracks are possible to build the final state for each single event. These combinations are comparable via their χ^2 value of an applied kinematic fit[4]. In this work the particle combination with the lowest χ^2 value is chosen as the best combination of an event.
In addition, the $\eta' \to \eta\pi^+\pi^-$ channel has to fulfil the following further photon condition. Two of the three final state photons have to result from an $\eta \to \gamma\gamma$ decay. Here, the best combination is chosen via the condition $0.4\ \mathrm{GeV}/c^2 < m(\gamma\gamma) < 0.7\ \mathrm{GeV}/c^2$ [57] and via the lowest χ^2 value of an

[4] Within a kinematic fit a certain particle combination is analysed by altering the single particle four-momenta in the range of their detector given uncertainties. The four momenta combination, that fulfils the conservation of energy and momentum best is chosen and assigned the corresponding χ^2 value.

additional applied one constraint kinematic η fit onto the $\gamma\gamma$ mass.

Besides the required final states particles the intermediate states η_c and η' are demanded for both channels. They are selected by defining the following rough mass selection conditions

$$\begin{aligned} &\text{for the } \eta' \to \gamma\pi^+\pi^- \text{ channel } \begin{cases} 2.6\ \text{GeV}/c^2 < m(\gamma\pi^+\pi^-K^+K^-) < 3.1\ \text{GeV}/c^2 & \text{for } \eta_c \\ 0.868\ \text{GeV}/c^2 < m(\gamma\pi^+\pi^-) < 1.048\ \text{GeV}/c^2 & \text{for } \eta' \end{cases} \\ &\text{for the } \eta' \to \eta\pi^+\pi^- \text{ channel } \begin{cases} 2.6\ \text{GeV}/c^2 < m(\eta\pi^+\pi^-K^+K^-) < 3.1\ \text{GeV}/c^2 & \text{for } \eta_c \\ 0.848\ \text{GeV}/c^2 < m(\eta\pi^+\pi^-) < 1.068\ \text{GeV}/c^2 & \text{for } \eta'. \end{cases} \end{aligned} \tag{38}$$

Finally, for the $\eta' \to \gamma\pi^+\pi^-$ channel the η' is selected via the final state photon, that yields the best η'.

General Cuts concerning Detector Characteristics. Various detector specific cuts have to be defined that accommodate certain detector characteristics, like the incomplete solid angle coverage of 93% of 4π, for what only a fraction of final state particles are detectable with BESIII.
The polar angle coverage of the MDC is restricted (see Fig. 6). Thus the polar angle θ of a charged track has to fulfil the same condition of

$$|\cos\theta| < 0.93,$$

otherwise the detected particle is not identified as a charged particle.
Similar conditions as for the MDC are applied to neutral particles, here photons, that are detected by the EMC via electromagnetic showers. The barrel and end cap construction of the EMC requires a certain polar angle range for detection, respectively. Furthermore, in order to suppress low energy background photons a minimal energy deposit of actual final state photons is required. Hence, detected photons have to fulfil either

$$E_\gamma > 25\ \text{MeV} \quad \text{with} \quad |\cos\theta| < 0.80 \quad \text{for barrel photons or}$$

$$E_\gamma > 50\ \text{MeV} \quad \text{with} \quad 0.86 < |\cos\theta| < 0.92 \quad \text{for end cap photons.}$$

Additionally, the shower time of a generated electromagnetic shower in the EMC is restricted to

$$0\ \text{ns} < t < 700\ \text{ns},$$

in order to reduce electronic noise. [57]

Further General Cuts for Charged Tracks. The complex particle identification process of BESIII, that takes information of several BESIII sub-detectors (TOF, MDC, EMC) into account, enables to distinguish between charged kaons $K^\pm$, pions $\pi^\pm$, protons $p/\bar{p}$, electrons $e^\pm$ and muons $\mu^\pm$. For that, each detected charged track is assigned the calculated probabilities $P(x)$ with $x = K^\pm, \pi^\pm, p/\bar{p}, e^\pm$ or $\mu^\pm$, that can be easily used for event selection [57]. In this work the required charged final state kaons and pions have to fulfil the following conditions

$$P(K^\pm) > P(\pi^\pm), P(p^\pm), P(e^\pm), P(\mu^\pm), 10^{-4},$$

$$P(\pi^\pm) > P(K^\pm), P(p^\pm), P(e^\pm), P(\mu^\pm), 10^{-4}.$$

That means, a charged track is only counted as a kaon $K^\pm$ (respectively pion $\pi^\pm$), if the corresponding probability $P(K^\pm)$ (respectively $P(\pi^\pm)$) is larger than the probabilities for being one of the other possible charged particles. Furthermore, it has to be at least larger than 10^{-4} in order to

reject tracks, for which the probability determination fails.
Additionally, a primary vertex fit is applied to charged tracks via the FSFilter package, while combining the particles to form the final state(s). It is based on the evaluation of the trajectory origin of charged particles passing the MDC [57], whereby the point of lowest distance to all tracks is defined as the particles' common origin (vertex). The combination of particles that fulfils the vertex condition best, is chosen. Thus, the primary vertex fit is based on the assumption, that all intermediate states (except K_S^0 and Λ resonances) decay immediately at the primary vertex, which is expected to be in close vicinity to the interaction point of the e^+e^- beams. This assumption is justified here, since the mean lifetimes of occurring intermediate states lie in the range of $(10^{-17} - 10^{-23})$ s (see Table 2 and 3).
Finally, a vertex cut is applied to all charged final state particles (here kaons $K^{\pm}$ and pions $\pi^{\pm}$). The closest distance of the trajectory of each charged particle to the e^+e^- interaction point has to lie within a cylindrical volume of 1.0 cm radius and 20.0 cm length. This volume is aligned coaxially to the beam line and symmetrically around the interaction point. With the z axis corresponding to the beam line direction and r to the radial direction, the cylindrical volume V and hence the vertex cut conditions can be written as

$$V_r < 1.0 \text{ cm}, \quad |V_z| < 10.0 \text{ cm}.$$

Further General Cuts for Neutral Particles. Neutral particles, here photons, are detected spatially resolved by the EMC via electromagnetic showers. But a high amount of detected photons are no real final state photons. These unwanted photons occur for example due to photon emission processes of decaying or accelerated charged particles. Usually, the angle between an unwanted photon, that is emitted by a charged particle, and the charged particle itself is small. The angle is defined between the detected and extrapolated trajectories of the unwanted photon and the charged particle. Thus, by requiring a minimum angle between an unwanted photon γ and the next closest charged track [57], the counting of photons resulting from decaying charged particles is widely suppressed. In this work the minimum angle is set to the experimentally well established value of

$$\angle(\gamma, \text{closest charged track}) > 10^{\circ}.$$

Furthermore, in order to avoid background components above the η_c signal with $m_{\eta_c} = 2.984$ GeV/c^2 [12] and below the phase space edge of $m_{J/\psi} = 3.0969$ GeV/c^2 [12], the radiative photon energy of the $J/\psi \to \gamma_r \eta_c$ decay is set to be at least

$$E_{\gamma_r} > 0.06 \text{ GeV}.$$

This is done to accommodate the fact that a large background part is given by events that contain at least one low energy photon that is incorrectly assigned to be the radiative photon of the $J/\psi \to \gamma_r \eta_c$ decay.

The presented general event selection criteria in this section cause a first rough background reduction. But there is still a high amount of background reactions left, that cover the signal part further on. Thus, additional criteria are needed, that eliminate specifically the remaining background components.

4.1.2 Background Studies with Inclusive MC Simulation

In order to determine further specific event selection criteria, background studies have been performed using the inclusive MC simulation. For that, the whole inclusive MC simulation has been split into signal and background reactions. The main outstanding background parts, which have

been observed, are summarised in Table 7 together with some exemplary reactions.
The main background reactions are composed of a decay chain, that does not contain the $\eta_c \to \eta' K^+ K^-$ decay. Thus, the final state particles result mainly from other intermediate states as the required ones. For instance, the final state photons of both final state channels result frequently from one or even two neutral pion decays through the reaction $\pi^0 \to \gamma\gamma$. Other frequent and unwanted intermediate reactions are decays of excited neutral kaons into neutral kaon-pion pairs via $K^*(892)^0 \to K^\pm \pi^\mp$. Additionally, for the $\eta' \to \eta\pi^+\pi^-$ channel the intermediate resonance η is often missing, whereas vice versa for the $\eta' \to \gamma\pi^+\pi^-$ channel an unwanted η is observed in many reactions. Lastly, also reactions that do not match with the required two final states generate noticeable background parts, for instance due to missing photons or due to multiple pion pairs $n \cdot \pi^+\pi^-$ with $n > 1$.

Unwanted Background Component	**Exemplary Background Reaction**
Neutral Pions π^0	$J/\psi \to \pi^0 K^+ K^- \pi^+ \pi^-$
Excited Kaons $K^*(892)^0/\bar{K}^*(892)^0$	$J/\psi \to \gamma K^- (K^{*0} \to K^+\pi^-)\pi^+$
Unwanted η (for $\eta' \to \gamma K^+ K^-$)	$J/\psi \to (\eta \to \gamma\gamma) K^+ K^- \pi^+ \pi^-$
Missing η (for $\eta' \to \eta K^+ K^-$)	$J/\psi \to (b_1^0 \to (\omega \to \pi^+\pi^-\pi^0)\pi^0) K^+ K^-$
Multiple Pion Pairs $n \cdot \pi^+\pi^-$ with $n > 1$	$J/\psi \to K^+ K^- \pi^+ \pi^- \pi^+ \pi^-$
Missing γ	$J/\psi \to \gamma K^+ K^- \pi^+ \pi^-$

Table 7: Main background components observed within the inclusive MC simulation. Additionally, an exemplary reaction of each background component is given. The background component η depends on the considered final state channel. Whereas for the $\eta' \to \eta\pi^+\pi^-$ channel an η is often missed, it is vice versa often seen for the $\eta' \to \gamma\pi^+\pi^-$ channel, where it is unwanted.

In order to reduce these remaining main background components several specific vetoes are applied as well as a four constraint kinematic fit, which are presented in the following section.

4.1.3 Specific Event Selection

For the elimination of background components that contain excited kaons $K^*(892)^0$ or an unwanted (missing) η meson specific mass cuts are applied. Events with missing photons or supernumerary pion pairs are rejected via a four constraint kinematic fit and an appropriate χ^2 cut. Furthermore, a one-constraint kinematic fit is used to reject two-photon combinations that result from π^0 decays in order to reduce background reactions containing neutral pions. All these specific event selection criteria are described in detail in the following, starting with the $K^*(892)^0$ and η mass cuts.

The $K^*(892)^0$ Mass Cut. To veto background reactions with excited kaons $K^*(892)^0$ decaying to $K^\pm\pi^\mp$ corresponding mass cuts are applied. The cut limits are determined through a fit of the invariant $K^+\pi^-$ and $K^-\pi^+$ mass spectra of the inclusive MC simulation. The two spectra are shown in Figure 11 for the $\eta' \to \gamma\pi^+\pi^-$ channel, whereby the inclusive MC simulation is marked in blue. Both spectra feature a clear $K^*(892)^0$ peak at about 0.9 GeV/c^2 sitting on large continuum. In order to estimate approximately appropriate cut limits, the $K^*(892)^0$ signal is fitted roughly by a Gaussian function. The background is described via a polynomial function of third order. The total fit is marked in red. The fit results for the Gaussian function and the total χ^2 value are presented in Table 8.

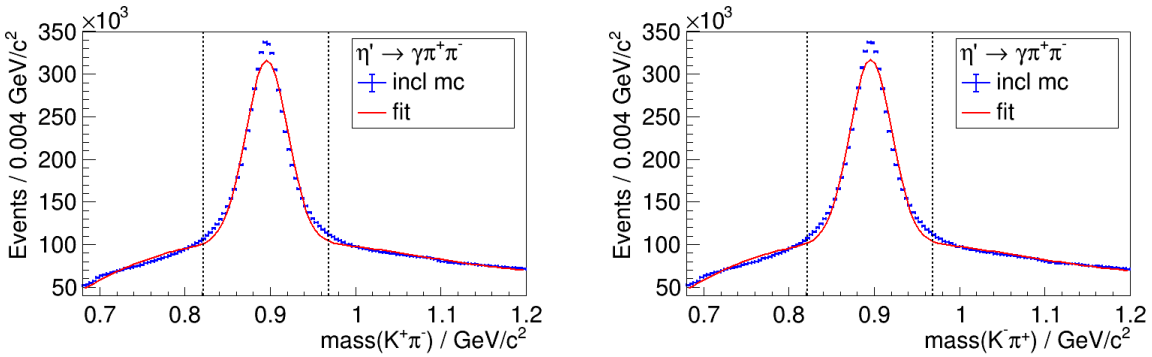

(a) (b)

Figure 11: The invariant mass spectra of $m(K^+\pi^-)$ in (a) and $m(K^-\pi^+)$ in (b) of the inclusive MC simulation (marked in blue) for the $\eta' \to \gamma\pi^+\pi^-$ channel for estimating the $K^*(892)^0$ cut limits. The inclusive MC simulation is fitted approximately by a sum over a Gaussian function and a polynomial function of third order, that is shown in red. The $\pm 3\sigma$ surrounding of the Gaussian maximum defines the $K^*(892)^0$ selection limits, which are highlighted with black dashed lines.

	Reaction	
Fit Parameter	$K^*(892)^0 \to K^+\pi^-$	$\overline{K}^*(892)^0 \to K^-\pi^+$
Intensity I / Events $(0.004\ \text{GeV}/c^2)^{-1}$	210921.7 ± 209.7	211818.0 ± 202.7
Maximum m_0 / GeV/c^2	0.896 ± 0.0000	0.896 ± 0.0000
Width σ / GeV/c^2	0.024 ± 0.0000	0.024 ± 0.0000
χ^2/NDF	$25844.3/123.0 = 210.1$	$26670.2/123.0 = 216.8$

Table 8: Fit parameters for the Gaussian function and the total χ^2/NDF value of the fit of the inclusive $K^\pm\pi^\mp$ mass spectra for the $\eta' \to \gamma\pi^+\pi^-$ channel, as described in the text.

As expected the total fit provides less well values for the χ^2/NDF and neglectable uncertainties for the maximum and width of the Gaussian function. Both aspects are discussed in section 4.1.4 and do not preclude the further evaluation of the fit results for the rough determination of the selection limits. Hence, the region $\pm 3\sigma$ around the Gaussian maximum m_0 is used for defining the selection limits, which are for both reactions given by

$$0.822\ \text{GeV}/c^2 < m(K^\pm\pi^\mp) < 0.969\ \text{GeV}/c^2. \tag{39}$$

As expected, the cut limits coincide for the two spectra, since the strong decay of $\overline{K}^*(892)^0 \to K^-\pi^+$ is the complex conjugated one of $K^*(892)^0 \to K^+\pi^-$. Thus, the two reactions are expected to be symmetric assuming CP conservation within the strong interaction. Furthermore, the estimated cut limits (39) are applied to both final state channels, since their determination via the $\eta' \to \gamma\pi^+\pi^-$ channel is sufficient for this analysis.
For comparison purposes, in Figure 12 the invariant $K^+\pi^-$ mass spectra of data are shown (marked in black) for both final state channels. In green the signal MC simulation is pictured, which is scaled in such a way, that it is comparable with data. As excepted, the signal MC simulation shows no $K^*(892)^0$ resonance, since the $K^*(892)^0$ is not incorporated. In both spectra the $K^*(892)^0$ cut limits of eq. (39) are highlighted with black dashed lines, which enclose the $K^*(892)^0$ mass peaks of data well. The corresponding $K^-\pi^+$ mass spectra can be found in the appendix 6.1 in Figure 35.

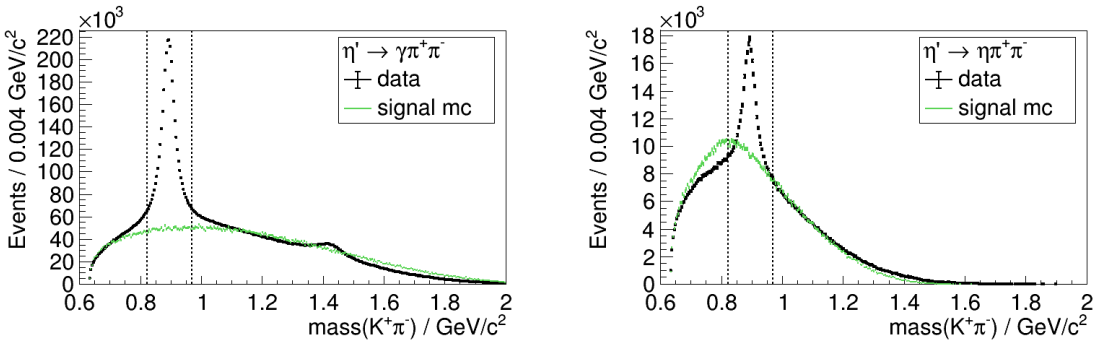

(a) (b)

Figure 12: Invariant $K^+\pi^-$ mass spectra of data (marked in black) for the $\eta' \to \gamma\pi^+\pi^-$ channel in (a) and for the $\eta' \to \eta\pi^+\pi^-$ channel in (b). In comparison the scaled signal MC simulation is added in green as well as the $K^*(892)^0$ selection limits, which are highlighted with black dashed lines.

The η Mass Cut. The rejection of background components that contain an unwanted η in the $\eta' \to \gamma\pi^+\pi^-$ channel as well as the selection of events that actual feature an η in the $\eta' \to \eta\pi^+\pi^-$ channel are realised via a mass cut onto an invariant $\gamma\gamma$ mass spectrum, since η decays predominantly into two photons [12]. The $\gamma\gamma$ mass spectrum is generated out of all possible $\gamma_i\gamma_j$ combinations (with $i < j$), that can be composed out of the up to ten stored photons of every single event. In Figure 13 (a) the inclusive MC simulation (marked in blue) of the invariant $\gamma_i\gamma_j$ mass spectrum is pictured showing a significant peak at the η mass of around 0.54 GeV/c^2. To determine approximately the η selection limits the spectrum is fitted analogously to the former $K^\pm\pi^\mp$ mass spectra. The fit results for the Gaussian function and the total χ^2/NDF value are given in Table 9. They show again a less well χ^2/NDF value and partially neglectable uncertainties, that are discussed in section 4.1.4.

	Reaction
Fit Parameter	$\eta \to \gamma\gamma$
Intensity I / Events $(0.004\ \text{GeV}/c^2)^{-1}$	34459.4 ± 202.2
Maximum m_0 / GeV/c^2	0.542 ± 0.000
Width σ / GeV/c^2	0.011 ± 0.000
χ^2/NDF	$1054.9/28.0 = 37.7$

Table 9: Fit parameters for the Gaussian function and the total reduced χ^2/NDF value of the fit of the inclusive $\gamma_i\gamma_j$ mass spectra for the $\eta' \to \gamma\pi^+\pi^-$ channel, as described in the text.

The $\pm 3\sigma$ surrounding of the Gaussian peak provides for both final state channels the η selection limits, which are

$$0.508\ \text{GeV}/c^2 < m(\gamma\gamma) < 0.576\ \text{GeV}/c^2. \tag{40}$$

In Figure 13 (b) and (c) the invariant $\gamma_i\gamma_j$ mass spectra of data are shown in black for both final states. The η mass peaks are well enclosed by the η selection limits, that are highlighted with black dashed lines. The green markers correspond to the scaled signal MC simulation. As expected, for the $\eta' \to \gamma\pi^+\pi^-$ channel in (b) it shows no η signal, whereas in (c) a huge η peak is observed for the $\eta' \to \eta\pi^+\pi^-$ channel, because the intermediate η state is a signal resonance in that case.

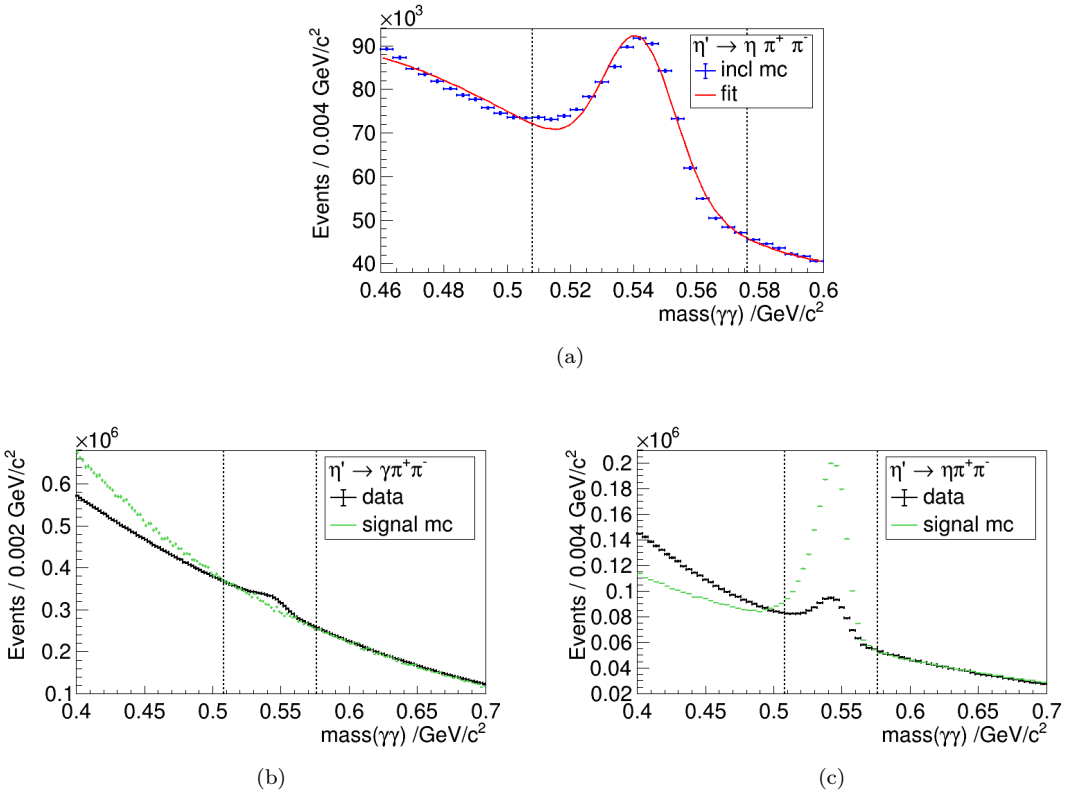

Figure 13: In (a) the invariant mass spectrum of $\gamma_i\gamma_j$ combinations with $i < j$ of the inclusive MC simulation (marked in blue) is shown for the $\eta' \to \eta\pi^+\pi^-$ channel. The η signal region is fitted by a sum over a Gaussian function and a polynomial function of third order, which is plotted in red. In (b) and (c) the invariant $\gamma_i\gamma_j$ mass spectra of data (in black) in comparison to the scaled signal MC simulation (in green) are presented for the $\eta' \to \gamma\pi^+\pi^-$ channel in (b) and for the $\eta' \to \eta\pi^+\pi^-$ channel in (c). The η cut limits are highlighted with black dashed lines.

The Four Constraint Kinematic Fit. To veto background components that stand out due to incorrect numbers or species of final state particles a cut of the four constraint (4C) kinematic fit is applied. The combination of final state particles of a single event that fulfils energy conservation (1C) and momentum conservation (+3C) with respect to the initial J/ψ state best is chosen as the best combination of this event. The assigned χ^2_{4C} value mirrors how good the energy and momentum conservation is satisfied by the best combination. Hence, the χ^2_{4C} value describes the quality of the kinematic fit. The smaller the χ^2_{4C} value the better the restrictions are fulfilled. Thus, one should naively select only events of smallest χ^2_{4C} values to suppress background maximally. But this approach causes a tremendous, statistical loss and loss of significance. Therefore, an optimal χ^2_{4C} cut value has to be determined, whereby the maximum of the so called **F**igure **O**f **M**erit FOM is taken. The χ^2_{4C}-dependent $\text{FOM}(\chi^2)_{\text{4C}}$ is calculated by integrating the χ^2_{4C} spectrum up to the corresponding χ^2_{4C} value, whereby two different approaches are used in this work:

1. To minimise the background components (minBack) the $\text{FOM}(\chi^2_{\text{4C}})$ is determined via [58]

$$\text{FOM}_{\text{minBack}}(\chi^2_{\text{4C}}) = \frac{(N_{\text{signalMC}})^2}{\sqrt{(N_{\text{data}})^3}}. \tag{41}$$

2. For achieving maximal significance (maxSig) of the signal part compared to the background the FOM(χ^2_{4C}) is defined as

$$\mathrm{FOM}_{\mathrm{maxSig}}(\chi^2_{4C}) = \frac{N_{\text{Signal MC}}}{\sqrt{N_{\mathrm{data}}}}, \tag{42}$$

where N_{signalMC} is the number of signal MC events and N_{data} the number of data events that pass the current χ^2_{4C} (cut) value[5]. It has to be mentioned that the estimation of FOMs via equation (41) and (42) is only valid, if the accepted MC simulation describes data sufficiently well. This holds true for this analysis, as can be seen in the appendix 6.2.
In the following, the two FOM approaches will be distinguished by indicating them as the "minimal background" approach (using eq. (41)) and the "maximal significance" approach (using eq. (42)).
The purpose to study the $\eta_c \to \eta' K^+ K^-$ decay by considering two different FOM approaches is, to be able to compare and evaluate the results. In general, the FOM approach of "maximal significance" is used in analyses. But, as can be seen in section 4.2, the significance of the signal part above the background is entirely sufficient in this analysis. Thus, there is no need for further significance maximisation. Instead, it is of central concern to minimise the background part as much as possible, to improve the results of the following PWA. Thus, the "minimal background" approach for the FOM determination is tested in this work in comparison to the conventional "maximal significance" approach.
In Figure 14 the χ^2_{4C} distributions of the signal MC simulation and of data are shown for both final states. Furthermore, the resulting FOM of "maximal significance" and of "minimal background" are pictured. For the $\eta' \to \eta\pi^+\pi^-$ channel in (b) the curves are plotted while fulfilling solely the general event selection criteria of section 4.1.1, whereas for the $\eta' \to \gamma\pi^+\pi^-$ channel in (a) additionally the η and K^{*0} cuts have been applied (otherwise, the corresponding FOM shows no maximum). In addition, the maximum of each FOM curve is marked and its value is taken for the χ^2_{4C} cut, respectively. They are compiled in the following list, that states, which events are rejected

$$\left.\begin{array}{r}\chi^2_{4C,\ \mathrm{maxSig}} > 23.8 \\ \chi^2_{4C,\ \mathrm{minBack}} > 15.8\end{array}\right\} \text{for } \eta' \to \gamma\pi^+\pi^-, \qquad \left.\begin{array}{r}\chi^2_{4C,\ \mathrm{maxSig}} > 24.6 \\ \chi^2_{4C,\ \mathrm{minBack}} > 14.8\end{array}\right\} \text{for } \eta' \to \eta\pi^+\pi^-. \tag{43}$$

The comparison of the χ^2_{4C} cut results reveals significant deviations between the two FOM approaches. The χ^2_{4C} cuts regarding the "minimal background" approach have considerably lower values as the ones of "maximal significance". But this comes up to expectations, since the background part gets smaller the lower the χ^2_{4C} cut is chosen.

The π^0 Cut. In order to reject background events, that contain the intermediate reaction $\pi^0 \to \gamma\gamma$, a cut on the 1C kinematic fit of specific two-photon combinations is used.
While combining the detected and filtered particles to the final state by the FSFilter package, also the pull of the best π^0 is estimated. This π^0 is composed of a final state photon and an arbitrary photon, that has also been detected by the EMC. In total up to ten photons are stored within one single event. Thus, assuming n final state photons $\gamma_{\mathrm{fs},i}$ (with $i = 1, 2, ..., n$), each of them is combined with up to nine other stored photons γ. Via a 1C kinematic fit the combination $\gamma\gamma_{\mathrm{fs},i}$ of the lowest $\chi^2_{1C,i}$ is searched and the combination of the minimum $\min(\chi^2_{1C,i})$ is stored as the pull of the best π^0 for the final state photon $\gamma_{\mathrm{fs},i}$. Thus, if the pull $\min(\chi^2_{1C,i})$ is small, the probability

[5] It is remarked, that the conventional FOM approach is based on an inclusive MC simulation split into the signal (S) and background part (B), whereby the signal part corresponds to the Signal MC simulation N_{signalMC} and the sum $S + B$ to data N_{data} in this work. But due to the fact, that the inclusive MC simulation does not contain any essential signal component, since the studied η_c decay is still unlisted in the PDG (that means $S \approx 0$), the usual approach fails here.

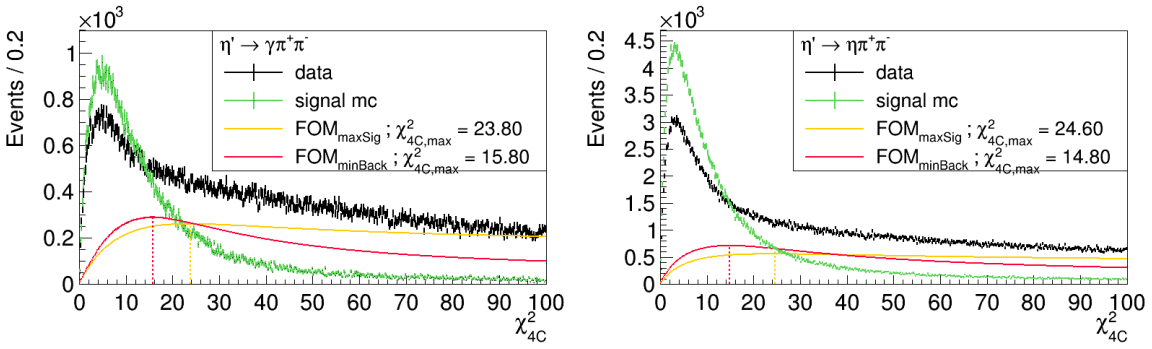

(a) (b)

Figure 14: The χ^2_{4C} distributions for data (marked in black) and for the signal MC simulation (marked in green). Additionally, the FOMs for the "maximal significance" approach (orange line) and for the "minimal background" approach (red line) are plotted using the same axis of ordinates as the χ^2_{4C} distributions. The highlighted FOM maxima define the optimal χ^2_{4C} cuts. In (a) the results for the $\eta' \to \gamma\pi^+\pi^-$ channel are shown, in (b) for the $\eta' \to \eta\pi^+\pi^-$ channel.

that the $\gamma\gamma_{\text{fs},i}$ combination results from a π^0 decay is high and vice versa. In the following, the minimum pull will assigned the variable Υ_i and it is given

$$\Upsilon_i \equiv \sqrt{\min\left(\chi^2_{1\text{C},i}\right)} \quad \Longrightarrow \begin{cases} \text{large} \;\to\; \text{probability for a } \pi^0 \to \gamma\gamma_{\text{fs},i} \text{ decay is low} \\ \text{small} \;\to\; \text{probability for a } \pi^0 \to \gamma\gamma_{\text{fs},i} \text{ decay is high} \end{cases} \tag{44}$$

But, depending on the number n of final state photons, one has to consider n corresponding Υ_i per event. In this work they will be combined to the event-based minimum $\Upsilon \equiv \min\left(\Upsilon_1, ..., \Upsilon_n\right)$. Hence, Υ gives the probability, whether an arbitrary final state photon γ_{fs} of an event results from a π_0 decay or not. Hence, this variable is appropriate to reject events containing $\pi^0 \to \gamma\gamma_{\text{fs}}$ decays. For that, an optimal cut value has to be determined, whereby all events with Υ smaller than this value will be rejected. Analogously to the previous χ^2_{4C} cut definition, the optimal Υ value is determined as the maximum of a corresponding FOM. Additionally, the FOM will be calculated using both approaches, the "minimal background" approach via equation (41) and the "maximal significance" approach via equation (42). In Figure 15 the Υ distributions of each final state are plotted logarithmically for the signal MC simulation and for data. The corresponding FOM curves for the "maximal significance" and "minimal background" approach are also shown. The FOM's maxima are highlighted and their values are used for the Υ and hence π^0 cut definition. All events with Υ values smaller than the following cut values are rejected

$$\left.\begin{array}{r} \Upsilon_{\text{maxSig}} < 4.0 \\ \Upsilon_{\text{minBack}} < 5.6 \end{array}\right\} \text{for} \;\; \eta' \to \gamma\pi^+\pi^-, \qquad \left.\begin{array}{r} \Upsilon_{\text{maxSig}} < 3.2 \\ \Upsilon_{\text{minBack}} < 4.4 \end{array}\right\} \text{for} \;\; \eta' \to \eta\pi^+\pi^-. \tag{45}$$

As expected, more events will be rejected using the FOM approach "minimal background" as the cut values $\Upsilon_{\text{minBack}}$ lie significantly above the Υ_{maxSig} values for each final state.

4.1.4 Discussion

In this section the different general and specific event selection criteria have been introduced, that are applied to data in this work. In the next section, their effective results, so far, will be presented and evaluated. But nevertheless, there is still potential for optimisations, in order to improve the

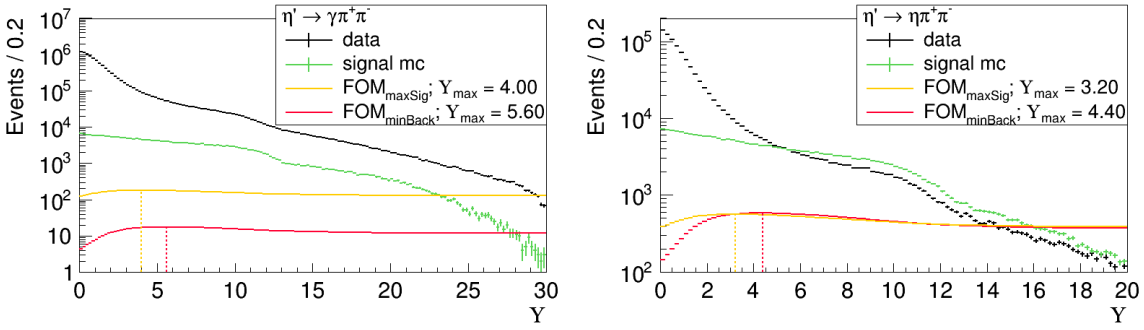

(a) (b)

Figure 15: Logarithmically plotted Υ distributions for data (marked in black) and for signal MC simulation (marked in green). Additionally, the FOMs for the "maximal significance" approach (orange line) and for the "minimal background" approach (red line) are shown using the same axis of ordinates as the Υ distributions. The highlighted FOM maxima define the optimal Υ cut values. In (a) the results for the $\eta' \to \gamma\pi^+\pi^-$ channel are pictured, in (b) for the $\eta' \to \eta\pi^+\pi^-$ channel.

background reduction procedure.
First of all, the presented $K^*(892)^0$ and η mass cuts have been defined by fitting the corresponding invariant mass spectra of the inclusive MC simulation (see Fig. 11 and Fig. 13 (a)). But the reduced χ^2/NDF values of the total fit curves, that are way above the expected value of about one, and the partially neglectable uncertainties for several fit parameters reveal large potential for improvement of the fit. The bad χ^2/NDF values are based on the one hand on the large number of inclusive MC events. This leads to small uncertainties, that constrain the fit. On the other hand, the chosen fit function of a pure Gaussian function for the signal parts is not appropriate, as the signal line shapes rather have to be described by a convolution of a Breit-Wigner distribution and a Gaussian function. This would also lead to reasonable uncertainties for the fit parameters. However, the chosen fit approach for the estimation of mass cut limits has been judged as being sufficient within the scope of this work, but should be improved in future. Furthermore, besides the chosen $\pm 3\sigma$ surrounding of the Gaussian peaks for defining the mass cut limits, also smaller or larger ranges should be considered.
The π^0 intermediate resonances have been rejected via a cut onto the pull Υ of the best π^0. But there are other possible π^0 cut definitions. For example, another frequently used approach is, to apply a π^0 mass cut onto the best $\gamma_i\gamma_j$ combination (with $i < j$) of all stored photons per event. This approach is much stricter, since it generates hard cuts that, however, may cause artefacts. In contrast, the chosen π^0 cut via the Υ distribution only takes $\gamma\gamma$ combinations into account, that contain at least one final state photon. A comparison between both π^0 cut approaches could be useful especially concerning the PWA results.
Furthermore, the chosen specific event selection criteria are based on the main background components, which have been observed within the inclusive MC simulation (see Tab. 7). But there are other, however, less dominant background components. Some of them could be studied likewise and reduced via specific selection conditions.
Finally, systematic studies in general need to be done, in order to optimise the background reduction procedure. For that, the optimal χ^2_{4C} and Υ cut values could be changed stepwise above and below the current values, while evaluating the results concerning background reduction and significance optimisation.

4.2 Evaluation of the Event Selection

In this section the presented and applied event selection criteria of the previous section are evaluated by studying several invariant mass spectra of concern in this work.
At first, the 2D histograms of the invariant mass of η_c candidates against the mass of η' candidates are analysed with respect to the reached significance of η_c-η' coincidences (see sect. 4.2.1). Via these coincidences the $\eta_c \to \eta' K^+ K^-$ decay is found. Afterwards, the invariant mass spectra of η' candidates are studied qualitatively concerning the achieved background reduction (see sect. 4.2.2). Since there is still some non-η' background left, which might contribute to the η_c signal, a so called sideband subtraction method is implemented. Thereafter, the sideband subtracted invariant mass spectra of η_c candidates are analysed (see sect. 4.2.3), since they provide the base for the following determination of the $\eta_c \to \eta' K^+ K^-$ branching ratio in section 4.3 via a PWA.
All pictured mass spectra in this section are based on the "minimal background" approach. The corresponding spectra for the "maximal significance" approach can be found in the appendix 6.3. A first brief comparison between both FOM approaches is given at the end of this section in 4.2.4, where the results of the applied event selections are conclusively discussed.

4.2.1 2D Histograms of the Invariant Masses of η_c against η' candidates

Since coincidences between two particles give evidence for a decay correlation, the 2D histograms of the invariant masses of η_c against η' candidates are studied to search for the $\eta_c \to \eta' K^+ K^-$ decay at BESIII. Thus, in Figure 16 the corresponding 2D histograms of data are pictured on the left for both final state channels, whereby the η_c is reconstructed via the $\eta' K^+ K^-$ mass and the η' with regard to the final state channel. For comparison, the inclusive MC simulations are shown on the right. For further comparison purposes, the following histograms are plotted at first without using any of the general or specific selection conditions introduced in section 4.1, despite the implemented criteria in the FSFilter package. Below, the corresponding histograms with applied cuts are presented.
Considering the four histograms in Figure 16, solely in the data plots on the left a clear yellow spot is visible, that is located at the η' mass of about 0.98 GeV/c^2 and at the η_c mass of around 2.98 GeV/c^2. Thus, in data a clear coincidence for the occurrence of an η' meson and an η_c meson, that decays into $\eta' K^+ K^-$, is observed in both final state channels. It carries a high number of events in comparison to the spot's immediate surrounding. In contrast, no similar event accumulation at the η_c-η' coincidence can be seen in the inclusive MC simulations on the right of Figure 16. But this comes up to expectations, since the decay $\eta_c \to \eta' K^+ K^-$ is not included in the inclusive MC simulation, yet. Thus, it can be concluded:

> *The decay $\eta_c \to \eta' K^+ K^-$ is experimentally observed at BESIII using the world's largest J/ψ data sample.*

However, besides the clearly visible η_c-η' coincidences in data, a high amount of background comes to appearance in Figure 16. For instance, left above the η_c-η' spot a yellow more longish region occurs. It is visible in both final state channels as well as in data and inclusive MC simulation. Background studies via the inclusive MC simulation have revealed (see sect. 4.1.2), that this background component is caused by missing photons. It is rejected completely via the radiative photon energy condition of $E_{\gamma_r} > 0.06$ GeV. Also the further remaining background next to the η_c-η' spot has been effectively and significantly reduced via the event selection criteria of section 4.1. This can be seen in Figure 17, which shows the 2D histograms of data after applying all selection conditions. The corresponding 2D data histograms of the "maximal significance" approach show similar results, but with a slightly higher remaining background level (see Fig. 36 in the appendix 6.1).

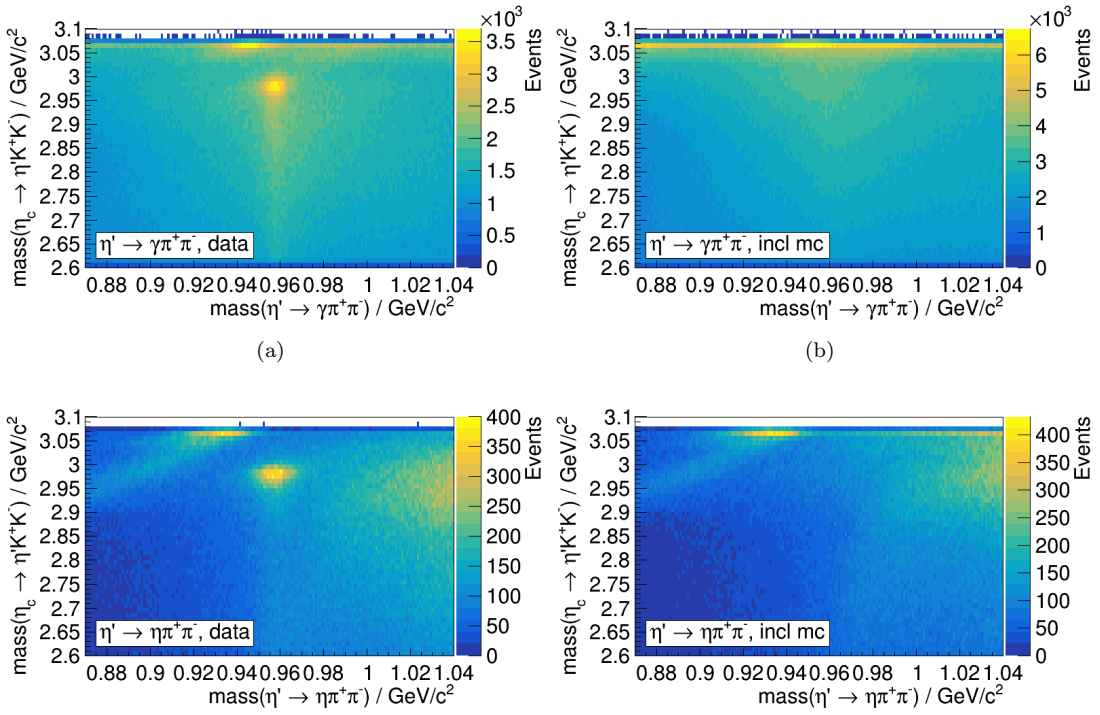

Figure 16: 2D histograms of data on the left and of inclusive MC simulation on the right for the "minimal background" approach without using any event selection criteria, despite the rough cuts implemented in the FSFilter package. The invariant mass of η' candidates is plotted against the invariant mass of η_c candidates, that are reconstructed via the $\eta' K^+ K^-$ mass. The colour of a single bin shows the number of events. In the top row the channel $\eta' \to \gamma\pi^+\pi^-$ is considered, below the $\eta' \to \eta\pi^+\pi^-$ channel.

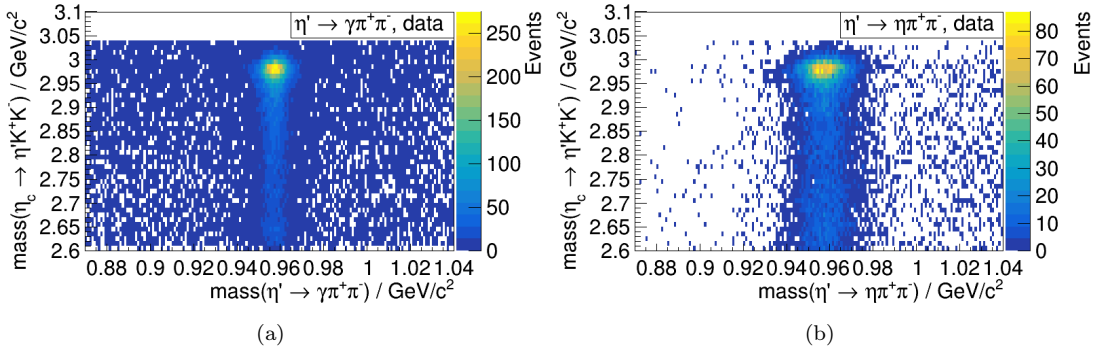

Figure 17: 2D histograms of data for the "minimal background" approach after applying the event selection criteria of sect. 4.1. The invariant masses of η' against η_c candidates are plotted,, whereby the η_c is reconstructed via the $\eta' K^+ K^-$ mass. The colour of a single bin shows the number of events. On the left the $\eta' \to \gamma\pi^+\pi^-$ channel is shown, on the right the $\eta' \to \eta\pi^+\pi^-$ channel.

However, the cutted 2D histograms of data of both FOM approaches reveal that on the left and right of the η_c-η' coincidence background components are still left. They are supposed to be present also under the η_c-η' spot. Thus, in the following the invariant mass spectra of η' candidates are analysed, which offer the opportunity via the sideband subtraction method to reduce the non-η' background contributions under the η_c signal.

4.2.2 The Invariant Mass Spectra of η' candidates and Sideband Subtraction

The invariant mass spectra of η' candidates, that result after applying the event selection criteria of section 4.1, are considered in more detail in the following.

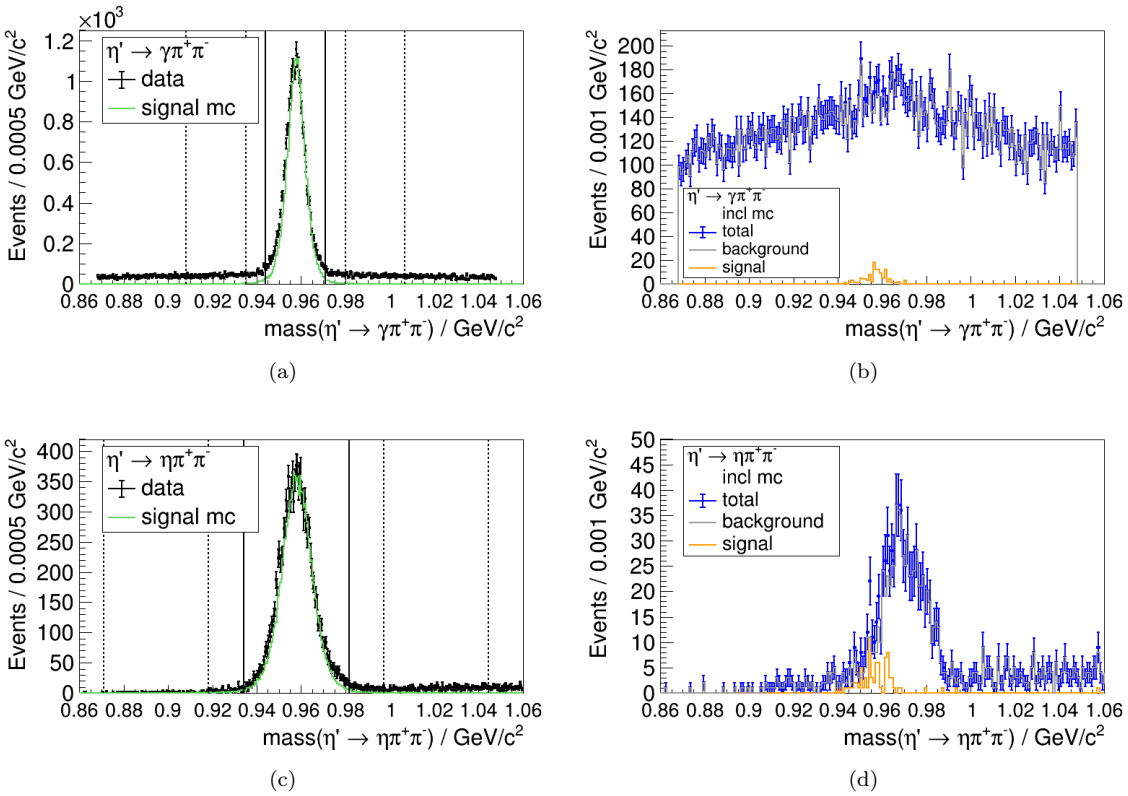

Figure 18: The invariant mass spectra of η' candidates for the "minimal background" approach of data on the left (marked in black). In addition a scaled signal MC simulation is added with a green line. On the right inclusive MC simulations are pictured. The orange lines represent the signal events of the correct final state, the grey lines show the corresponding background events of the false final state. The total inclusive MC simulation is marked in blue. In the top row the channel $\eta' \to \gamma\pi^+\pi^-$ is considered, below the $\eta' \to \eta\pi^+\pi^-$ channel.

In Figure 18 the invariant mass spectra of η' candidates are pictured for data on the left and for the inclusive MC simulation on the right. In the top row the $\eta' \to \gamma\pi^+\pi^-$ channel is shown, in the bottom row the channel $\eta' \to \eta\pi^+\pi^-$. As expected via the previous 2D histograms of Figure 17, the two data plots in figure 18 show a strong signal at the η' mass of 0.96 GeV/c^2 sitting on

a very low background level. It confirms the achieved high significance of the η' signal above the background. Analogous results are obtained for the invariant mass spectra of η' candidates of the "maximal significance" approach (see Fig. 37 in the appendix 6.1).
In the data plots the signal MC simulation is added as green line, which is scaled in such a way, that it is comparable with data. It reveals a good agreement between data and signal MC simulation concerning the η' signal. Moreover, as expected, additional background is observed in data next to the η' signal, that is not present in the MC simulation.
The background to the left and right of the η' peak in data is supposed to lie also under the η' signal region and hence also under η_c signal. Its general structure can be analysed via the inclusive MC simulation shown on the right of Figure 18. There, the inclusive MC simulation is split into the signal (orange line) and background contributions (grey line), whereby a signal event is determined as an event of the correct final state and a background event as an event of the false final state. The inclusive MC simulation in total is marked in blue. For both final state channels the inclusive MC simulation shows no essential signal contribution of the correct final state. Instead, the background part below the η' signal results almost exclusively due to events of the false final state. It will be treated by a sideband subtraction method. Since the inclusive MC simulation does not incorporate the true signal reaction $\eta_c \to \eta' K^+ K^-$ (as it is not listed in the PDG [12]), the signal parts in Figure 18 (b) and (d) (orange lines) contain exclusively contributions, that do not belong to the true signal part. They have solely the correct final state. Thus, the inclusive MC simulations also reveal, that essentially no incorrect signal (with only the right final state) lies under the η' peak, which may cover the true data signal.

To apply the sideband subtraction method, two sideband regions and a signal region are determined by fitting the mass spectra of η' candidates of data. It is presented in more detail in the following.

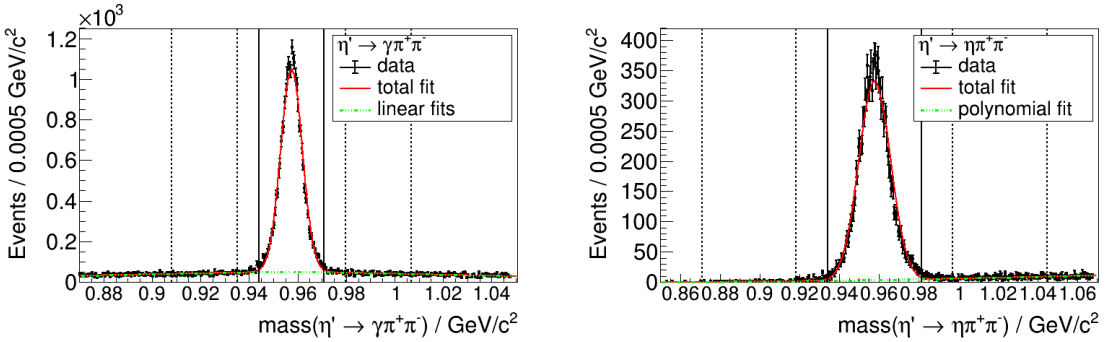

(a) (b)

Figure 19: Fit results of the invariant mass spectra of η' candidates of data for the "minimal background" approach. On the left the channel $\eta' \to \gamma\pi^+\pi^-$ is considered, on the right the $\eta' \to \eta\pi^+\pi^-$ channel. Data points are marked in black, the total fit as red line and the background components of the fit as green dotted line. With black (dashed) vertical lines the signal and sideband region limits are highlighted for applying the sideband subtraction method.

In Figure 19 the invariant mass spectra of η' candidates of data are pictured once again for both final state channels. For the $\eta' \to \gamma\pi^+\pi^-$ channel on the left the η' signal is fitted with a Gaussian function, since the width of the η' meson of (0.188 ± 0.006) MeV/c^2 [12] is significantly smaller than the resolution of the BESIII detector. Thus, the line shape of the η' signal mirrors the Gaussian-

shaped detector resolution rather than the natural η' width. The background to the left and right of the η' signals shows no significant resonances and seems to be triangle-shaped. It is supposed that the triangle-shape continues also underneath the η' peak, like it is observed in the inclusive MC simulation in Figure 18 (b). The triangle-shape results from the applied η' selection (see sect. 4.1.1). Out of the two final state photons, the photon that yields the best $\eta' \to \gamma\pi^+\pi^-$ is chosen. This selection becomes more probable, when the combination lies closer to the nominal η' mass, resulting in the observed line shape.
Thus, initially the mass spectrum of η' candidates for the $\eta' \to \gamma\pi^+\pi^-$ channel is fitted by two linear functions, that describe the background part to the left and right of the η' signal and intersect at the η' peak position, while excluding the η' signal region. Afterwards, the background fit results are used for a total fit, that is composed of a Gaussian function and the two linear functions. Both fits are based on the binned likelihood method that includes empty bins due to the low background statistic present here.
The corresponding invariant mass spectrum of η' candidates of the $\eta' \to \eta\pi^+\pi^-$ channel is fitted similarly (see Fig. 19 (b)). Solely the fit function for the η' background is chosen different. Here, a polynomial function of second order is used to account for the background's monotonous increase towards higher masses.
The total fit results for both η' candidate mass spectra are plotted as red lines in Figure 19 and the background components as green dotted lines. Additionally, the fit results for the Gaussian functions, that show partially neglectable uncertainties for the maximum and width, and the χ^2 values for the background and total fits are summarised in Table 10.
The corresponding fitted mass spectra of η' candidates for the "maximal significance" approach are pictured in the appendix 6.1 in Figure 38 and the fit results are summarised in Table 15.

"Minimal Background"	**Final State Channel**	
Fit Parameter	$\eta' \to \gamma\pi^+\pi^-$	$\eta' \to \eta\pi^+\pi^-$
Background χ^2/NDF	$325.43/301.00 = 1.08$	$187.99/275.00 = 0.68$
Total Fit χ^2/NDF	$507.41/357.00 = 1.42$	$514.67/435.00 = 1.18$
Intensity I / Events (0.004 GeV/c^2)$^{-1}$	995.32 ± 8.90	330.87 ± 3.70
Maximum m_0 / GeV/c^2	0.9574 ± 0.0000	0.9578 ± 0.0001
Width σ / GeV/c^2	0.0045 ± 0.0000	0.0079 ± 0.0001
Weight	0.58 ± 0.01	0.41 ± 0.01

Table 10: Results for the fit parameters of the Gaussian function and the χ^2 values for the background and total fit of the invariant mass spectrum of η' candidates of data for both final state channels for the "minimal background" approach. Via the Gaussian width a signal and two sideband regions are defined. The resulting sideband weights via equation (46) are given.

The fits of the η' candidate mass spectra enable the definition of limits for sideband and signal regions. The signal region is defined as the $\pm 3\sigma$ surrounding of the obtained Gaussian maximum for the η' peak position. The two sideband regions are chosen to the left and right of the fitted η' peak position from -11σ to -5σ and from 5σ to 11σ. The resulting limits are highlighted with black (dashed) vertical lines in Figure 18 and 19.
For performing the sideband subtraction method, the weight of the sidebands has to be determined. It is given by

$$\text{weight} = \frac{N_{\text{signal}}}{N_{\text{sb-l}} + N_{\text{sb-r}}}, \tag{46}$$

where N_{signal} is the number of events in the signal region and $N_{\text{sb-l}}$ and $N_{\text{sb-r}}$ are the numbers of events in the left and right sidebands. The resulting sideband weights for both final state channels are also listed in Table 10.
Afterwards, two histograms are defined. A "sideband" histogram of weighted η_c candidates, that lie within the η' sideband regions, and a "signal histogram" of unweighted η_c events, that lie in the η' signal region. By subtracting the "sideband histogram" from the "signal histogram" an η'-sideband subtracted mass spectrum of η_c candidates is generated. These mass spectra are presented and analysed in the following section.

4.2.3 The Invariant Mass Spectra of η_c Candidates

Since the mass spectra of η_c candidates are used in this work to determine the $\eta_c \to \eta' K^+ K^-$ branching ratio via a PWA fit approach, a background level as low as possible is required. Thus, in this section the sideband subtracted invariant mass spectra of η_c candidates are studied concerning the achieved background reduction.

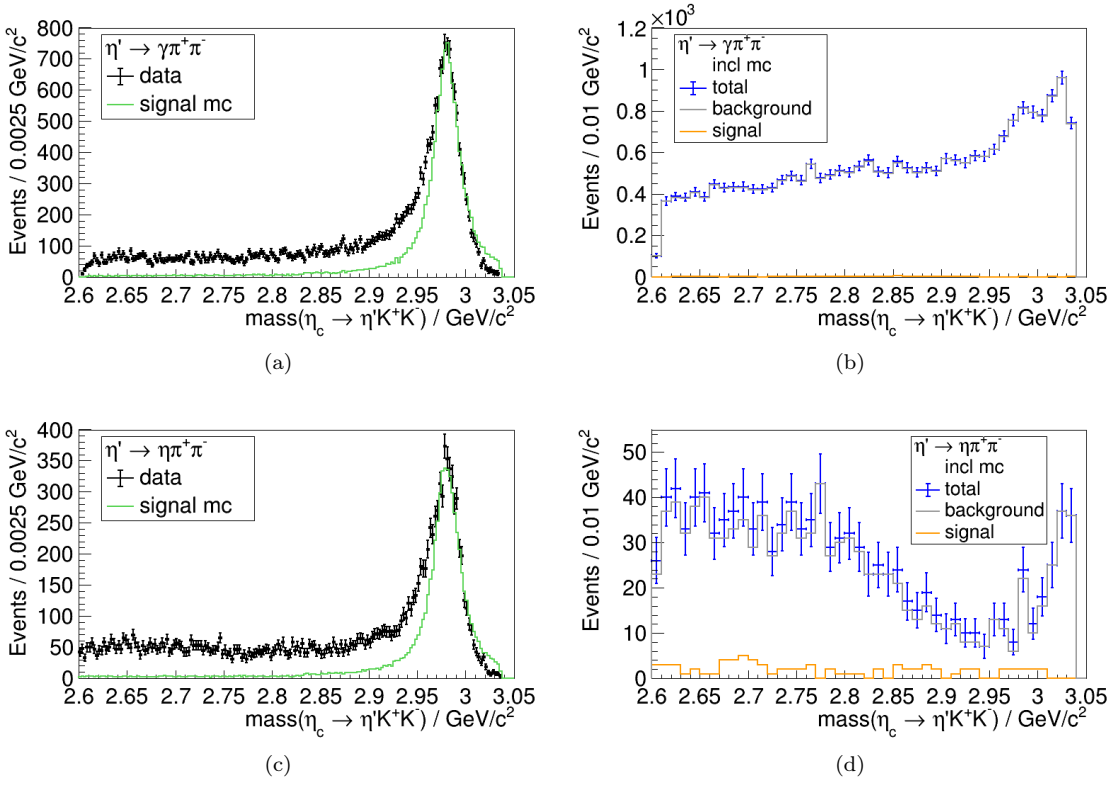

Figure 20: The sideband subtracted invariant η_c mass spectra of data on the left (marked in black) for the "minimal background" approach. The scaled signal MC simulation is added as green line. On the right the (non-sideband subtracted) inclusive MC simulations are pictured. With orange and grey lines the signal, respectively background contributions are shown, that have the correct, respectively false final state. The total inclusive MC simulation is marked in blue. In the top row the channel $\eta' \to \gamma\pi^+\pi^-$ is considered, below the $\eta' \to \eta\pi^+\pi^-$ channel.

In Figure 20 on the left the sideband subtracted invariant mass spectra of η_c candidates of data (marked in black) are presented for both final state channels, whereby the η_c mass is reconstructed via the $\eta' K^+K^-$ mass. In each spectrum a strong signal at the η_c mass of 2.98 GeV/c^2 is observed sitting on a low, non-constant background. Furthermore, the η_c signals show the expected asymmetric line shape, which results from the radiative M1 decay of J/ψ to $\gamma\eta_c$ (see sect. 2.2.2). In contrast, the added and scaled signal MC simulation (green line) does not feature the η_c asymmetry. However, it shows a good agreement with data regarding the η_c peak position.
On the right of Figure 20 the inclusive MC simulations are pictured[6]. Both spectra show no essential signal contribution. Instead, the remaining background under the η_c signal results almost solely from reactions of the false final state. The corresponding invariant η_c mass spectra of the inclusive MC simulation and of data for the "maximal significance" approach reveal analogous results (see Fig. 39 in the appendix 6.1).
To evaluate the results of the sideband subtraction, the η_c-sideband mass spectra of data are presented in Figure 21. The two spectra contain a comparatively low number of events, but neither for the $\eta' \to \gamma\pi^+\pi^-$ channel on the left, nor for the $\eta' \to \eta\pi^+\pi^-$ channel on the right an η_c signal or other peaking background is observed. Hence, applying the sideband subtraction method onto the mass spectra of η_c candidates provides a further efficient background reduction underneath the η_c signal without loss of significance. The same results are obtained for the η_c-sideband mass spectra of the "maximal significance" approach (see Fig. 40 in the appendix 6.1).

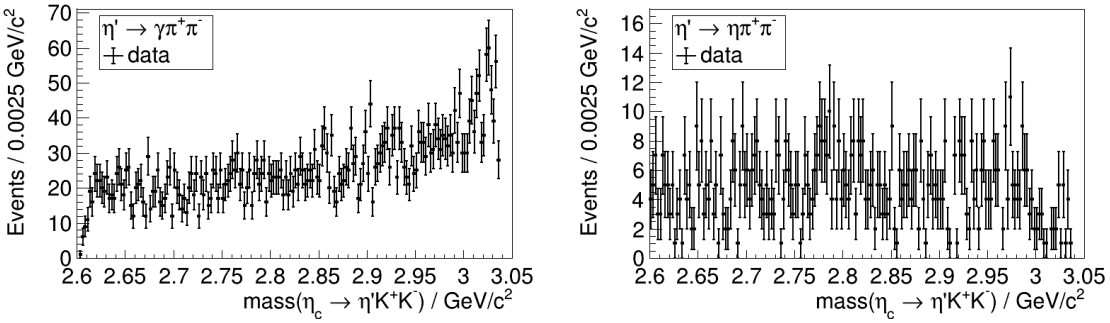

(a) (b)

Figure 21: Invariant η_c-sideband mass spectra of data for the "minimal background" approach. The spectra are filled with η_c events, that are reconstructed via $\eta' K^+K^-$ and solely lie in the η' sidebands as defined in sect. 4.2.2. On the left the channel $\eta' \to \gamma\pi^+\pi^-$ is pictured, on the right the $\eta' \to \eta\pi^+\pi^-$ channel.

4.2.4 Discussion

The presented invariant mass spectra and 2D histograms of data in this section reveal, that a very high significance of signal above background has been achieved. Furthermore, the background level itself has been reduced efficiently. Thus, the observation of the $\eta_c \to \eta' K^+K^-$ decay within the BESIII experiment has been accomplished via a high significance of η_c-η' coincidences.
Hence, the results of this section confirm the so far effectively working event selection criteria and sideband subtraction method presented in section 4.1 and 4.2.2. Nevertheless, there is further

[6]The invariant η_c candidate mass spectra of the inclusive MC simulation are not sideband subtracted, since the number of events in the η' signal in the inclusive MC simulations in Figure 18 (b) and (d) are too low for a convincing fitting to apply the sideband subtraction method.

potential for improvement, concerning the sideband subtraction method in particular.
In Figure 22 (a) a detail of Figure 19 (a) is presented. It shows the fitted invariant η' candidate mass spectrum of data for the $\eta' \to \gamma\pi^+\pi^-$ channel. The detail reveals, that the triangle-shape assumption for the background part is not quite justified. Especially on the left of the η' signal, structures are observed, that cause a slightly non-linear shape of the background. Thus, further background studies are required, for instance, by analysing the inclusive MC simulation. First studies reveal, that the structures do not result due to muons, which have been incorrectly identified as final state pions by the particle identification system of BESIII.

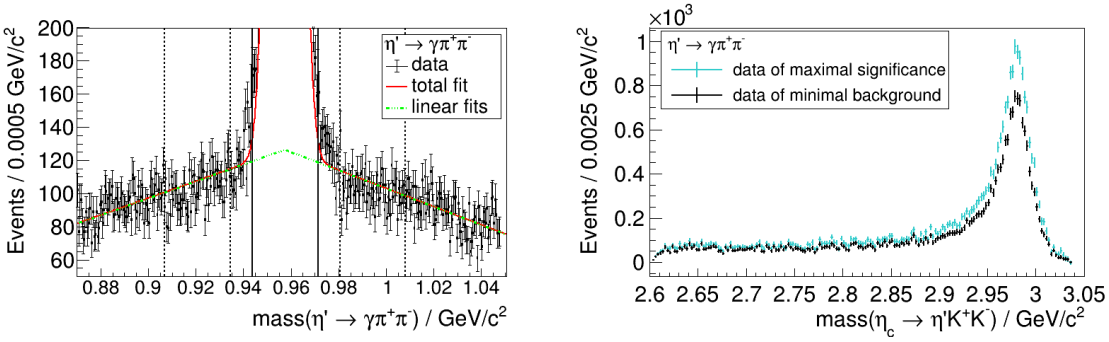

(a) (b)

Figure 22: (a) Detail of Figure 19 (a), that shows the fitted invariant η' candidate mass spectrum of data for the "minimal background" approach of the $\eta' \to \gamma\pi^+\pi^-$ channel. The data points are marked in black, the total fit as red line and the fit of the assumed triangle-shaped background as green dashed line. Additionally, the η' signal region and sidebands are highlighted via vertical black (dashed) lines. (b) The η'-sideband subtracted invariant mass spectrum of η_c candidates of data for the $\eta' \to \gamma\pi^+\pi^-$ channel for both FOM approaches in the same plot. The mass spectrum of the "minimal background" approach is marked in black, the spectrum of "maximal significance" in light blue.

In the following a first brief comparison between the two FOM approaches is presented.
In Figure 22 (b) the invariant η_c candidate mass spectra of both FOM approaches are pictured in the same plot, exemplary for the $\eta' \to \gamma\pi^+\pi^-$ channel. The data of "maximal significance" (marked in light blue) lies constantly slightly above the data of "minimal background" (marked in black). Thus, the FOM approach of "minimal background" further reduces the background level as expected, but also the signal component is reduced likewise. Hence, it seems there is a purely statistical loss from using the "maximal significance" approach to the "minimal background" method.
But due to the fact, that the background component underneath the η_c signal is non-constant, further comparative analyses are required to verify or discount the assumption of a purely statistical difference between both FOM approaches. This is done via the results of the performed PWAs, which is considered in the next section in detail.

4.3 Partial Wave Analysis

After the final event selection discussed in section 4.1 and evaluated in section 4.2 a partial wave analysis is carried out via two PWA hypotheses as described in section 4.3.1. The PWA fit results are presented and discussed in section 4.3.2. The results are used in order to determine the branching ratio $BR_{\eta_c \to \eta' K^+ K^-}$ (see sect. 4.3.3) as well as to investigate qualitatively intermediate resonances in the K^+K^- system, especially the possible isoscalar scalar contributions $f_0(1370)$, $f_0(1500)$ and $f_0(1710)$ (see sect. 4.3.4). All results are compared to the theoretical predictions presented in section 2.3.

4.3.1 Implementation of two PWA Hypotheses

In this analysis the PWA is performed using the software package **PA**rtial **W**ave **I**nteractive **AN**alysis PAWIAN, which has been developed at the Ruhr University Bochum [59]. Thus, the PWA is carried out as an unbinned maximum likelihood fit, whereby the minimisation is done by MINUIT2. Details on the likelihood construction can be found for example in [59] or [60].
In the following the structure of the performed PWA is presented. The full decay chain, the PWA is based on, is schematically shown in Figure 23.

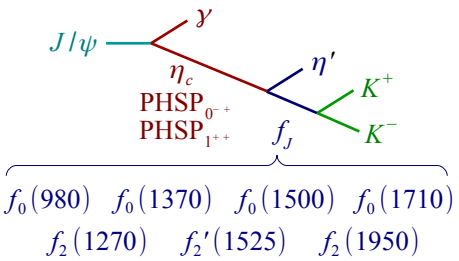

Figure 23: Illustration of the J/ψ decay chain in the isobar model. The J/ψ decays radiatively either into η_c or into background contributions containing events evenly distributed in phase space PHSP with $J^{PC} = 0^{-+}$ or $J^{PC} = 1^{++}$. While the η' meson is treated as a final state particle in the model, the f_J contributions decay further into K^+K^-, whereby for the f_J contributions the seven resonances listed under the brace are considered.

The full decay chain is described as a series of two-body decays (isobar model). First, the J/ψ decays radiatively either into η_c or into non-resonant background contributions. The latter contain events evenly distributed in **PH**ase **SP**ace PHSP and have a total angular momentum limited to $J \leq 1$ here. Thus, with regard to the conservation of CP parity and the total angular momentum J, non-resonant $J^{PC} = 0^{-+}$ and $J^{PC} = 1^{++}$ background contributions are allowed and implemented. This is done in order to account for remaining non-resonant background below the η_c signal and to account for possible interference effects between the η_c and these background contributions.
Both the η_c meson and the two background contributions further decay into f_J and η', whereby the η' meson is treated as a final state particle in the model. Hence, the formerly considered two η' channels can be treated with one single combined PWA approach. For the f_J contribution decaying to K^+K^- seven resonances are considered as possible candidates, that conserve CP parity and total angular momentum J, which is limited here up to $J = 2$. Thus, the four isoscalar scalars $f_0(980)$, $f_0(1370)$, $f_0(1500)$ and $f_0(1710)$ and the three isoscalar tensor resonances $f_2(1270)$, $f_2'(1525)$ are implemented. Hence, the whole PWA decay tree combines in total 3×7 sub-decay chains, whereby each is composed of three two-body decays and described analogously to equation (31) and (32).

The radiative photon γ and pseudoscalar mesons η' and $K^{\pm}$ are defined as the final state particles and provide via their event-based four momenta the input data for the PWA. However, only events are taken into account, that lie in the η' signalband or in the sidebands (as defined in sect. 4.2.2), whereby the sideband events are weighted according to the negative weights that are listed in Table 10 and 15.

Now, the description of the angular and dynamical parts of the included two-body decays are considered in detail.
The angular amplitudes of the radiative decays $J/\psi \to \gamma X$ with X being $\text{PHSP}_{0^{-+}}$, $\text{PHSP}_{1^{++}}$ or η_c are described in the radiative multipole basis according to equation (16). The angular amplitudes of all other decays within the PWA-decay tree in Figure 23 are treated in the LS basis (see eq. 18). Each amplitude includes the complex factor α, that is separated into a magnitude and phase. However, only one factor α per sub-decay chain is used as a free fit parameter for the PWA, while the other two are fixed. Without loss of generality, one single phase of all 3×7 sub-decay chains is additionally fixed, so that the other phases are determined relatively to the fixed one.
The dynamical part of the decay amplitudes are parameterised as follows. The η_c line shape is described via a relativistic Breit-Wigner amplitude $BW(m)$ according to equation (19), with parameters fixed to the mass and width of the η_c meson as stated in the PDG [12] and listed in Table 11. Furthermore, a special form factor $C(m)$ taken from [20] is used

$$C(m) = a^3 e^{-\frac{a^2}{8\kappa^2}} \quad \text{with} \quad a = \frac{1}{2}\left(M_{J/\psi} - \frac{m^2}{M_{J/\psi}}\right). \tag{47}$$

It accounts for the asymmetric line shape of the η_c (discussed in sect. 2.2.2). The J/ψ mass is set to the PDG value $M_{J/\psi} = 3096.9$ MeV/c^2 [12], while the factor κ is determined as $\kappa = 0.065$ GeV/c^2 in [20].
The two non-resonant $\text{PHSP}_{0^{-+}}$ and $\text{PHSP}_{1^{++}}$ contributions are parameterised as broad relativistic Breit-Wigner amplitudes, whereby their masses and widths act as free parameters, that are constrained to the limits listed in Table 11.

So far, the two implemented PWA hypotheses in this work are identical. The differences between them arise from the parameterisation of the considered f_J resonances as described in the following.

The "K-Matrix PWA". Within the first PWA approach, the isoscalar scalar f_0 resonances are described by the K-matrix approach of V. V. Anisovich and A. V. Sarantsev [41] as presented in equation (26). Their solution is based on data up to $m(K\overline{K}) < 1.9$ GeV/c^2 and incorporates the five meson channels $\pi\pi$, $K\overline{K}$, $\eta\eta$, $\eta\eta'$ and 4π as well as the five fixed poles $f_0(500)$, $f_0(980)$, $f_0(1370)$, $f_0(1500)$ and $f_0(1710)$. The corresponding pole-dependent production strengths β and the production constants f^{prod} of the $K\overline{K}$ channel (see eq. (30)) act as free fit parameters for the PWA.
The isoscalar tensor f_2 resonances are described by single relativistic Breit-Wigner amplitudes via equation (19) with masses and widths fixed to the PDG values (see Tab. 11).
The "K-Matrix PWA" is based on in total 65 free fit parameters.

The "Breit-Wigner PWA". For the second PWA hypothesis both the isoscalar scalar f_0 resonances as well as the isoscalar tensor f_2 contributions are parameterised as relativistic Breit-Wigner amplitudes using equation (19). The fixed masses and widths that are used are also listed in Table 11. In total, the "Breit-Wigner PWA" is based on 53 free fit parameters.

Furthermore, the two PWA hypotheses are carried out for both FOM approaches, the "minimal background" approach and the "maximal significance" approach.

Contribution	**Mass / GeV/c^2**		**Width / GeV/c^2**	
	Low	High	Low	High
"K-Matrix PWA" and "Breit-Wigner PWA"				
η_c	2.9836		0.0322	
$\mathrm{PHSP}_{0^{-+}}$	2.3	3.1336	0.1	1.0
$\mathrm{PHSP}_{1^{++}}$	2.3	3.1336	0.1	1.0
$f_2(1270)$	1.275		0.185	
$f_2'(1525)$	1.5252		0.076	
$f_2(1950)$	1.944		0.472	
"Breit-Wigner PWA"				
$f_0(980)$	0.98		0.05	
$f_0(1370)$	1.35		0.35	
$f_0(1500)$	1.505		0.105	
$f_0(1710)$	1.72		0.15	

Table 11: Masses and widths of the contributions incorporated in the PWA hypotheses. Fixed values correspond to the world average values stated in the PDG [12]. The free parameters for the masses and widths of the $\mathrm{PHSP}_{0^{-+}}$ and $\mathrm{PHSP}_{1^{++}}$ contributions are limited as stated.

4.3.2 The PWA-Fit Results

In the following, the PWA-fit results are presented. They are shown exemplary for the "K-Matrix PWA" and "Breit-Wigner PWA" using the "minimal background" approach in Figure 24 - 29. The first two Figures 24 and 25 picture the "K-Matrix PWA" results for the $\eta' \to \gamma\pi^+\pi^-$ channel and the second two Figures 26 and 27 the results for the $\eta' \to \eta\pi^+\pi^-$ channel. Figure 28 and 29 show the results for the "Breit-Wigner PWA" for the $\eta' \to \eta\pi^+\pi^-$ channel.
For each PWA solution the projections of the PWA fit to different invariant masses and the corresponding helicity decay angular distributions are presented. Furthermore, each spectrum shows besides the data (marked in black) and the total PWA fit result (red line) also individual components of the fit. The total fits are either separated solely into the η_c signal component and the two non-resonant background contributions $\mathrm{PHSP}_{0^{-+}}$ and $\mathrm{PHSP}_{1^{++}}$, or the η_c and two background components are additionally separated into the f_0 and f_2 contributions as indicated in the legends. For the presentation of the "Breit-Wigner PWA" fit results also the separation into the single f_J contributions in chosen.
Underneath each spectrum the residuum is pictured showing the deviation of each data point from the total fit line. In its right upper corner the corresponding χ^2 value of the PWA fit projection is stated.
The spectra for the "maximal significance" approach can be found in the appendix 6.3, where all PWA fit results of this analysis are printed and sorted by the two PWA approaches.

"K-Matrix PWA" with "Minimal Background" for the $\eta' \to \gamma\pi^+\pi^-$ Channel

Projections to Invariant Masses

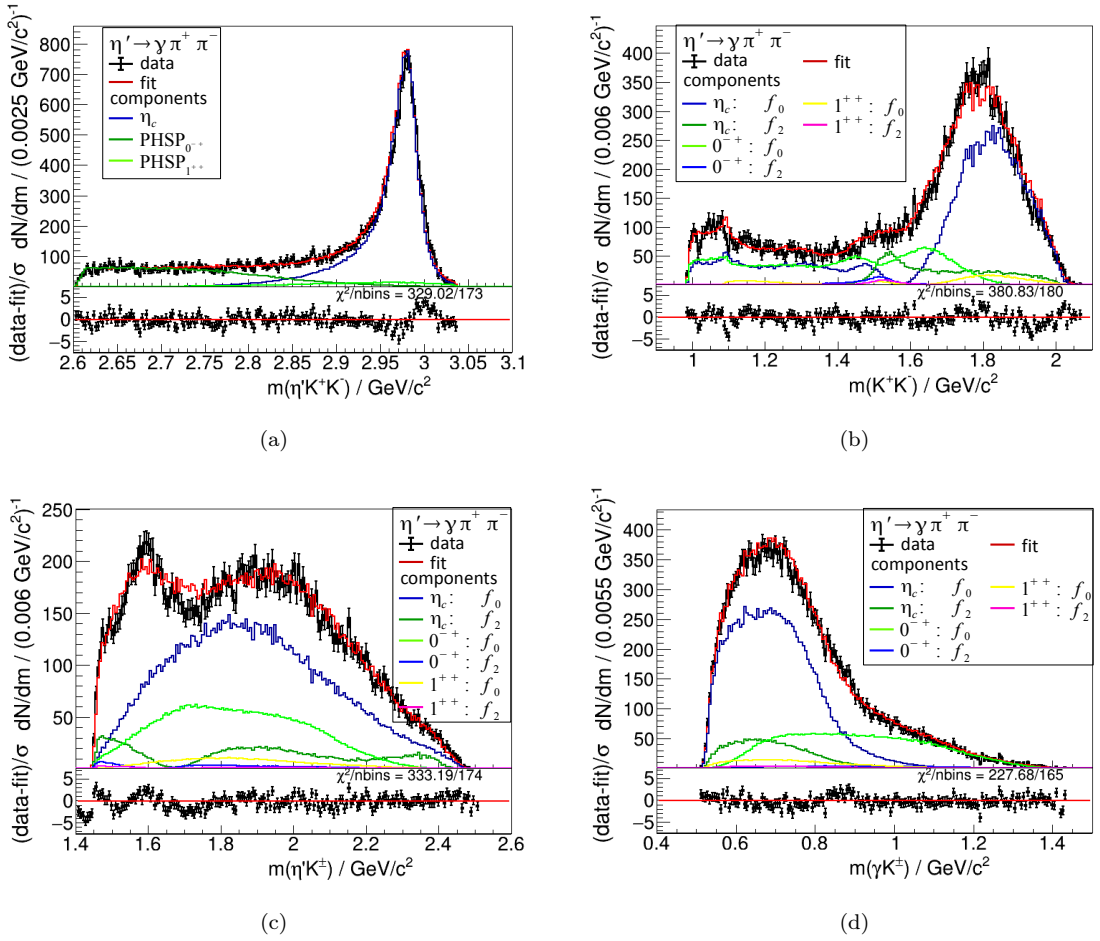

Figure 24: Projections of the PWA-fit results to different invariant masses for the "K-matrix PWA" with "minimal background" for the $\eta' \to \gamma\pi^+\pi^-$ channel. In (a) the invariant $m(\eta' K^+K^-)$ mass distribution is shown, in (b) the $m(K^+K^-)$ mass spectrum, in (c) the $m(\eta' K^\pm)$ mass spectrum and in (d) the $m(\gamma K^\pm)$ spectrum. The identification of the plotted lines follows the legends pictured. Below the mass distribution the residuals are pictured.

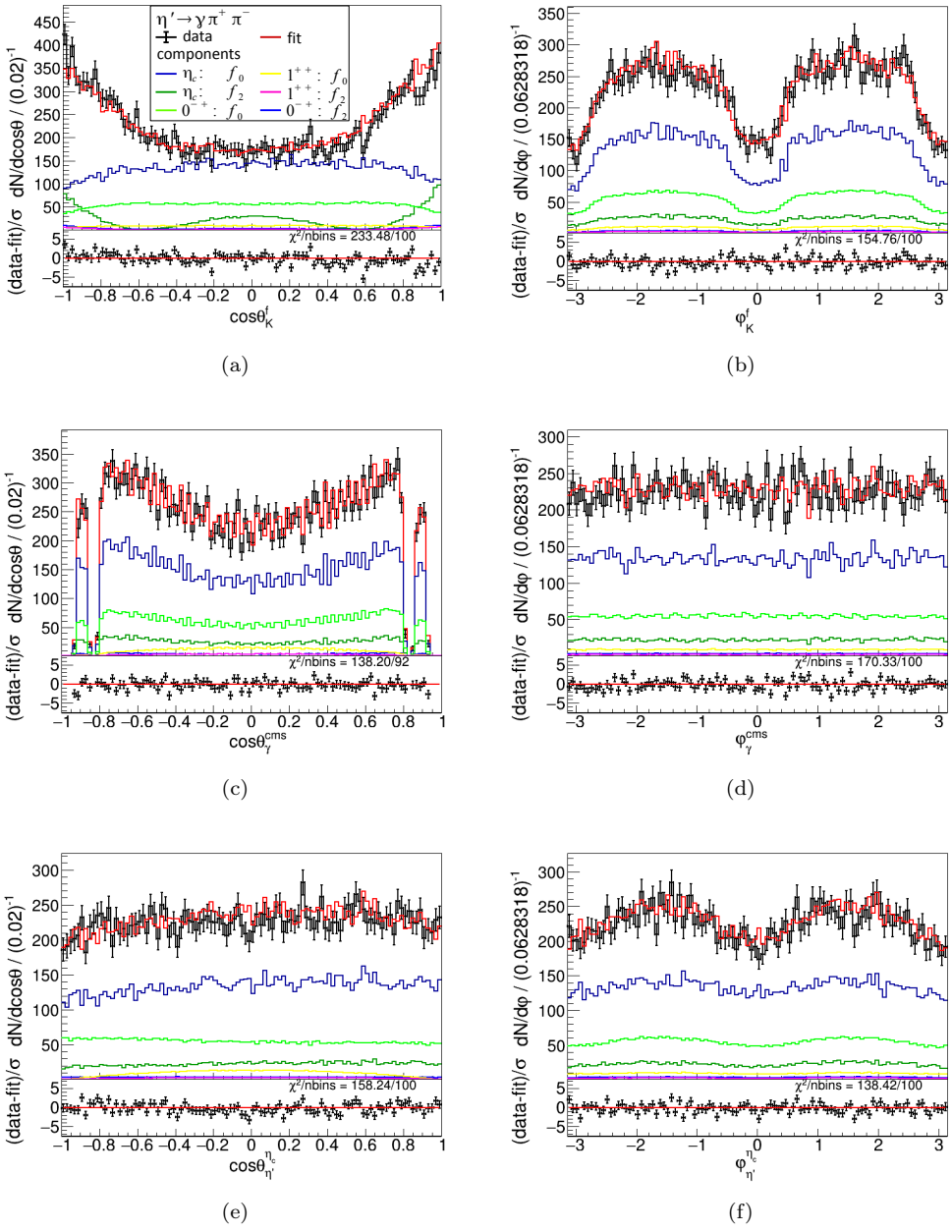

Figure 25: Decay helicity angular distributions for the "K-matrix PWA" with "minimal background" for the $\eta' \to \gamma\pi^+\pi^-$ channel. On the left the projections to the polar decay angle θ are shown, on the right to the azimuthal angle φ. In (a) and (b) the angular distributions of $K^\pm$ in the f rest frame are pictured, in (c) and (d) of η' in the η_c rest frame and in (e) and (f) of the radiative γ in the center of mass system (cms). The identification of the plotted lines follows the legend pictured in (a). Below the residuals are shown.

"K-Matrix PWA" with "Minimal Background" for the $\eta' \to \eta\pi^+\pi^-$ Channel

Projections to Invariant Masses

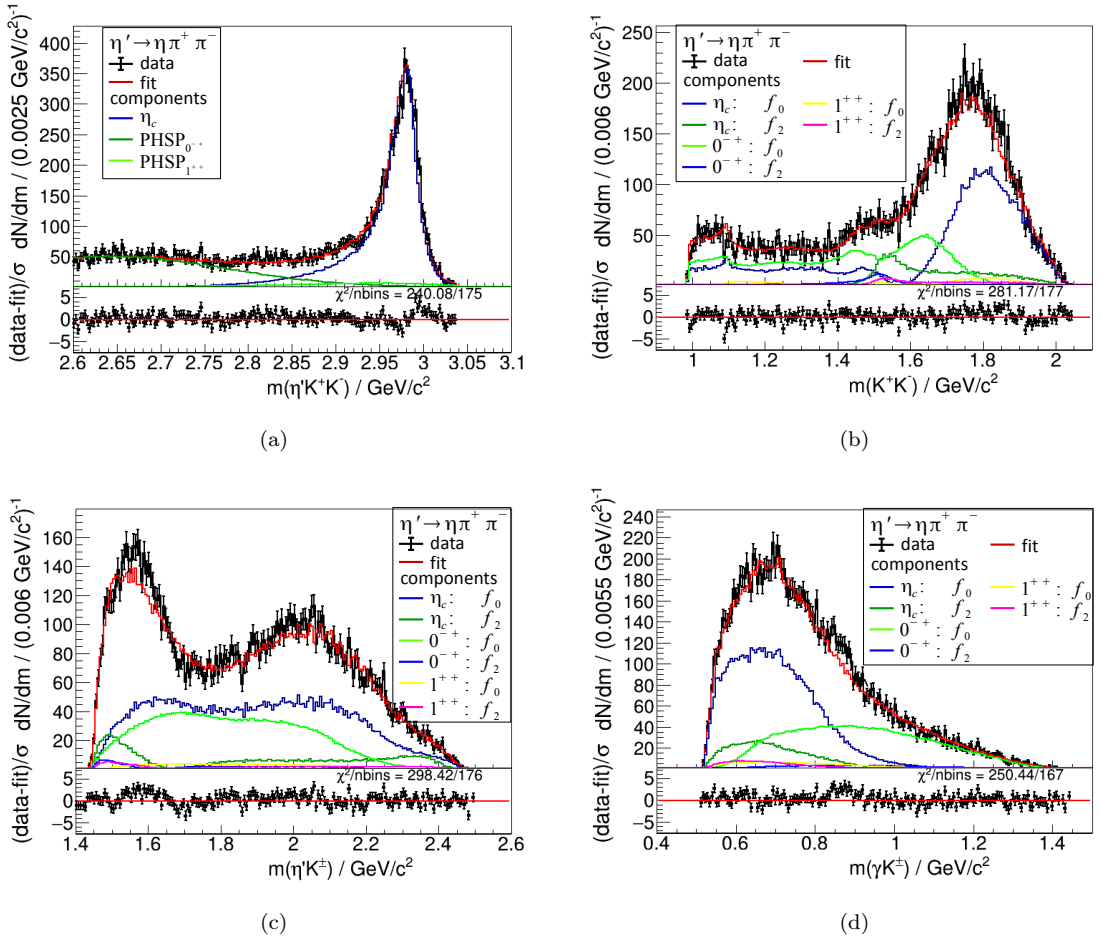

Figure 26: Projections of the PWA-fit results to different invariant masses for the "K-matrix PWA" with "minimal background" for the $\eta' \to \eta\pi^+\pi^-$ channel. In (a) the invariant $m(\eta' K^+ K^-)$ mass distribution is shown, in (b) the $m(K^+K^-)$ mass spectrum, in (c) the $m(\eta' K^\pm)$ mass spectrum and in (d) the $m(\gamma K^\pm)$ spectrum. The identification of the plotted lines follows the legends pictured.

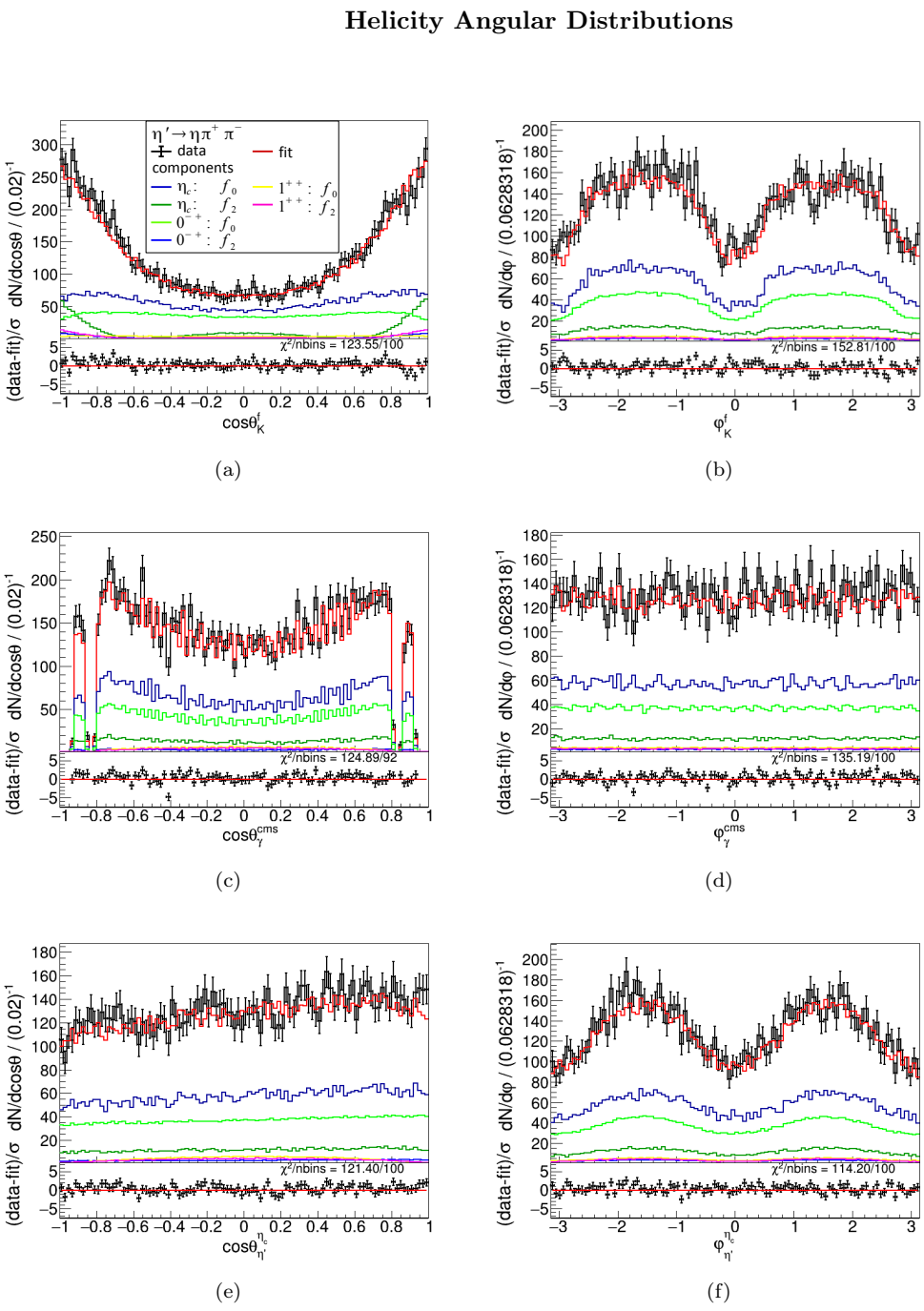

Figure 27: Decay helicity angular distributions for the "K-matrix PWA" with "minimal background" for the $\eta' \to \eta\pi^+\pi^-$ channel. On the left the projections to the polar decay angle θ are shown, on the right to the azimuthal angle φ. In (a) and (b) the angular distributions of $K^\pm$ in the f rest frame are pictured, in (c) and (d) of η' in the η_c rest frame and in (e) and (f) of the radiative γ in the center of mass system (cms). The identification of the plotted lines follows the legend pictured in (a). Below the residuals are shown.

"Breit-Wigner PWA" with "Minimal Background" for the $\eta' \to \eta\pi^+\pi^-$ Channel

Projections to Invariant Masses

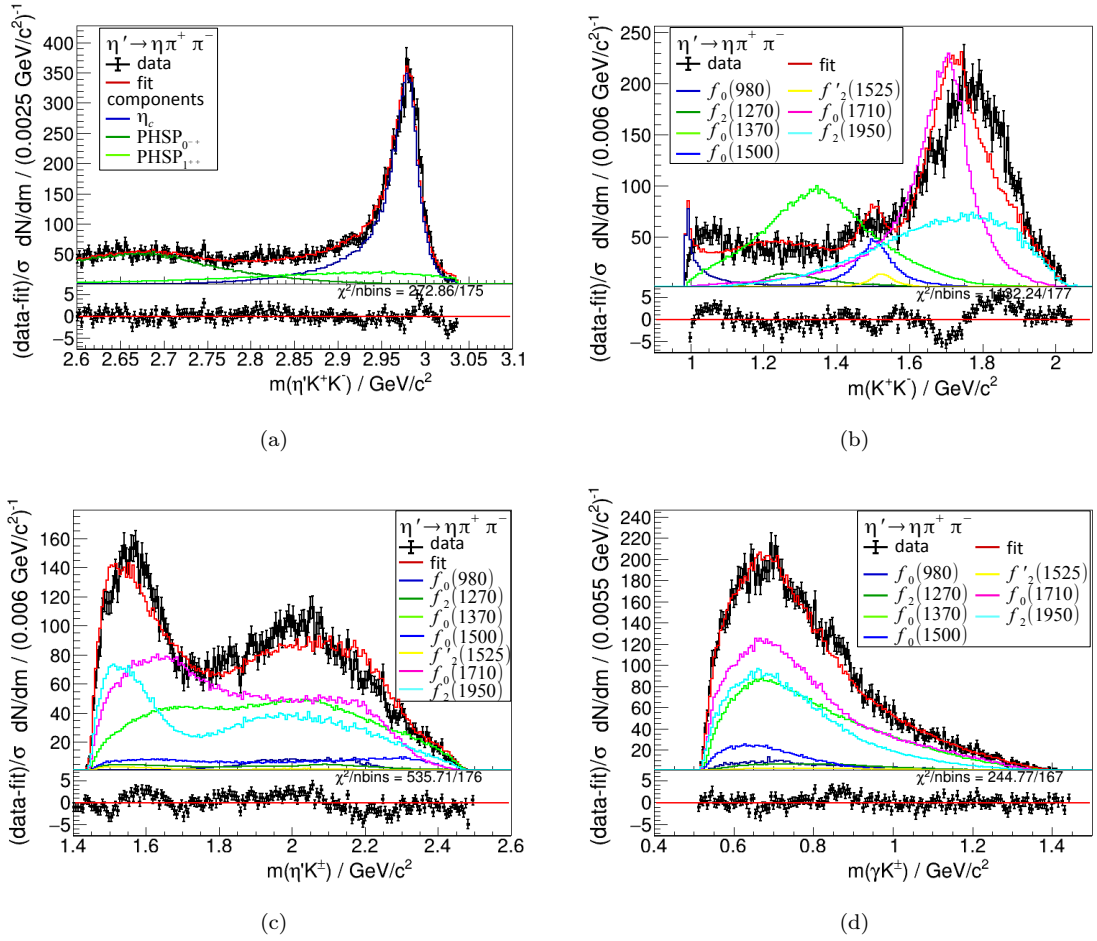

Figure 28: Projections of the PWA-fit results to different invariant masses for the "Breit-Wigner PWA" with "minimal background" for the $\eta' \to \eta\pi^+\pi^-$ channel. In (a) the invariant $m(\eta' K^+ K^-)$ mass distribution is shown, in (b) the $m(K^+K^-)$ mass spectrum, in (c) the $m(\eta' K^\pm)$ mass spectrum and in (d) the $m(\gamma K^\pm)$ spectrum. The identification of the plotted lines follows the legends pictured. Below the mass distribution the residuals are pictured.

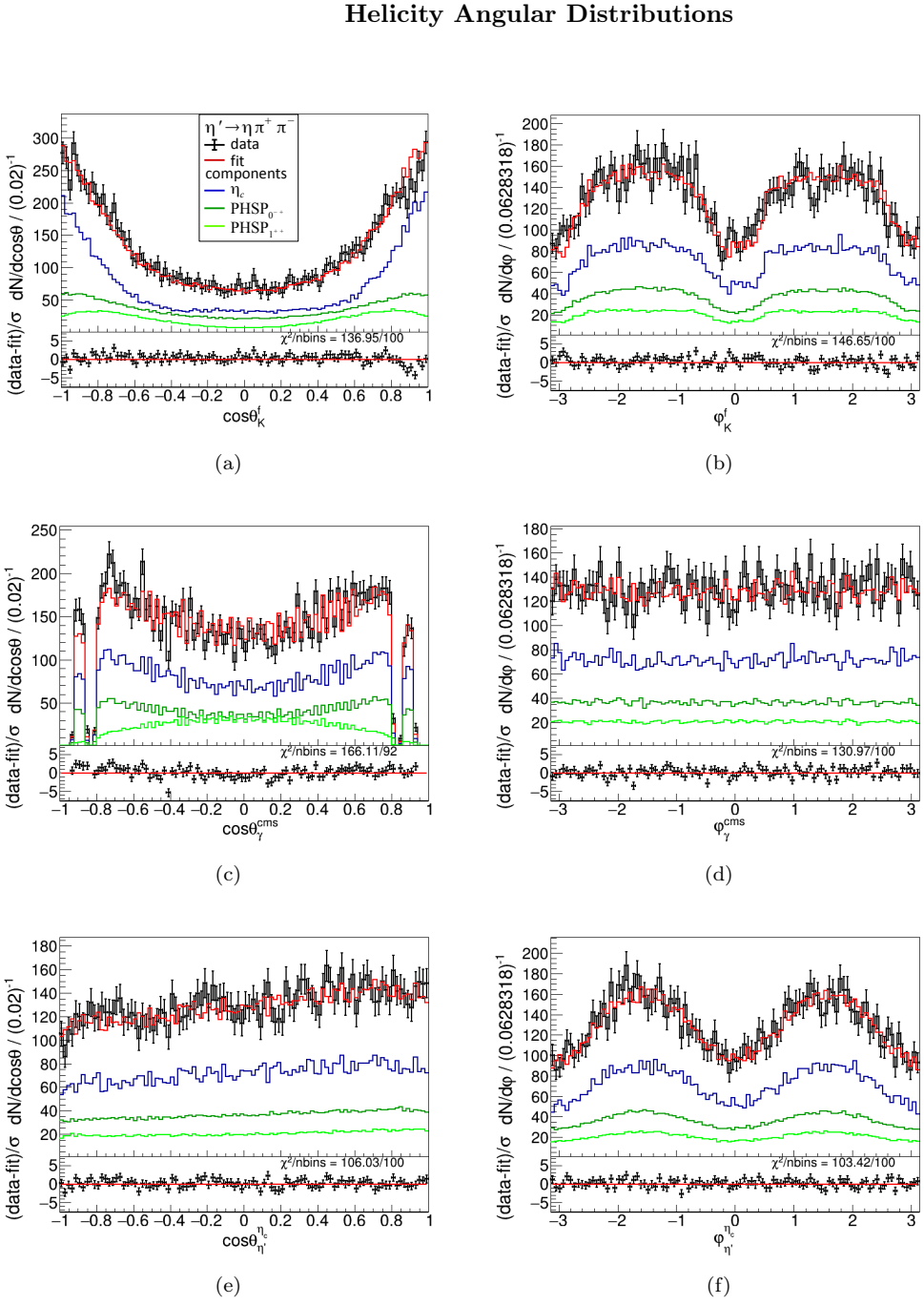

Figure 29: Decay helicity angular distributions for the "Breit-Wigner PWA" with "minimal background" for the $\eta' \to \eta\pi^+\pi^-$ channel. On the left the projections to the polar decay angle θ are shown, on the right to the azimuthal angle φ. In (a) and (b) the angular distributions of $K^\pm$ in the f rest frame are pictured, in (c) and (d) of η' in the η_c rest frame and in (e) and (f) of the radiative γ in the center of mass system (cms). The identification of the plotted lines follows the legend pictured in (a). Below the residuals are shown.

Comparison of the two PWA Approaches. In the following, the fit results of the two PWA approaches "K-Matrix PWA" and "Breit-Wigner PWA" are compared to each other.
With regard to the projections to the helicity decay angular distributions, the fit results of both PWA hypotheses describe the data quite well, as can be seen in Figure 27 for the "K-Matrix PWA" and in Figure 29 for the "Breit-Wigner PWA", exemplarily. Hence, the description of the angular distributions succeeds model independent, here.
However, the projections to the invariant masses show large deviations between the approaches. Whereas the "K-Matrix PWA" also provides fit results, that are in good agreement with data (see for instance Fig. 26), the "Breit-Wigner PWA" clearly fails (see for instance Fig. 28 (b) and (c)).

To compare the quality of the fit results quantitatively, the values for the final likelihoods $\mathcal{L}$ are used. They are summarised in Table 12, whereby the fit quality is the better the more negative the final likelihood is.

	Minimal Background	**Maximal Significance**
K-Matrix PWA		
Final Likelihood $(-\ln\mathcal{L})$	-32469	-41206
Number of free Parameters	65	65
Breit-Wigner PWA		
Final Likelihood $(-\ln\mathcal{L})$	-30147	-38395
Number of free Parameters	53	53

Table 12: Results for the final likelihoods $\mathcal{L}$ of the two PWA hypotheses "K-Matrix PWA" and "Breit-Wigner PWA" for the two FOM approaches "minimal background" and "maximal significance".

As can be seen in Table 12, the "K-Matrix PWA" provides clearly better fit results (with more than 35σ)[7] than the "Breit-Wigner PWA" in both cases, for the "minimal background" and "maximal significance" approach[8].

Thus, within this analysis, the "K-Matrix PWA" is identified as the best PWA hypothesis.

There are several reasons for the failure of the current "Breit-Wigner PWA". The seven incorporated f_J resonances have partially the same quantum numbers and overlap with regard to their widths as can be seen markedly in Figure 28 (b). Additionally, they are able to decay into several modes besides the K^+K^- channel, for example into the $\pi\pi$ or partially the $\eta\eta$ channel [12]. Thus, as already discussed in theory (sect. 2.4.4) the two-body unitarity is violated, since the "Breit-Wigner PWA" does not include interference effects between the resonances correctly. Furthermore, the "Breit-Wigner PWA" does not incorporate the very broad $f_0(500)$ resonance, as it cannot be described reasonably by a simple Breit-Wigner parameterisation [21]. In contrast, it is implemented in the utilized K-Matrix approach of the "K-Matrix PWA". However, this resonance has a large influence concerning the correct description of the $K\overline{K}$ threshold around 1 GeV/c^2 in Figure 28 (b), that clearly fails here.

[7] The significance between the fit results of the PWA approaches is determined via the probability for the given difference of the final likelihoods $\Delta(\ln\mathcal{L})$ and the difference between the total numbers of free fit parameters using the incomplete gamma function. Afterwards, the half of the calculated probability serves as the upper limit for the determination of the integral of the upper tail of the Gaussian distribution as the inverse of the cumulative distribution function, which provides the significance in terms of σ [61].

[8] As it will be discussed below in more detail, the final likelihood values are not appropriate for a quantitative comparison between the two FOM approaches, since the "'minimal background" and "maximal significance" approach are based on deviating data samples.

Moreover, the seven f_J resonances are all parameterised by Breit-Wigner amplitudes with fixed masses and widths. Thus, only the magnitude of the Breit-Wigner functions remains as a degree of freedom for the PWA fit. Furthermore, the values for the masses and widths are fixed to the average values estimated via the PDG. The averaging of these values is based on published experimental results and theoretical estimations, that show partially large deviations to each other [12]. For instance, for the $f_0(1370)$ resonance the mass is estimated by the PDG between 1200 and 1500 MeV and the width from 200 to 500 MeV [12]. Additionally, the Breit-Wigner parameter, which are fixed to the particles' mass and width, do not intrinsically correspond to the particles' properties in general, as they depend on the production reaction of the parameterised resonance.
Thus, the parameterisation via Breit-Wigner amplitudes with fixed values for the resonances' masses and widths most probably do not mirror the actual physics in data. The parameterisation with free but reasonably limited masses and widths would improve the fit results. A corresponding "Breit-Wigner PWA" with free masses and widths has already been carried out and a first elementary evaluation of the results has been performed. In Figure 30 first results are presented via the projections of the PWA fit to the invariant masses of $\eta' K^+K^-$ and K^+K^-. An elementary analysis shows a significant improvement of the fit results in comparison to the "Breit-Wigner PWA" with fixed masses and widths. However, the "K-Matrix PWA" further provides a still around 18σ better fit result than the improved "Breit-Wigner PWA" with free masses and widths.

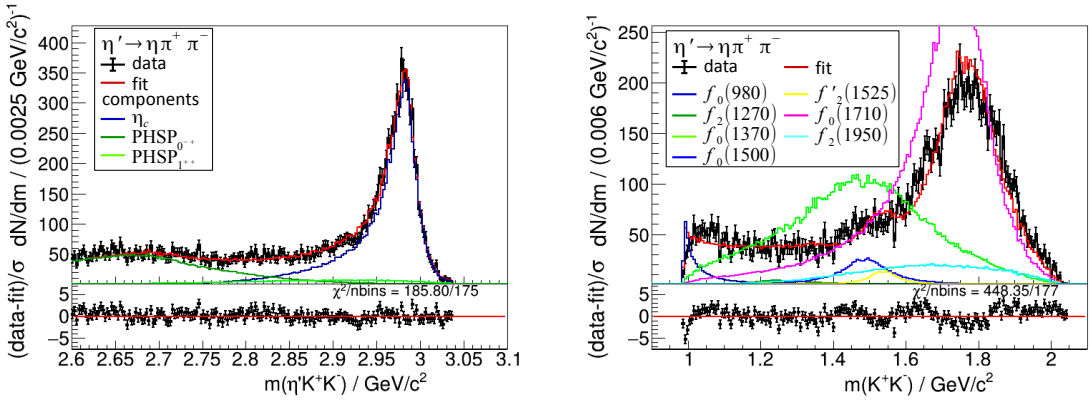

(a) (b)

Figure 30: Projections to the invariant $\eta' K^+K^-$ mass on the left and K^+K^- mass on the right of the "Breit-Wigner PWA" with free masses and widths using the "minimal background" approach for the $\eta' \to \eta\pi^+\pi^-$ channel. The identification of the plotted lines follows the legends pictured. Below the projections the residuals are pictured.

In contrast, the "K-Matrix PWA" describes data quite well in all projections, which also approves the seven f_J-resonance hypothesis to be in good agreement with data. However there is also still potential for improvement of the fit quality. Considering for example the projection of the "K-Matrix PWA" fit to the invariant $\eta' K^+K^-$ mass in Figure 44 (a) reveals, that primarily underneath the η_c signal larger deviations between data and the total fit occurs in this projection. Hence, in the following, possible approaches for improvement are discussed.
In Figure 31 the projections of the PWA fit results to the invariant mass $m(\gamma K^\pm)$ are shown for the "K-Matrix PWA" with "minimal background". On the left the $\eta' \to \gamma\pi^+\pi^-$ channel and on the right the $\eta' \to \eta\pi^+\pi^-$ channel are shown. In particular in the latter channel a small peak around 0.9 GeV/c^2 can be seen. This still unconsidered background component may result from charged,

excited kaons $K^*(892)^{\pm}$, that decay with the branching ratio of $(0.098 \pm 0.009)\%$ into $\gamma K^{\pm}$ [12]. By implementing this background reaction into the current PWA hypotheses, the PWA fit results may be improved.

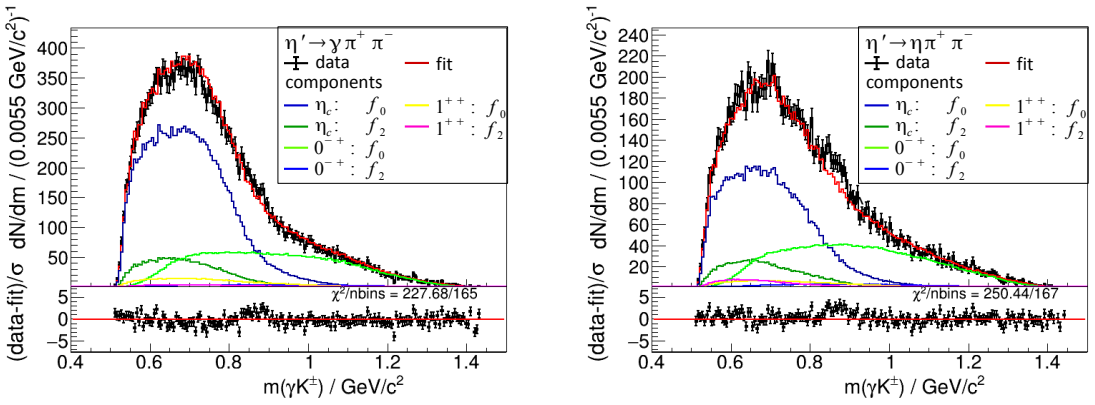

(a) (b)

Figure 31: Projections to the invariant $\gamma K^{\pm}$ mass of the "K-matrix PWA" with "minimal background" for the $\eta' \to \gamma\pi^+\pi^-$ channel in (a) and for the $\eta' \to \eta\pi^+\pi^-$ channel in (b). The identification of the plotted lines follows the legends pictured. Below the projections the residuals are shown.

Another approach for possible improvement is, to vary, exchange or extend the current seven f_J-resonance hypothesis both PWA approaches are based on. Ideas for possible further resonances in the reaction $\eta_c \to \eta' K^+ K^-$ can be found for instance in Figure 32, that shows the projections to the invariant mass $m(\eta' K^{\pm})$ for both final state channels of the "K-matrix PWA" with "minimal background". Here, a peak around 1.6 GeV/c^2 and a broad accumulation around 2.0 GeV/c^2 is observed and the residues reveal larger deviations between data and the PWA fit results in the mass region of $(1.4 - 1.7)$ GeV/c^2. A possible reason is, that further resonances of the $\eta_c \to \eta' K^+ K^-$ reaction occur that decay into the $\eta' K^{\pm}$ system. So far, only seven intermediate f_J resonances have been considered decaying solely into the K^+K^- system. To evaluate the assumption of further resonances additional studies via an appropriate PWA approach including also resonances decaying into the $\eta' K^{\pm}$ channel are required. Possible candidates are for example the excited kaons $K_0^*(1430)$, $K_2^*(1980)$ and $K_0^*(1950)$. The decay of the $K_0^*(1430)$ into $\eta' K^{\pm}$ has already been seen [12], likewise the decay of the $K_2^*(1980)$ into $\eta K^{\pm}$ [12], which suggests also the analogous decay into $\eta' K^{\pm}$ to be existing. Furthermore, both η_c decays into $K_0^*(1430)\overline{K}$ and $K_0^*(1950)\overline{K}$ are already listed in the PDG [12]. Finally, so far the "K-Matrix PWA" solely describes the f_0 resonances via a K-Matrix approach. The f_2 contributions are still parameterised with Breit-Wigner amplitudes. Thus, the description of the f_2 contributions by an additional K-Matrix approach, using the results published for instance in [60], is expected to further improve the "K-Matrix PWA" fit results.

Comparison of the two FOM Approaches. The comparison between the two FOM approaches "minimal background" and "maximal significance" is more complex, since the same PWA hypothesis is tested on data samples that correlate and deviate partially due to different event selection criteria applied. Thus, in this case no appropriate variable (like the final likelihood) is available in the scope of this work to quantitatively compare the PWA fit results between both approaches.
The data sample of the "maximal significance" approach contains a higher number of events that

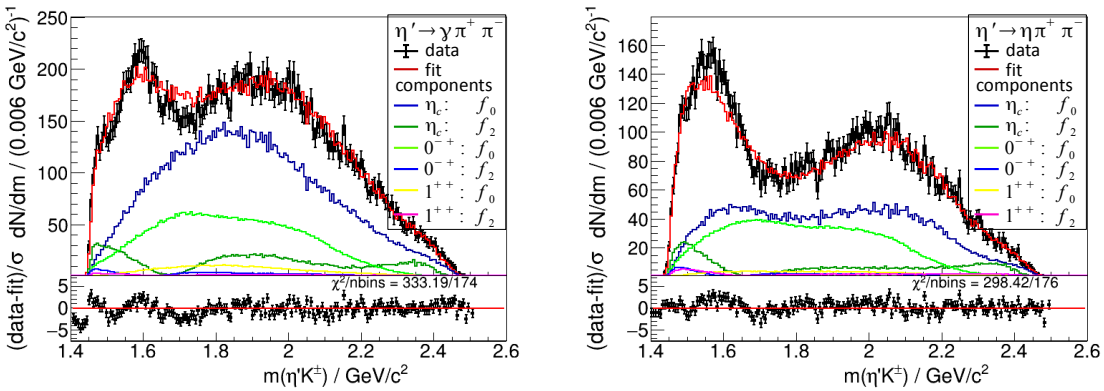

(a) (b)

Figure 32: Projections to the invariant $\eta' K^{\pm}$ mass of the "K-matrix PWA" with "minimal background" for the $\eta' \to \gamma\pi^+\pi^-$ channel in (a) and for the $\eta' \to \eta\pi^+\pi^-$ channel in (b). The identification of the plotted lines follows the legends pictured. Below the projections the residuals are shown.

is in general beneficial for performing PWA. However, this data sample also incorporates a higher background level, which is vice versa more challenging for a PWA. However, comparing the projections to the different invariant masses and helicity angular distributions between both FOM approaches, one finds the following. The "minimal background" approach provides slightly better single PWA fit results with slightly lower χ^2 values in each projection than the "maximal significance approach". This aspect supports the expectation, that a background level as low as possible improves the PWA fit results, rather than a significance as high as possible. The reason is, that remaining background has to be included correctly into a PWA hypothesis for an optimal fit result and this comes to be more challenging, the higher the background level is.
However, the argumentation via the χ^2 values of the single projections has to be considered with special care. The PWA fit represents an unbinned fit in all dimensions and thus, the χ^2 value only evaluates the fit result with respect to this single projection. It is not optimised or minimised to the total fit result. Nevertheless, the determination of a global reduced χ^2 value, that describes the overall goodness of the PWA fit via the comparison of all relevant data histograms and fit projections, as it is done for instance in [62], might provide a variable for a quantitative comparison between the two approaches.

In conclusion, based on the expectation, that a background as low as possible improves the PWA fit quality more than a high significance of signal sitting on a higher background level, the "K-Matrix PWA" using the "minimal background" approach is identified in this analysis as the best PWA hypothesis. Its results will be used for further studies, starting with the determination of the branching ratio $BR_{\eta_c \to \eta' K^+ K^-}$ in the following section. However, the results of the other performed PWAs will also be mentioned, as they serve in the following as first systematic studies.

4.3.3 The η_c Branching Ratio

The branching ratio of the reaction $\eta_c \to \eta' K^+ K^-$ is given by

$$BR_{\eta_c \to \eta' K^+ K^-} = \frac{N_{\eta_c \to \eta' K^+ K^-}}{N_{\eta_c}}, \tag{48}$$

where N_{η_c} is the number of η_c mesons produced in radiative J/ψ decays at BESIII and $N_{\eta_c \to \eta' K^+ K^-}$ is the number of η_c mesons that have decayed to $\eta' K^+ K^-$ in the detector.
From 2009 to 2019, a total of $N_{J/\psi} = (10.087 \pm 0.044) \cdot 10^9$ J/ψ mesons were produced via e^+e^- collisions at BESIII [51], so that

$$N_{\eta_c} = N_{J/\psi} \cdot BR_{J/\psi \to \gamma \eta_c} = (171.5 \pm 40.4) \cdot 10^6 \tag{49}$$

with $BR_{J/\psi \to \gamma \eta_c} = (1.7 \pm 0.4)\%$ being the branching fraction of the J/ψ decay to $\gamma \eta_c$ [12].
The number $N_{\eta_c \to \eta' K^+ K^-}$ is unknown, due to imperfect detection capabilities. However, via the number $N_{\mathrm{obs},\eta_c \to \eta' K^+ K^-}$ of observed η_c particles and the detector efficiency ϵ it is given

$$N^i_{\eta_c \to \eta' K^+ K^-} = \frac{N^i_{\mathrm{obs},\eta_c \to \eta' K^+ K^-}}{\epsilon_i \cdot BR_{\mathrm{i}}} \begin{cases} \text{with} \;\; BR_i = BR_{\eta' \to \gamma \pi^+ \pi^-} & \text{for} \quad \eta' \to \gamma \pi^+ \pi^- \\ \text{with} \;\; BR_i = BR_{\eta' \to \eta \pi^+ \pi^-} \cdot BR_{\eta \to \gamma\gamma} & \text{for} \quad \eta' \to \eta \pi^+ \pi^- \end{cases} \tag{50}$$

with BR_{i} being the branching ratio of the considered decay the η' is reconstructed in.

In conclusion, inserting the equations (50) and (52) in (48) the branching ratio for the η_c decay to $\eta' K^+ K^-$ can be written as

$$\begin{aligned} BR_{\eta_c \to \eta' K^+ K^-} = \; & \frac{N^i_{\mathrm{obs},\eta_c \to \eta' K^+ K^-}}{N_{J/\psi} \cdot BR_{J/\psi \to \gamma \eta_c} \cdot \epsilon_i \cdot BR_{\mathrm{i}}} \\ & \text{with} \begin{cases} BR_i = BR_{\eta' \to \gamma \pi^+ \pi^-} & \text{for} \quad \eta' \to \gamma \pi^+ \pi^- \\ BR_i = BR_{\eta' \to \eta \pi^+ \pi^-} \cdot BR_{\eta \to \gamma\gamma} & \text{for} \quad \eta' \to \eta \pi^+ \pi^-. \end{cases} \end{aligned} \tag{51}$$

In this equation the detector efficiency ϵ_i and the number of observed η_c particles $N^i_{\mathrm{obs},\eta_c \to \eta' K^+ K^-}$ are still unknown. Both quantities will be determined in the following via the PWA results, starting with the detector efficiency.

Determination of the Detector Efficiency. The detector efficiency ϵ is given by

$$\epsilon = \frac{\sum_{i=1}^{n_{\eta_c,\mathrm{acc}}} w_i}{\sum_{i=1}^{n_{\eta_c,\mathrm{gen}}} w_i} \tag{52}$$

with $n_{\eta_c,\mathrm{gen}}$ and $n_{\eta_c,\mathrm{acc}}$ being the numbers of generated and accepted MC events, whereby each event is assigned an event weight w_i appropriate to the PWA solution. Thus, the detector efficiency is determined as the ratio between the sum over the weights of the accepted MC events divided by the sum over the weights of the generated MC events. Both numbers are estimated by integrating the invariant $m(\eta' K^+ K^-)$ mass spectra of the weighted accepted and generated MC simulation within the interval of $(2.6 - 3.1)$ GeV/c^2, respectively. The chosen interval incorporates almost the entire η_c signal contribution. The same integrating procedure will be applied for the determination of the number of observed η_c particles, presented below.
The resulting detector efficiencies are summarised in Table 13, whereby the result for the best PWA hypothesis of this analysis ("K-Matrix PWA" with "minimal background") is shaded in grey. The presented uncertainties are solely statistical.

Determination of the Number of observed η_c Particles. In Figure 33 the projections of the fit results to the invariant mass $m(\eta' K^+ K^-)$ are presented for the "K-Matrix PWA" for both final

state channels using the "minimal background" approach. The total fits are separated into the η_c signal and the two non-resonant background contributions $\text{PHSP}_{0^{-+}}$ and $\text{PHSP}_{1^{++}}$. Integrating over the η_c signal part of the PWA solution (blue line) within the interval of $(2.6 - 3.1)$ GeV/c^2 provides the number $N_{\text{obs},\eta_c \to \eta' K^+ K^-}$ of observed η_c mesons decaying to $\eta' K^+ K^-$. However, the resulting uncertainty solely incorporates the uncertainty coming from the PWA fit. Thus, the uncertainty of data, determined via a similar integration over data, has to be included via Gaussian error propagation. The results are listed in Table 13. It also lists the detector efficiencies and the resulting η_c branching ratios according to equation (51). The uncertainties in brackets exclude the large uncertainty of the $J/\psi \to \gamma\eta_c$ branching ratio. The results for the best PWA hypothesis are shaded in grey.

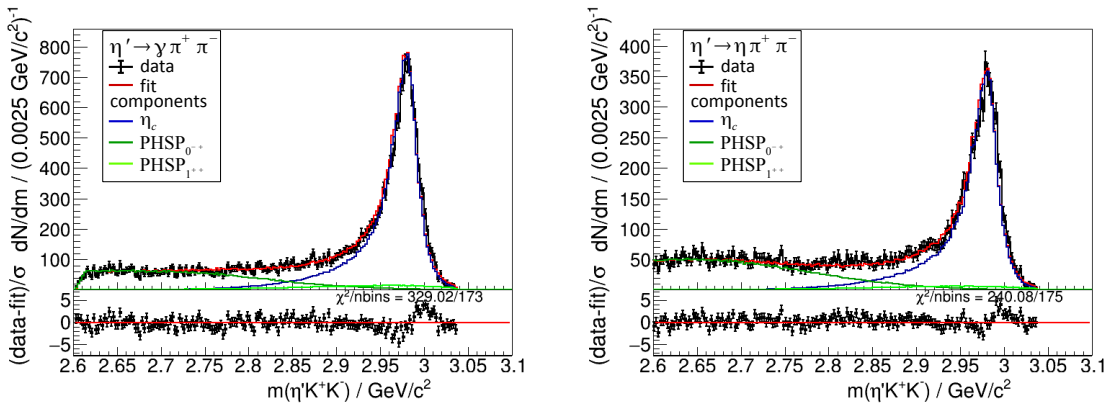

(a) (b)

Figure 33: Projections to the invariant mass $m(\eta' K^+ K^-)$ for the "K-matrix PWA" for the "minimal background" approach. On the left, the $\eta' \to \gamma\pi^+\pi^-$ channel is plotted, on the right, the $\eta' \to \eta\pi^+\pi^-$ channel. Data points are plotted in black, the total fit in red and the contributions of the η_c signal component and the two non-resonant components $\text{PHSP}_{0^{-+}}$ and $\text{PHSP}_{1^{++}}$ are pictured as given in the legends.

Discussion of the η_c Branching Ratio. The η_c branching ratio depends on the branching ratio of the J/ψ decay to $\gamma\eta_c$ (see eq. (51)), that is given by $BR_{J/\psi \to \gamma\eta_c} = (1.7 \pm 0.4)\%$ [12]. It has a very large uncertainty of almost 25%. This leads to the large uncertainties of the calculated η_c branching ratios presented in Table 13 without brackets. Neglecting the J/ψ uncertainty gives the values in brackets, that are one order of magnitude smaller. Hence, once the uncertainty of the $J/\psi \to \gamma\eta_c$ decay is determined more precisely, the calculated uncertainty for the $\eta_c \to \eta' K^+ K^-$ branching ratio in this work will be directly improved up to one order of magnitude.

In the following, the obtained branching ratios for the best PWA hypothesis in this work (shaded in grey in Tab. 13) are discussed. For the $\eta' \to \gamma\pi^+\pi^+$ channel a value of $BR_{\eta_c \to \eta' K^+ K^-} = (1.91 \pm 0.45\ (0.04))\%$ and for the $\eta' \to \eta\pi^+\pi^+$ channel the value $(1.65 \pm 0.39\ (0.03))\%$ have been determined.
The uncertainties of the two branching ratios are statistically correlated. However, to compare both results with each other, the uncorrelated uncertainties have to be known. These are upwards estimated via the stated uncertainties in brackets, which are the ones excluding the $J/\psi \to \gamma\eta_c$ branching ratio. Thus, considering the adjusted uncertainties in brackets, it can be concluded, that

	Maximal Significance		Minimal Background	
	$\eta' \to \gamma\pi^+\pi^-$	$\eta' \to \eta\pi^+\pi^-$	$\eta' \to \gamma\pi^+\pi^-$	$\eta' \to \eta\pi^+\pi^-$
K-Matrix PWA				
$n_{\mathrm{obs},\eta_c\to\eta' K^+K^-}$	29122.2 ± 219.5	16612.4 ± 143.6	22940.0 ± 185.1	12624.0 ± 124.7
ϵ / %	3.24 ± 0.01	3.51 ± 0.01	2.42 ± 0.01	2.65 ± 0.01
$BR_{\eta_c\to\eta' K^+K^-}$ / %	1.82 ± 0.43 (0.04)	1.65 ± 0.39 (0.03)	1.91 ± 0.45 (0.04)	1.65 ± 0.39 (0.03)
Breit-Wigner PWA				
$N_{\mathrm{obs},\eta_c\to\eta' K^+K^-}$	28862.8 ± 218.2	16875.4 ± 143.8	22726.2 ± 184.4	12840.7 ± 125.1
ϵ / %	3.25 ± 0.01	3.61 ± 0.01	2.41 ± 0.01	2.72 ± 0.01
$BR_{\eta_c\to\eta' K^+K^-}$ / %	1.79 ± 0.42 (0.04)	1.62 ± 0.38 (0.03)	1.90 ± 0.45 (0.04)	1.64 ± 0.39 (0.03)

Table 13: Number $N_{\mathrm{obs},\eta_c\to\eta' K^+K^-}$ of observed η_c mesons decaying to $\eta' K^+K^-$, detector efficiencies ϵ and the resulting branching ratios $BR_{\eta_c\to\eta' K^+K^-}$ determined via the results of the two PWA approaches "K-Matrix PWA" and "Breit-Wigner PWA", which are separated into the results for the two FOM approaches "minimal background" and "maximal significance" and the two considered final state channels $\eta' \to \gamma\pi^+\pi^-$ and $\eta' \to \eta\pi^+\pi^-$. The uncertainties in brackets neglect the uncertainty of the $J/\psi \to \gamma\eta_c$ branching ratio.

the branching ratios for the two final state channels are statistically incompatible. They deviate against the expectation with more than 6σ, which might result from systematic uncertainties, that have not been considered, yet. Taking the results of the other PWA and FOM approaches into account (see Tab. 13), which have to be understood as first systematic study results, the $\eta' \to \gamma\pi^+\pi^+$ channel shows in particular significant deviations. The branching ratios differ against the expectation significantly between the FOM approaches and also slightly between the two PWA approaches. However, the branching ratio results for the $\eta' \to \eta\pi^+\pi^-$ channel coincide quite well between the two PWA and FOM approaches and hence are almost model independent here, as expected.
The deviations between the channels may be caused by systematic uncertainties due to the different event selection criteria applied. Hence, possible deviations between the MC simulation and data, which could be larger for the $\eta' \to \gamma\pi^+\pi^-$ channel, occur and could cause the systematic differences. Furthermore, in the $\eta' \to \gamma\pi^+\pi^-$ channel, the pion pair is simulated through a decaying ρ_0 (see sect. 37). Here, via the utilized BesEvtGen generator a phase space model has been adopted. To improve the quality of the MC simulation in this channel a description including ρ/ω interference and incorporation of the box anomaly should be used [63].

In conclusion, whereas the $\eta' \to \eta\pi^+\pi^-$ channel provides promising results for the branching ratio $BR_{\eta_c\to\eta' K^+K^-}$ in the scope of this work, the channel $\eta' \to \gamma\pi^+\pi^-$ has to be further analysed. Furthermore, a complete systematic study is required to extend the determined uncertainty for the branching ratios by the systematic error.
In summary, as a result of this analysis the weighted arithmetic mean of the branching ratios of the two final state channels of the best PWA hypothesis is taken to state:

The branching ratio of the decay $\eta_c \to \eta' K^+K^-$ is experimentally obtained to be $BR^{mean}_{\eta_c\to\eta' K^+K^-} = (1.76 \pm 0.29)\,\%$ using the 10 billion J/ψ data sample of BESIII.

Comparison with the Theoretical Prediction. The $\eta_c \to \eta' K\overline{K}$ branching ratio is predicted to be $(1.34 \pm 0.13)\%$ (see sect. 2.3 and [11]). It includes the η_c decays into η' and the neutral

kaon combinations K^+K^- and $K^0\overline{K}^0$ (and hence, also K_SK_S and K_LK_L). However, the studied $\eta_c \to \eta' K^+K^-$ decay considers solely the K^+K^- kaon combination, which provides a twice as large contribution as the K_SK_S and K_LK_L pairs. Therefore, the branching ratio for the η_c decay to $\eta' K^+K^-$ is predicted to be $BR^{\text{theo}}_{\eta_c \to \eta' K^+K^-} \approx 0.67\%$.
Comparing the prediction with the result $BR^{\text{mean}}_{\eta_c \to \eta' K^+K^-} = (1.76 \pm 0.29)\%$ of this analysis an 4σ higher value is experimentally obtained. However, the theoretical prediction has to be understood solely as an order of magnitude prediction. With respect to this magnitude prediction, the experimental result lies in the same order as the prediction.

4.3.4 Investigation of Intermediate States decaying into K^+K^-

The PWA approach in this work is further used to study different intermediate resonances of the isoscalar scalar and tensor sector decaying into the K^+K^- system, whereby in particular the seven resonances $f_0(980)$, $f_0(1370)$, $f_0(1500)$, $f_0(1710)$, $f_2(1270)$, $f_2'(1525)$ and $f_2(1950)$ are considered.
In Figure 34 the projections to the invariant K^+K^- mass for the "K-matrix PWA" with "minimal background" are presented for both final state channels.

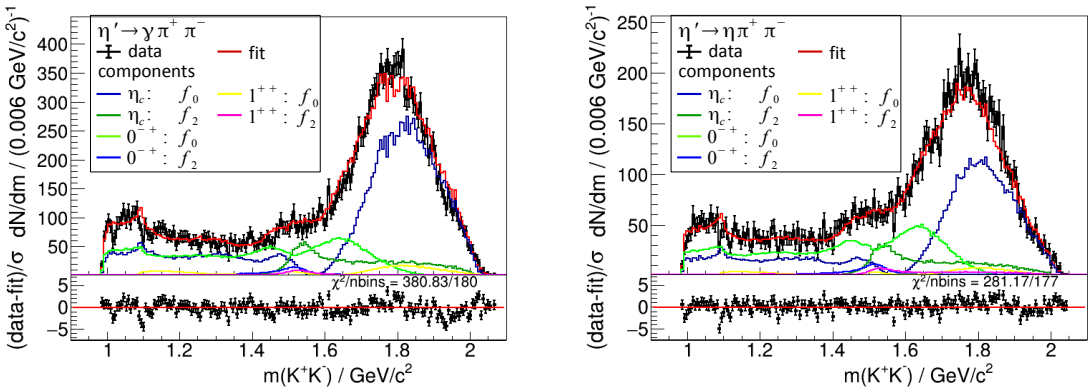

(a) (b)

Figure 34: Projections to the invariant mass $m(K^+K^-)$ for the "K-matrix PWA" for the "minimal background" approach. On the left, the $\eta' \to \gamma\pi^+\pi^-$ channel is presented, on the right, the $\eta' \to \eta\pi^+\pi^-$ channel. Data points are shown in black, the total PWA fit in red. The f_0 and f_2 components of the η_c signal contribution and of the two phase space components $\text{PHSP}_{0^{-+}}$ and $\text{PHSP}_{1^{++}}$ are identified following the legends pictured. Below the projections the residuals are pictured.

It can be seen that the total PWA fit works quite well in this projection. The residues reveal, that solely around 1.1 GeV/c^2 and 1.8 GeV/c^2 some larger deviations between data and the PWA fit occur. Considering the individual components of the fit, one finds, that the f_0 component of the η_c signal (dark blue line) dominates in both final state channels. Furthermore, this f_0 contribution shows a large broad accumulation around 1.8 GeV/c^2, where the $f_0(1710)$ is located. A further smaller and narrower peak is found on the left to 1.5 GeV/c^2, which corresponds to the $f_0(1500)$. An additional broader slight accumulation around 1.3 GeV/c^2 is observed, which is of the same intensity as the peak around 1.5 GeV/c^2 and may correspond partially to the $f_0(1370)$. However the coupling of the $f_0(1370)$ resonance into the $K\overline{K}$ system is predicted to be small [64]. Furthermore, the total PWA-fit overestimates data slightly around 1.3 GeV/c^2, as can be seen on the left in Figure

34. Hence, the identification of the $f_0(1370)$ is not significant.
The f_2 components of the η_c signal (dark green line) show in particular around 1.55 GeV/c^2 a peak, where the $f_2'(1525)$ is located, that smooths slowly out towards higher masses up to 2 GeV/c^2. This indicates a possible contribution of the $f_2(1950)$ resonance. Below 1.4 GeV/c^2, no contributions of the f_2 components are observed. Thus, the implemented $f_2(1270)$ resonance should play a vanishing role and may be neglected in further PWA hypotheses in the future.

Comparison with Theoretical Predictions. In the following the qualitative results of the experimentally observed f_0 resonances will be compared to the theoretical predictions presented in section 2.3 and [11]. The comparison is based on Table 5 of section 2.3, which lists the predictions for the branching ratios of $\eta_c \to \eta' f_0$ decays for the three resonances $f_0(1370)$, $f_0(1500)$ and $f_0(1700)$. For a better comparability the Table is reprinted here.

Decay channel	U_1 ([30])	U_2 ([29])	U_3 ([31])	U_4 ([31])	U_5 ([31])
$BR_{\eta_c \to f_0(1370)\eta'}$ / %	$6.25 \cdot 10^{-1}$	$6.25 \cdot 10^{-1}$	$6.25 \cdot 10^{-1}$	$6.25 \cdot 10^{-1}$	1.25
$BR_{\eta_c \to f_0(1500)\eta'}$ / %	$3.13 \cdot 10^{-1}$	$3.13 \cdot 10^{-2}$	$3.13 \cdot 10^{-5}$	$1.56 \cdot 10^{-1}$	$9.38 \cdot 10^{-2}$
$BR_{\eta_c \to f_0(1710)\eta'}$ / %	$1.25 \cdot 10^{-2}$	$1.25 \cdot 10^{-1}$	$1.56 \cdot 10^{-1}$	$1.88 \cdot 10^{-2}$	$2.81 \cdot 10^{-1}$

Table 14: Theoretical predictions for the branching ratios of the η_c decays to $\eta' f_0$ for the three resonances $f_0(1370)$, $f_0(1500)$ and $f_0(1710)$ using different mixing matrices U_n. [11]

The predicted results of the mixing matrix U_3 and U_5 do not coincide with the experimental results, since U_3 and U_5 predict up to four order of magnitude deviations between the contributions of the three resonances. Data shows contributions more likely in the same order of magnitude for the $f_0(1710)$ and $f_0(1500)$ and a possible only small contribution of $f_0(1370)$ (which disagrees with U_5). The mixing matrices U_1 and U_4 are also rejected. Both predict, that the contribution of the $f_0(1710)$ resonance is of minor role with even a contribution of one order of magnitude lower compared to the other two resonances. The experimental data show the opposite.
Only the predictions of the mixing matrix U_2 coincide with the experimental results to some extent. The contribution of the resonance $f_0(1500)$ is predicted to be one order of magnitude smaller. In data its contribution is also significantly smaller compared to the $f_0(1710)$ component.
Hence, a basically similar result can be seen between data and at most the U_2 mixing matrix.
If assuming the mixing matrix U_2 to be in agreement with data, the experimental data would support the prediction, that the $f_0(1500)$ resonance is mainly the isoscalar scalar glueball (see eq. (2) and (3)).
However, this comparison between data and the theoretical predictions has to be understood with special care. The analysed PWA-fit concerning possible f_0 contributions in the projection to the K^+K^- mass results of a K-Matrix approach. Thus, the single f_0 components cannot be explicitly extracted and plotted. Furthermore, in the invariant K^+K^- mass spectrum the product of two couplings is observed, the coupling of the η_c to $\eta' f_J$ and of f_J to K^+K^-. All relevant couplings here are experimentally still unknown (despite the branching ratio for $f_0(1500) \to K\overline{K}$ [12]). Thus, the relative heights of the observed peaks in the K^+K^- mass spectrum cannot be interpreted solely concerning the coupling of η_c to $\eta' f_J$.
Hence, no clear statement can be given at this point concerning the comparison between data and theoretical prediction. However, by considering further η_c decay channels, like for example $\eta_c \to \eta'\pi\pi$ or $\eta_c \to \eta'\eta\eta$ the aspect of the two-coupling dependence might be cleared up.

5 Conclusion and Outlook

Based on the world's largest 10 billion J/ψ data sample of the BESIII experiment the η_c decay to $\eta' K^+K^-$ has been studied in this analysis via a partial wave analysis in order to determine the so far unlisted η_c branching ratio to $\eta' K^+K^-$ and to investigate intermediate states decaying to K^+K^-. Here, in particular contributions of the isoscalar scalar resonances $f_0(1370)$, $f_0(1500)$ and $f_0(1710)$ were of special interest, since they might include admixtures of the lightest isoscalar scalar glueball. This analysis has been further motivated, as all results of this work are directly comparable with theoretical predictions made in [11].

Via specific and effective event selection criteria the searched η_c decay mode has been filtered out based on the two main η' decay channels $\eta' \to \gamma\pi^+\pi^-$ and $\eta' \to \eta\pi^+\pi^-$. Different approaches for the estimation of figure of merits have been tested: a method that maximises the significance and a second method that minimises background, since a background level as low as possible is expected to be more beneficial for performing PWAs.

The evaluation of the event selection criteria via selected invariant mass spectra revealed a clear and significant coincidence between the η_c and η' signal. Thus, the η_c decay to $\eta' K^+K^-$ has successfully been observed for the first time at the BESIII experiment. During finishing this thesis the BaBar Collaboration also found this so far unknown η_c decay mode in two-photon interactions [18]. However, their observation is based on a significant lower signal yield.

To determine the corresponding η_c branching ratio and to investigate intermediate states decaying to K^+K^- a partial wave analysis has been carried out via two hypotheses. Both approaches incorporated the four isoscalar scalar resonances $f_0(980)$, $f_0(1370)$, $f_0(1500)$ and $f_0(1710)$ as well as the three tensor mesons $f_2(1270)$, $f_2'(1525)$ and $f_2(1950)$ as candidates decaying into the K^+K^- system. Within the first approach the dynamical part of all f_J resonances has been parameterised with Breit-Wigner amplitudes with fixed masses and widths, whereas for the second approach a K-Matrix has been implemented to describe the f_0 contributions.

The PWA based on the K-Matrix and minimal background approach was identified as the best hypothesis in this work. Its results have been used to calculate the η_c branching ratio, which is $BR^{\text{mean}}_{\eta_c \to \eta' K^+K^-} = (1.76 \pm 0.29)\%$. It corresponds to the weighted arithmetic mean of the channel dependent results $BR_{\eta_c \to \eta' K^+K^-} = (1.91 \pm 0.45)\%$ (for $\eta' \to \gamma\pi^+\pi^-$) and $BR_{\eta_c \to \eta' K^+K^-} = (1.65 \pm 0.39)\%$ (for $\eta' \to \eta\pi^+\pi^-$). Thus, the branching ratios of the two channels showed deviations of more than 6σ against the expectation. Evaluating the results of the further performed PWAs as first systematic studies, in particular the $\eta' \to \gamma\pi^+\pi^-$ channel is identified to require further analysis and possibly an improvement of the quality of the underlying MC simulation.
The comparison of the experimentally obtained mean η_c branching ratio with the theoretical prediction of $BR^{\text{theo}}_{\eta_c \to \eta' K^+K^-} \approx 0.67\%$ showed a good agreement on magnitude order, as the theoretical value has to be understood solely as an order of magnitude prediction [11]. The BaBar Collaboration obtained the result $BR^{\text{BaBar}}_{\eta_c \to \eta' K^+K^-} / BR^{\text{PDG}}_{\eta_c \to \eta' \pi^+\pi^-} = 0.644 \pm 0.039_{\text{stat}} \pm 0.032_{\text{sys}}$ [18] relative to the known branching ratio $BR^{\text{PDG}}_{\eta_c \to \eta' \pi^+\pi^-} = (4.1 \pm 1.7)\%$ [12] of the decay $\eta_c \to \eta'\pi^+\pi^-$. The corresponding result of this work relative to the η' branching ratio is given by $BR^{\text{mean}}_{\eta_c \to \eta' K^+K^-} / BR^{\text{PDG}}_{\eta_c \to \eta' \pi^+\pi^-} = 0.43 \pm 0.19$, which shows a deviation of 2σ to the BaBar result.
However, the estimated η_c branching ratio of this work is based on PWA solutions that still show potential for improvement. For example, by optimising the parameterisation of the resonances' dynamical parts, by testing further PWA hypotheses via removing, exchanging or adding contributions (like heavy kaon resonances K^* decaying into the $\eta' K^\pm$ systems), or by taking so far unconsidered

background reactions into account (like the $K^*(892) \to \gamma K^{\pm}$ reaction), the PWA fit results will be further optimised, which directly affects the determination of the η_c branching ratio. Besides these PWA optimisations also a full systematic study is necessary in order to determine the systematic uncertainty of the calculated η_c branching ratio.

The PWA fit results of the current best hypothesis of this work have been additionally evaluated concerning the $f_0(1370)$, $f_0(1500)$ and $f_0(1710)$ contributions to the invariant K^+K^- mass spectrum. Whereas a possibly larger contribution of the $f_0(1710)$ resonance beside a lower fraction of the $f_0(1500)$ state has been found, the $f_0(1370)$ has not been clearly observed. The comparison with theoretical predictions revealed to some extent a coincidence to a mixing matrix, that identifies the $f_0(1500)$ resonance to be most likely the lightest glueball. However, the analysis and interpretation of the K^+K^- mass spectrum have to be understood with special care, since they mirror the product of two couplings: the coupling of the η_c meson to $\eta' f_J$ and the coupling of the f_J resonance to K^+K^-, which are inseparable within this study. However, by analysing further η_c decay channels, for example into the $\pi\pi$, K_SK_S, $\eta\eta$, $\eta'\eta$ or $\eta'\eta'$ channel, the two-coupling dependence might be cleared up. Hence, the study of intermediate states can be carried out quantitatively.
Moreover, the investigation of the still non-observed η_c decay mode to $\eta' K_S K_S$ would be particularly useful. Its branching ratio is expected to be lower by half compared to the result of the $\eta_c \to \eta' K^+K^-$ decay of this analysis. Hence, the implementation of a global PWA taking the two $\eta_c \to \eta' K\overline{K}$ reactions into account with a coupled channel approach is of special interest, here.

Furthermore, besides the investigation of related η_c decay modes to this work, a cross check by studying the same η_c decays using the $\psi(2S)$ data sample, that is also provided by the BESIII experiment and currently expanded significantly, would be very useful. The reason is, that several analysis problems will be avoided by using the $\psi(2S)$ sample, like the distorted η_c line shape at the phase space edge in connection with the merely low energy of the radiative photon, that is emitted whilst the magnetic dipole $M1$ transition of J/ψ to η_c.

6 Appendix

6.1 Appendix A

Event Selection

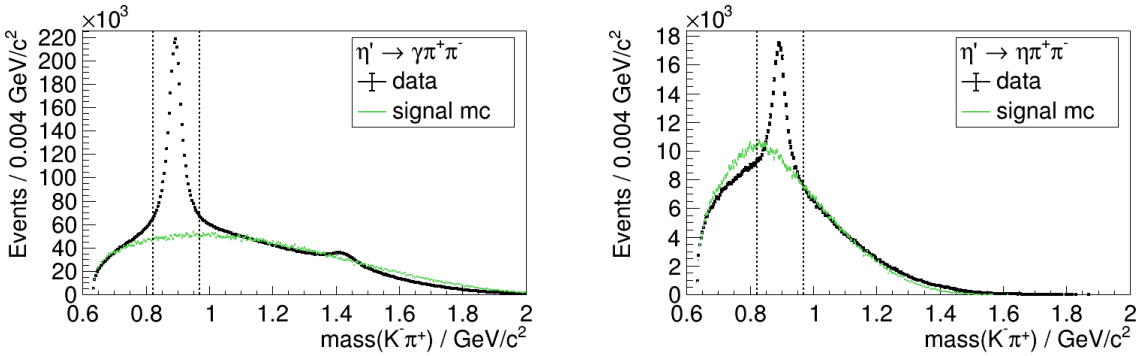

(a) (b)

Figure 35: Invariant $K^-\pi^+$ mass spectra for data in black for the $\eta' \to \gamma\pi^+\pi^-$ channel in (a) and for the $\eta' \to \eta\pi^+\pi^-$ channel in (b). The scaled signal MC simulation is added in green and the $K^*(892)^0$ cut limits are highlighted with black dashed lines.

Evaluation of the Event Selection

2D Histograms of the Invariant Mass of η_c candidates against the Mass of η' candidates

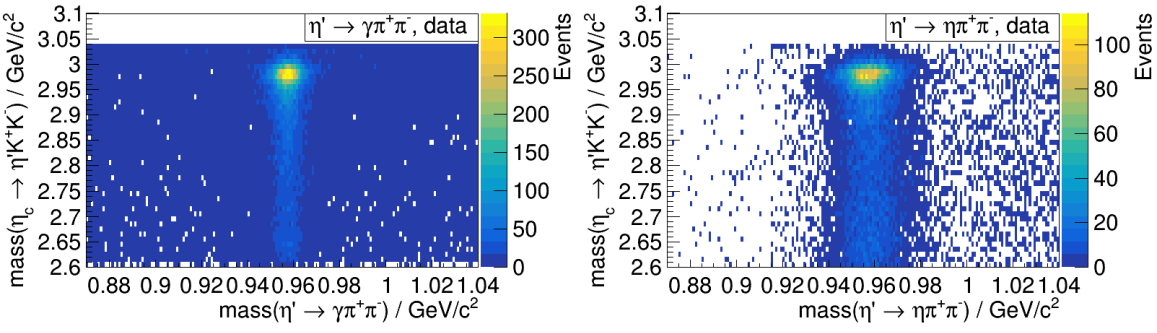

(a) (b)

Figure 36: 2D histograms of data for the "maximal significance" approach, whereby the invariant mass of η' candidates is plotted against the invariant mass of η_c candidates, that is reconstructed via the $\eta' K^+K^-$ mass. The colour of a single bin shows the number of events. On the left the $\eta' \to \gamma\pi^+\pi^-$ channel is pictured, on the right the $\eta' \to \eta\pi^+\pi^-$ channel. Both histograms are plotted after applying all in section 4.1 introduced event selection conditions.

The Invariant Mass Spectra of η' candidates and Sideband Subtraction

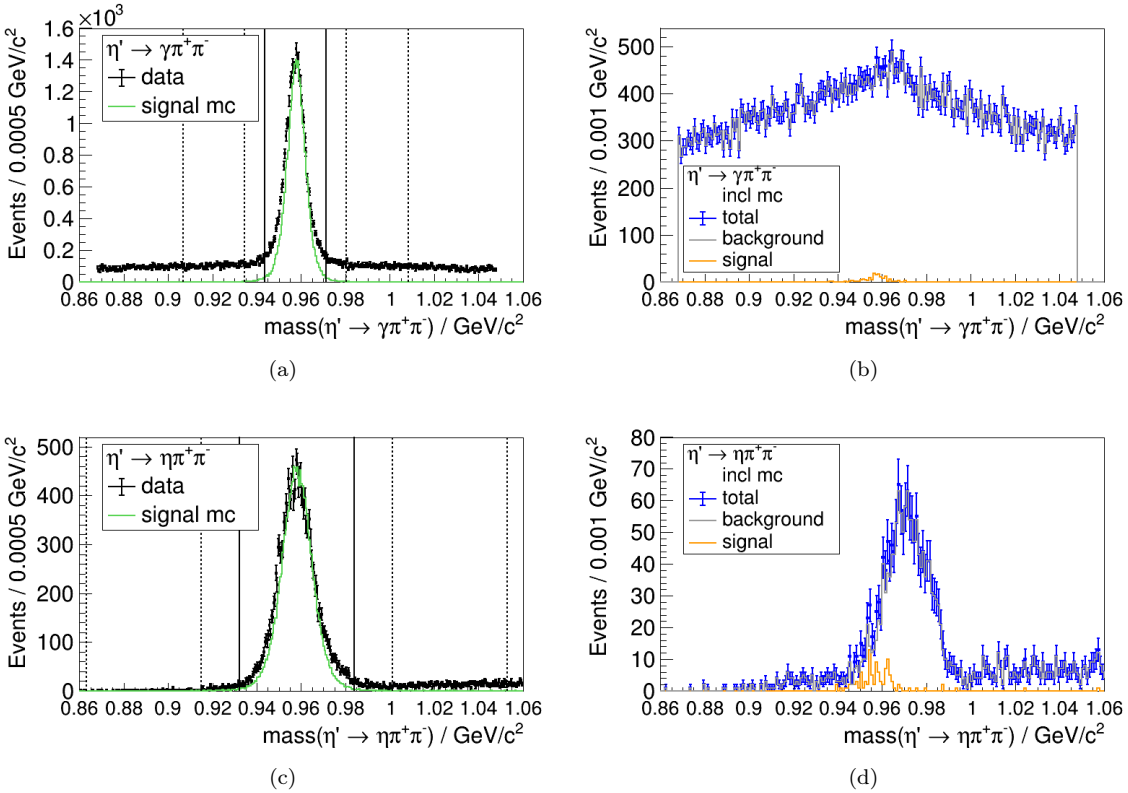

Figure 37: The invariant mass spectra of η' candidates for the "maximal significance" approach of data on the left (marked in black). In addition a scaled signal MC simulation is added with green markers. On the right inclusive MC simulations are pictured. The orange lines represent the signal events of the correct final state, the grey lines show the corresponding background events of the false final state. The total inclusive MC simulation is marked in blue. In the top row the channel $\eta' \to \gamma\pi^+\pi^-$ is considered, below the $\eta' \to \eta\pi^+\pi^-$ channel.

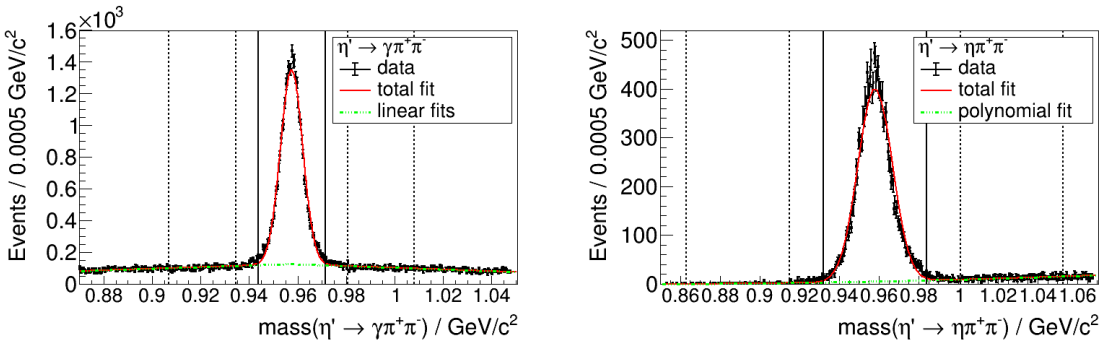

(a) (b)

Figure 38: Fit results of the invariant η' candidate mass spectra of data for the "maximal significance" approach. On the left the channel $\eta' \to \gamma\pi^+\pi^-$ is considered, on the right the $\eta' \to \eta\pi^+\pi^-$ channel. Data points are marked in black, the total fit as red line and the background components of the fit as green dashed line. With black (dashed) vertical lines the signal and sideband region limits are highlighted for applying the sideband subtraction method.

"Maximal Significance" Fit Parameter	**Final State Channel**	
	$\eta' \to \gamma\pi^+\pi^-$	$\eta' \to \eta\pi^+\pi^-$
Background χ^2/NDF	$371.60/301.00 = 1.23$	$241.20/275.00 = 0.88$
Total Fit χ^2/NDF	$560.03/357.00 = 1.57$	$717.51/435.00 = 1.65$
Intensity I / Events $(0.004\ \text{GeV}/c^2)^{-1}$	1221.83 ± 10.17	396.47 ± 3.90
Maximum m_0 / GeV/c^2	0.9575 ± 0.0000	0.9580 ± 0.0001
Width σ / GeV/c^2	0.0046 ± 0.0000	0.0086 ± 0.0001
Weight	0.57 ± 0.01	0.40 ± 0.01

Table 15: Results for the fit parameters of the Gaussian function and the reduced χ^2/NDF values for the background and total fit of the invariant η' candidate mass spectrum of data for both final state channels for the "maximal significance" approach. Via the Gaussian width a signal and two sideband regions are defined. The resulting sideband weight via equation (46) is given.

The Invariant Mass Spectra of η_c candidates

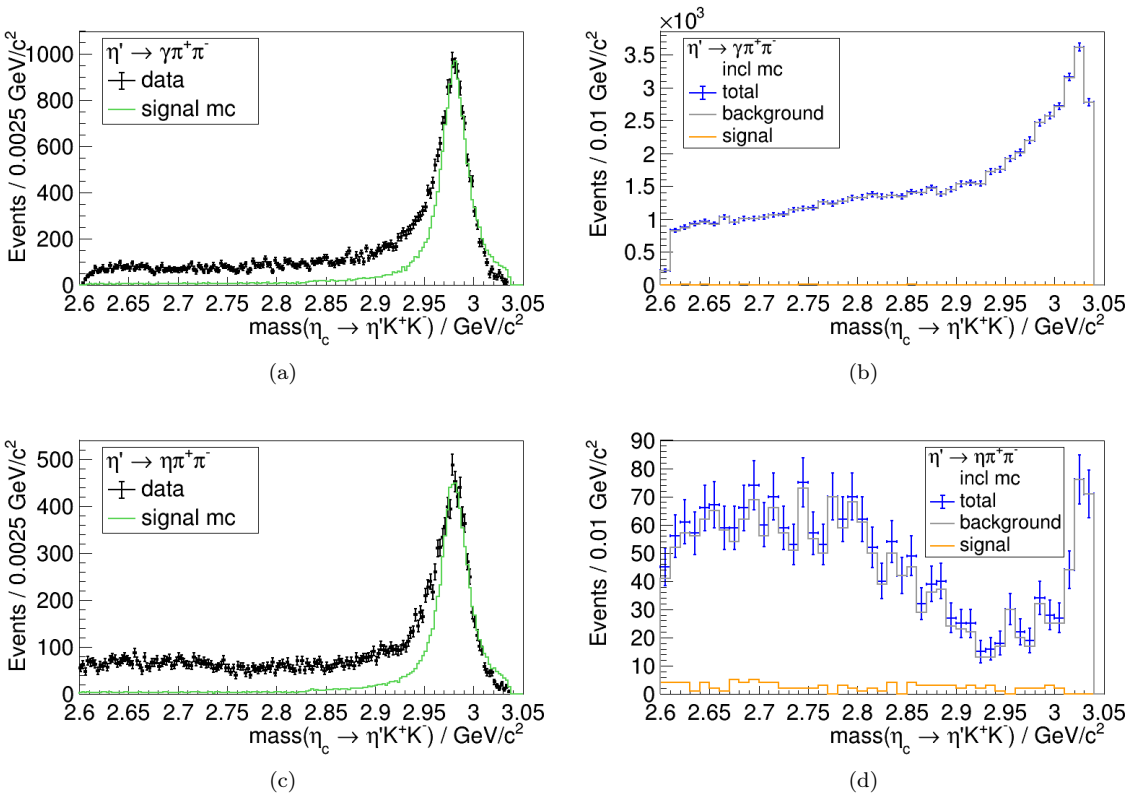

Figure 39: The sideband subtracted invariant $\eta' K^+K^-$ mass spectra of data on the left (marked in black) for the "maximal significance" approach. The scaled signal MC simulation is added as green line. On the right the (non-sideband subtracted) inclusive MC simulations are pictured. With orange and grey lines the signal, respectively background contributions are shown, that have the correct, respectively false final state. The total inclusive MC simulation is marked in blue. In the top row the channel $\eta' \to \gamma\pi^+\pi^-$ is considered, below the $\eta' \to \eta\pi^+\pi^-$ channel.

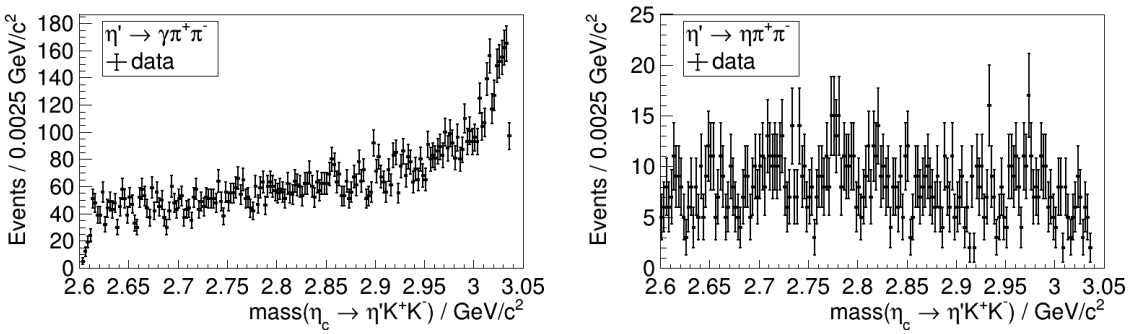

(a) (b)

Figure 40: The invariant η_c sideband mass spectra of data for the "maximal significance" approach. The spectra are filled with η_c events, that are reconstructed via $\eta' K^+ K^-$ and solely lie in the η' sidebands, which are defined in sect. 4.2.2. On the left the channel $\eta' \to \gamma\pi^+\pi^-$ is pictured, on the right the $\eta' \to \eta\pi^+\pi^-$ channel.

6.2 Appendix B

Comparison between Data and MC Simulation. In this appendix the agreement between data and MC simulation is analysed. Possible deviations between data and MC simulation occur for instance due to albeit tiny inaccuracies within the calibration of data or due to a defective resolution within the MC simulation. Since these deviations become usually visible by comparing the widths of the χ^2 distributions, they are considered in figure 41 for both final state channels. The curves are plotted without any applied event selection criteria except the FSFilter cuts. The χ^2_{4C} distributions of data are shown in black. The distributions for the signal MC simulation (S) and the inclusive MC simulation, which represents the background part (B), are marked in green and blue. In red the fit $a \cdot (S + b \cdot B)$ of the scaled and combined MC simulations is shown with a and b being the fit parameters. As can be seen in figure 41 the fits and thus the MC simulations match data well in both cases.

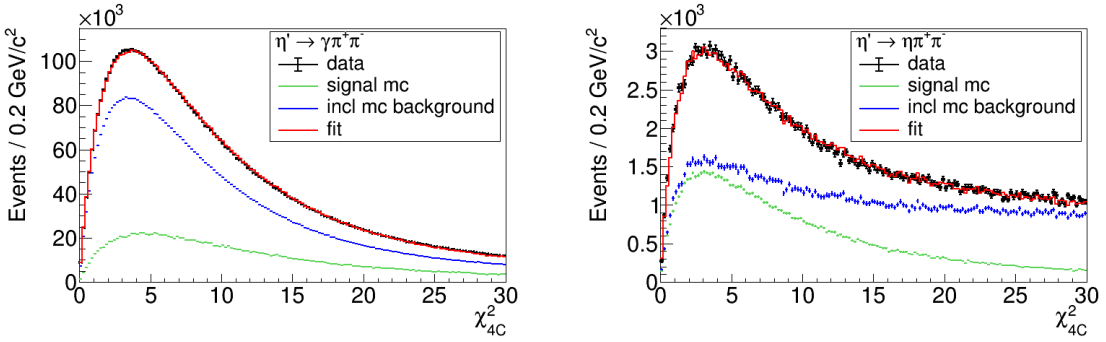

(a) (b)

Figure 41: Comparison between data and MC simulation via the width of their χ^2_{4C} distributions before applying any event selection criteria except the FSFilter cuts. The χ^2_{4C} distribution of real data (black), signal MC simulation (green) and inclusive MC simulation (blue) are plotted in comparison in (a) for the $\eta' \to \gamma K^+K^-$ channel and in (b) for the $\eta' \to \eta K^+K^-$ channel. The red line corresponds to the fit $a \cdot (S + b \cdot B)$ with S being the signal part, which is represented by the signal MC simulation and B being the background part, that is represented by the inclusive MC simulation. The factors a and b are the fit parameters. For the channel in (a) the fit result is $a = (5.571 \pm 0.041)$ and $b = (0.074 \pm 0.001)$ and for (b) $a = (0.324 \pm 0.004)$ and $b = (2.979 \pm 0.054)$.

6.3 Appendix C

PWA Results

"K-Matrix PWA" with "Minimal Background" for the $\eta' \to \gamma\pi^+\pi^-$ Channel

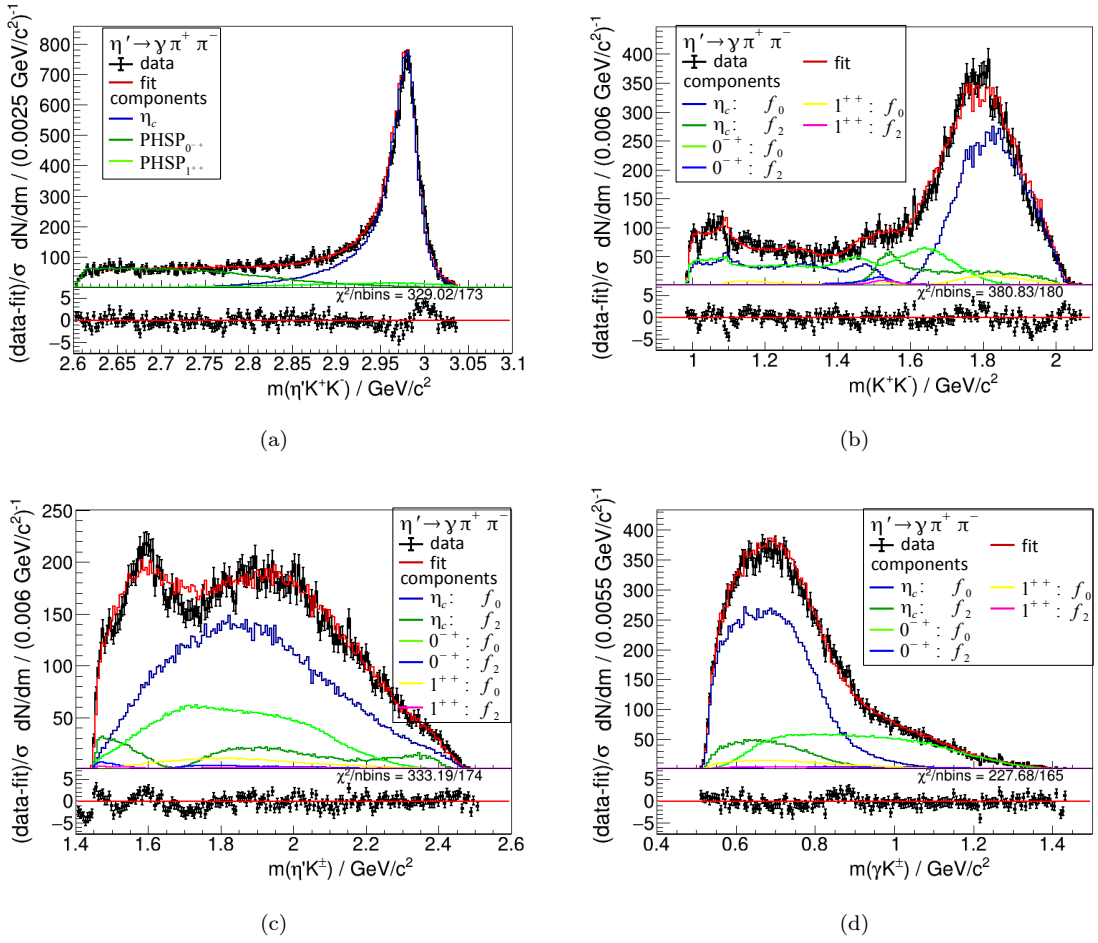

Figure 42: Projections of the PWA-fit results to different invariant masses for the "K-matrix PWA" with "minimal background" for the $\eta' \to \gamma\pi^+\pi^-$ channel. In (a) the invariant $m(\eta' K^+ K^-)$ mass distribution is shown, in (b) the $m(K^+K^-)$ mass spectrum, in (c) the $m(\eta' K^\pm)$ mass spectrum and in (d) the $m(\gamma K^\pm)$ spectrum. The identification of the plotted lines follows the legends pictured. Below the residuals are pictured.

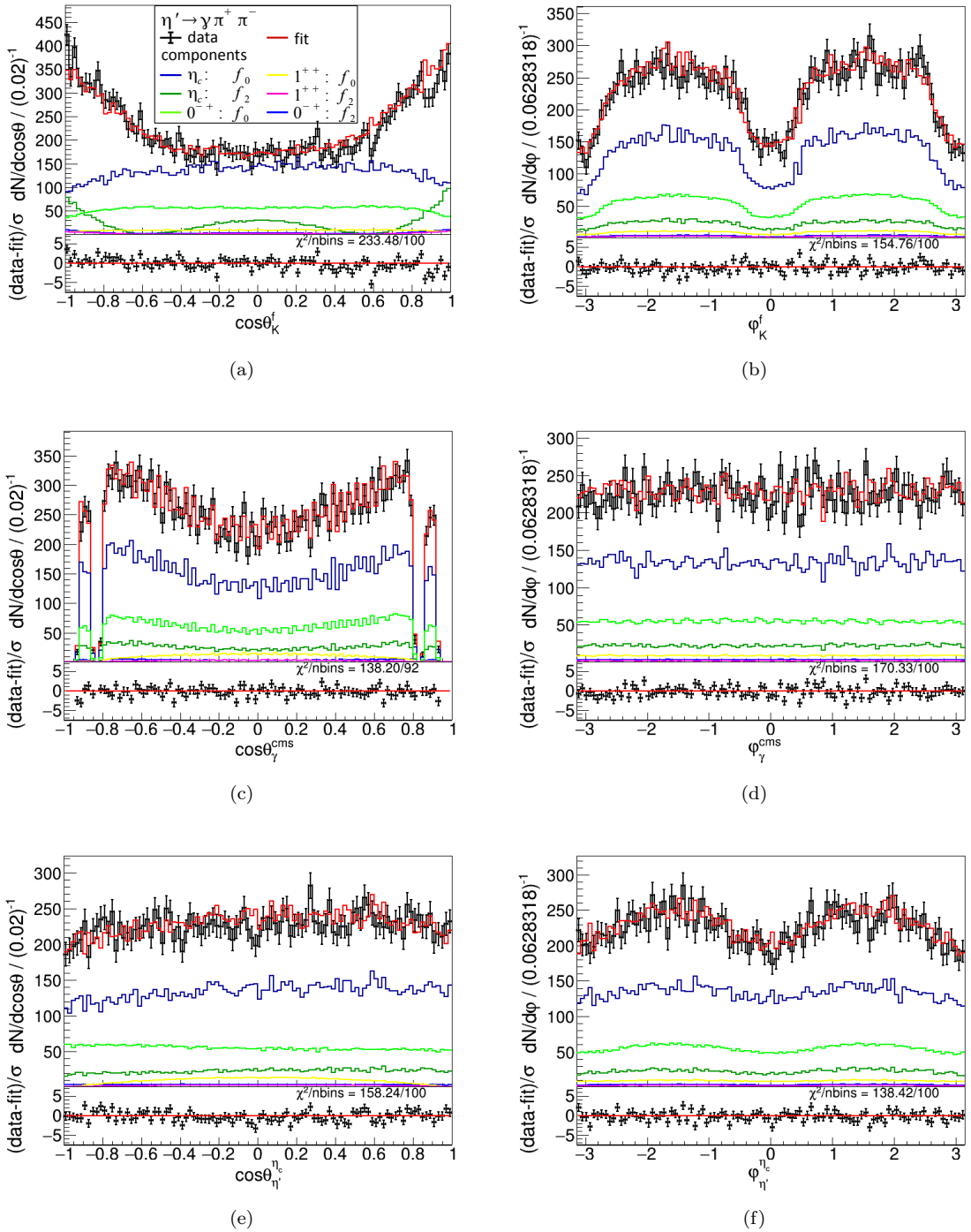

Figure 43: Decay helicity angular distributions for the "K-matrix PWA" with "minimal background" for the $\eta' \to \gamma\pi^+\pi^-$ channel. On the left the projections to the polar decay angle θ are shown, on the right to the azimuthal angle φ. In (a) and (b) the angular distributions of $K^\pm$ in the f rest frame are pictured, in (c) and (d) of η' in the η_c rest frame and in (e) and (f) of the radiative γ in the center of mass system (cms). The identification of the plotted lines follows the legend pictured in (a). Below the residuals are shown.

"K-Matrix PWA" with "Minimal Background" for the $\eta' \to \eta\pi^+\pi^-$ Channel

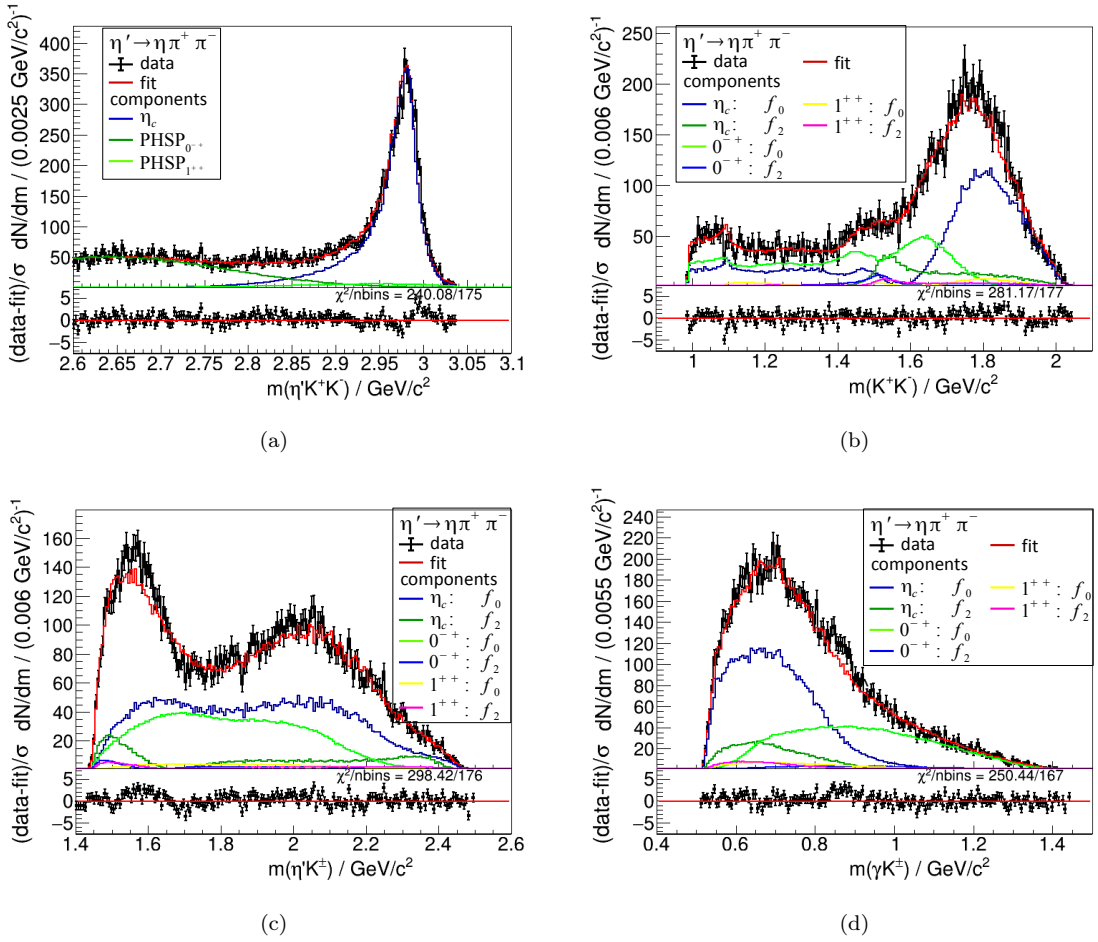

Figure 44: Projections of the PWA-fit results to different invariant masses for the "K-matrix PWA" with "minimal background" for the $\eta' \to \eta\pi^+\pi^-$ channel. In (a) the invariant $m(\eta' K^+ K^-)$ mass distribution is shown, in (b) the $m(K^+K^-)$ mass spectrum, in (c) the $m(\eta' K^\pm)$ mass spectrum and in (d) the $m(\gamma K^\pm)$ spectrum. The identification of the plotted lines follows the legends pictured. Below the residuals are pictured.

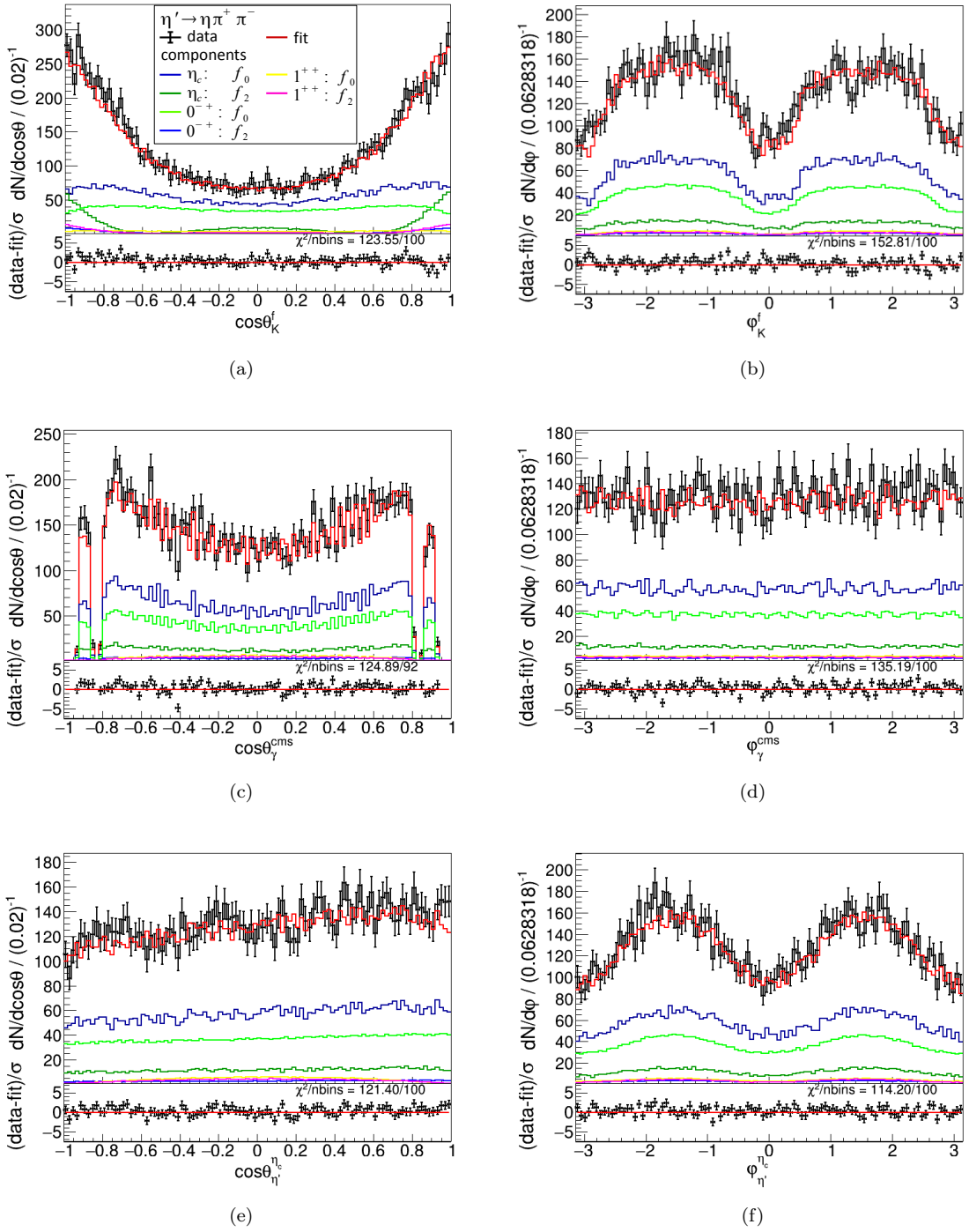

(a) (b) (c) (d) (e) (f)

Figure 45: Decay helicity angular distributions for the "K-matrix PWA" with "minimal background" for the $\eta' \to \eta\pi^+\pi^-$ channel. On the left the projections to the polar decay angle θ are shown, on the right to the azimuthal angle φ. In (a) and (b) the angular distributions of $K^\pm$ in the f rest frame are pictured, in (c) and (d) of η' in the η_c rest frame and in (e) and (f) of the radiative γ in the center of mass system (cms). The identification of the plotted lines follows the legend pictured in (a). Below the residuals are shown.

"K-Matrix PWA" with "Maximal Significance" for the $\eta' \to \gamma\pi^+\pi^-$ Channel

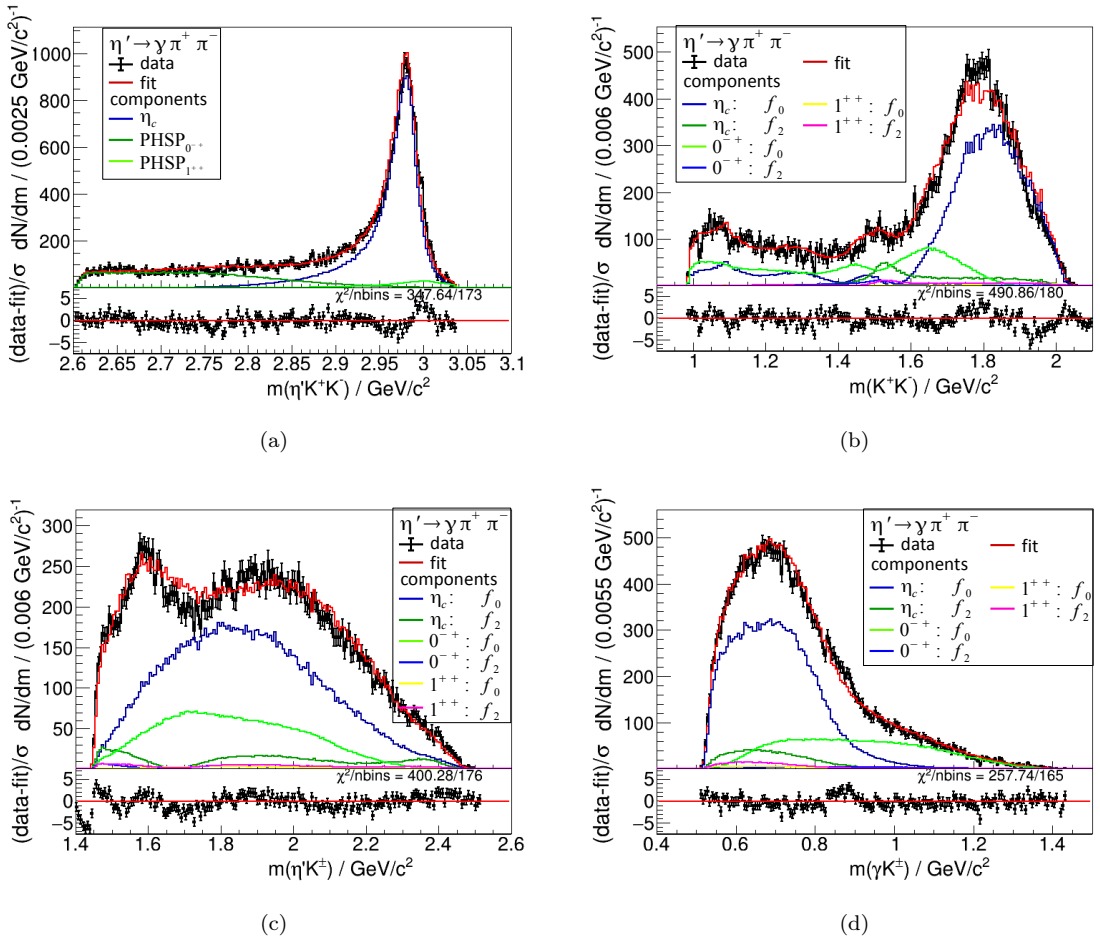

Figure 46: Projections of the PWA-fit results to different invariant masses for the "K-matrix PWA" with "maximal significance" for the $\eta' \to \gamma\pi^+\pi^-$ channel. In (a) the invariant $m(\eta' K^+ K^-)$ mass distribution is shown, in (b) the $m(K^+K^-)$ mass spectrum, in (c) the $m(\eta' K^\pm)$ mass spectrum and in (d) the $m(\gamma K^\pm)$ spectrum. The identification of the plotted lines follows the legends pictured. Below the residuals are pictured.

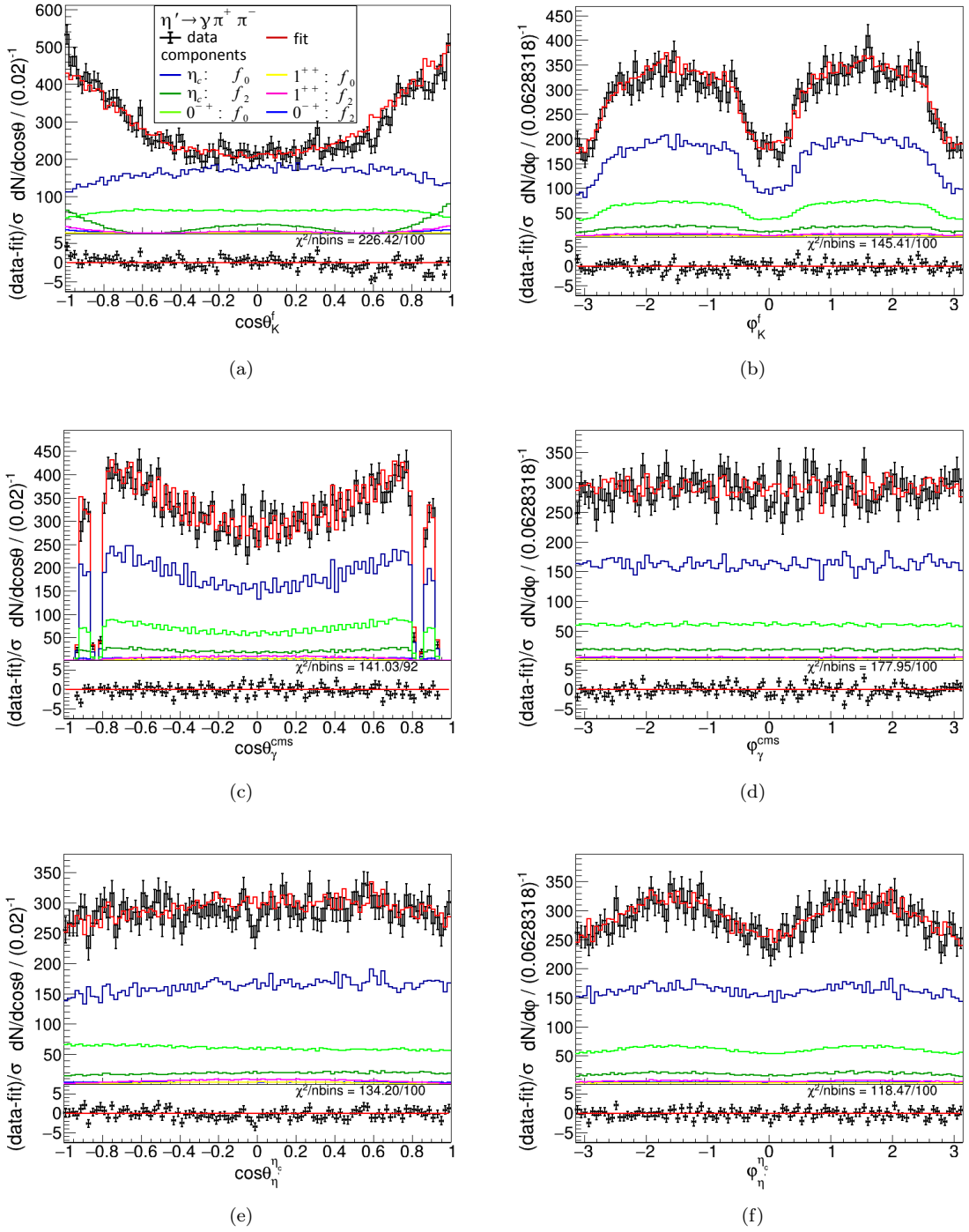

Figure 47: Decay helicity angular distributions for the "K-matrix PWA" with "maximal significance" for the $\eta' \to \gamma\pi^+\pi^-$ channel. On the left the projections to the polar decay angle θ are shown, on the right to the azimuthal angle φ. In (a) and (b) the angular distributions of $K^\pm$ in the f rest frame are pictured, in (c) and (d) of η' in the η_c rest frame and in (e) and (f) of the radiative γ in the center of mass system (cms). The identification of the plotted lines follows the legend pictured in (a). Below the residuals are shown.

"K-Matrix PWA" with "Maximal Significance" for the $\eta' \to \eta\pi^+\pi^-$ Channel

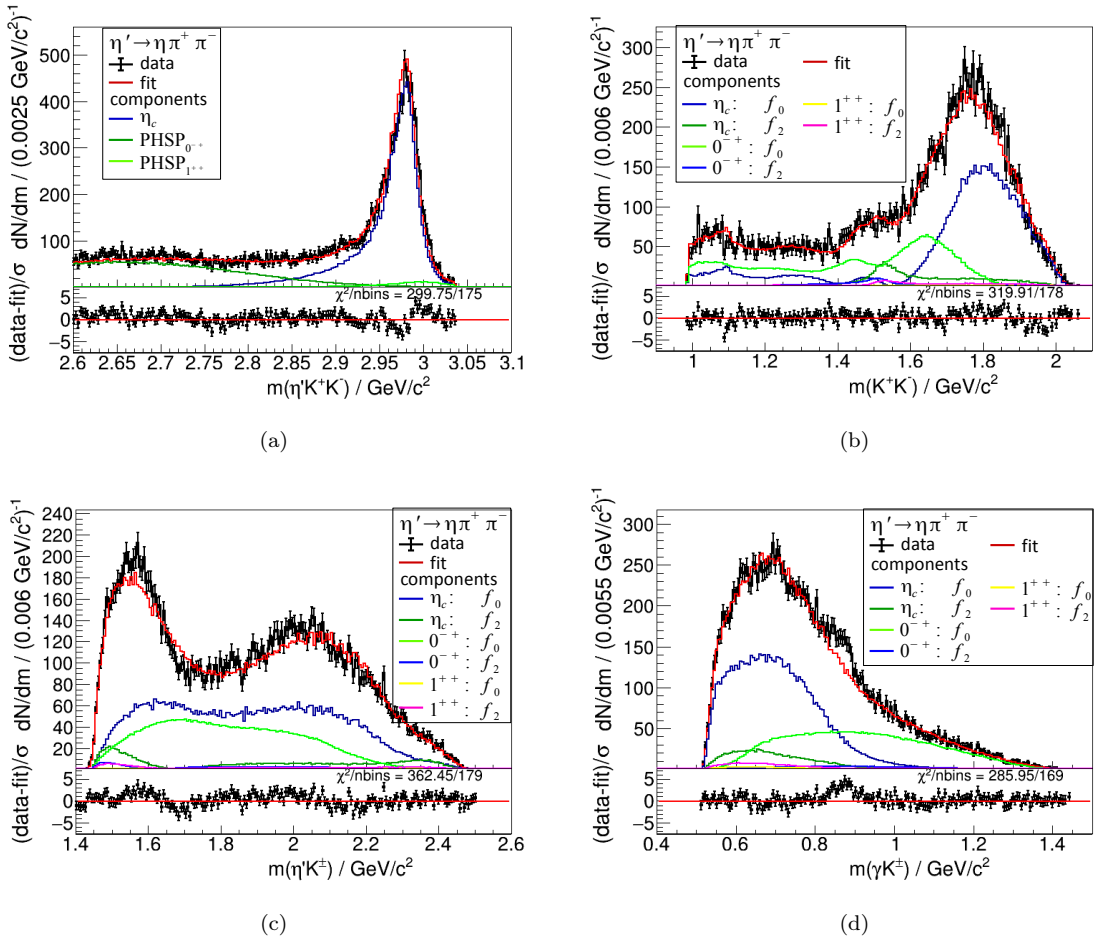

Figure 48: Projections of the PWA-fit results to different invariant masses for the "K-matrix PWA" with "maximal significance" for the $\eta' \to \eta\pi^+\pi^-$ channel. In (a) the invariant $m(\eta' K^+ K^-)$ mass distribution is shown, in (b) the $m(K^+K^-)$ mass spectrum, in (c) the $m(\eta' K^\pm)$ mass spectrum and in (d) the $m(\gamma K^\pm)$ spectrum. The identification of the plotted lines follows the legends pictured. Below the residuals are pictured.

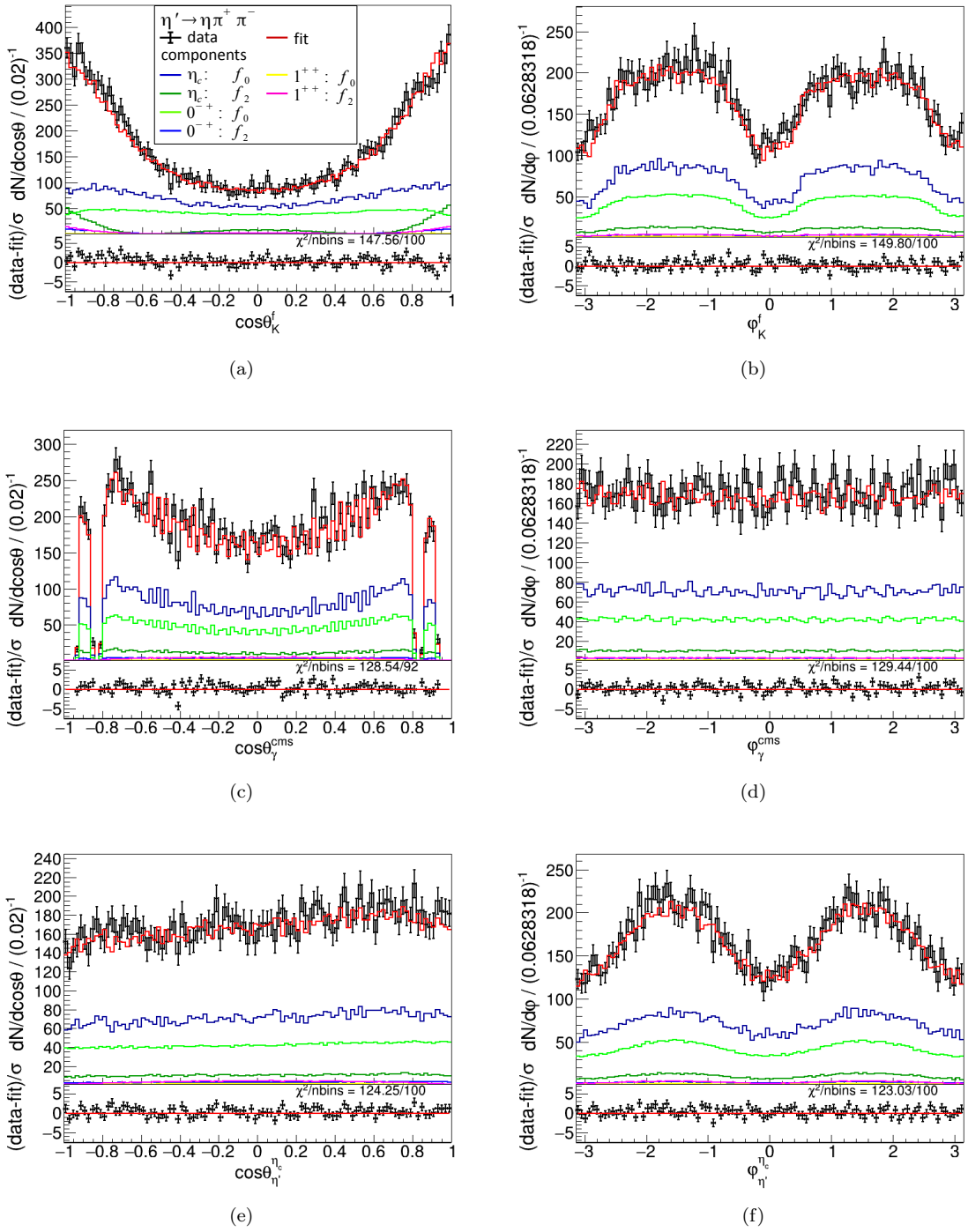

(a) (b) (c) (d) (e) (f)

Figure 49: Decay helicity angular distributions for the "K-matrix PWA" with "maximal significance" for the $\eta' \to \eta\pi^+\pi^-$ channel. On the left the projections to the polar decay angle θ are shown, on the right to the azimuthal angle φ. In (a) and (b) the angular distributions of $K^\pm$ in the f rest frame are pictured, in (c) and (d) of η' in the η_c rest frame and in (e) and (f) of the radiative γ in the center of mass system (cms). The identification of the plotted lines follows the legend pictured in (a). Below the residuals are shown.

"Breit-Wigner PWA" with "Minimal Background" for the $\eta' \to \gamma\pi^+\pi^-$ Channel

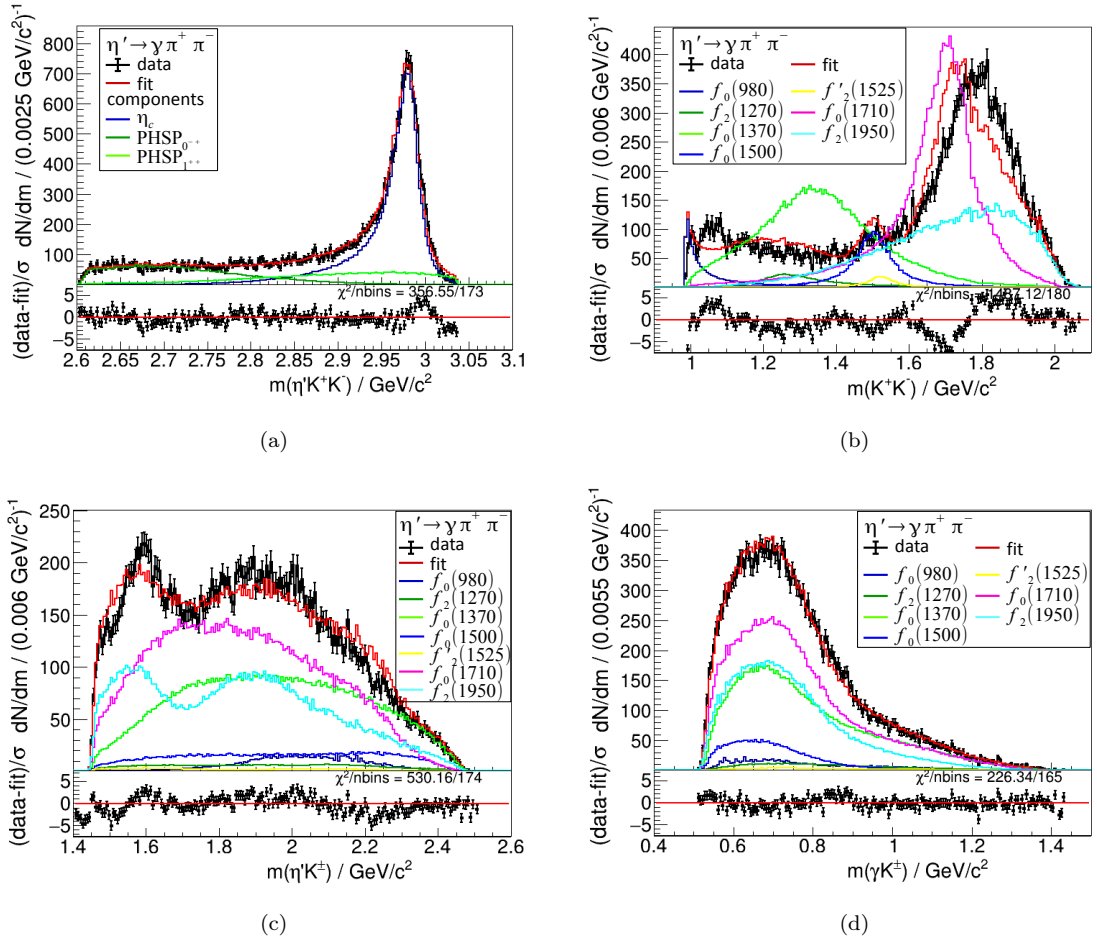

Figure 50: Projections of the PWA-fit results to different invariant masses for the "Breit-Wigner PWA" with "minimal background" for the $\eta' \to \gamma\pi^+\pi^-$ channel. In (a) the invariant $m(\eta' K^+ K^-)$ mass distribution is shown, in (b) the $m(K^+K^-)$ mass spectrum, in (c) the $m(\eta' K^\pm)$ mass spectrum and in (d) the $m(\gamma K^\pm)$ spectrum. The identification of the plotted lines follows the legends pictured. Below the residuals are pictured.

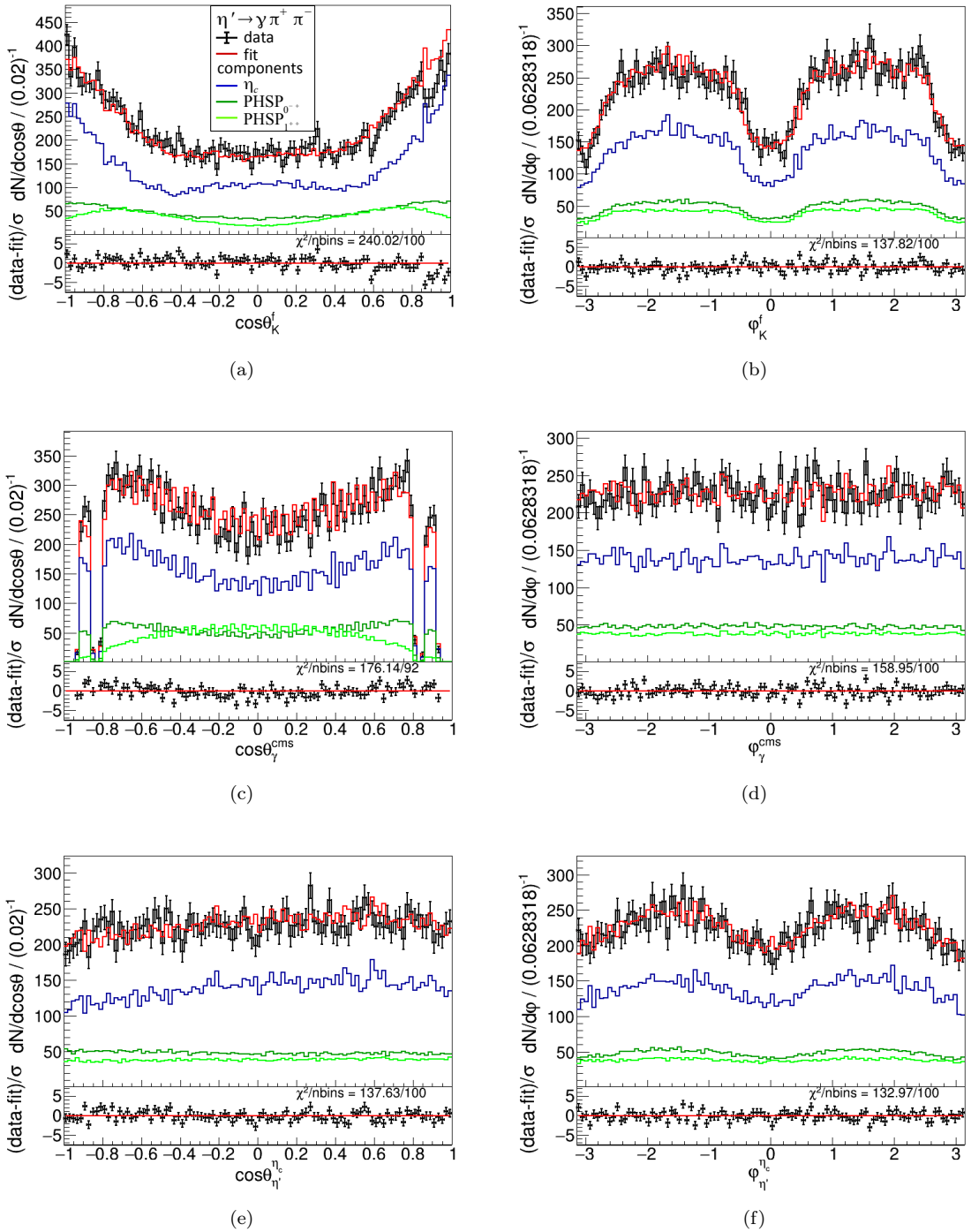

(a) (b) (c) (d) (e) (f)

Figure 51: Decay helicity angular distributions for the "Breit-Wigner PWA" with "minimal background" for the $\eta' \to \gamma\pi^+\pi^-$ channel. On the left the projections to the polar decay angle θ are shown, on the right to the azimuthal angle φ. In (a) and (b) the angular distributions of $K^\pm$ in the f rest frame are pictured, in (c) and (d) of η' in the η_c rest frame and in (e) and (f) of the radiative γ in the center of mass system (cms). The identification of the plotted lines follows the legend pictured in (a). Below the residuals are shown.

"Breit-Wigner PWA" with "Minimal Background" for the $\eta' \to \eta\pi^+\pi^-$ Channel

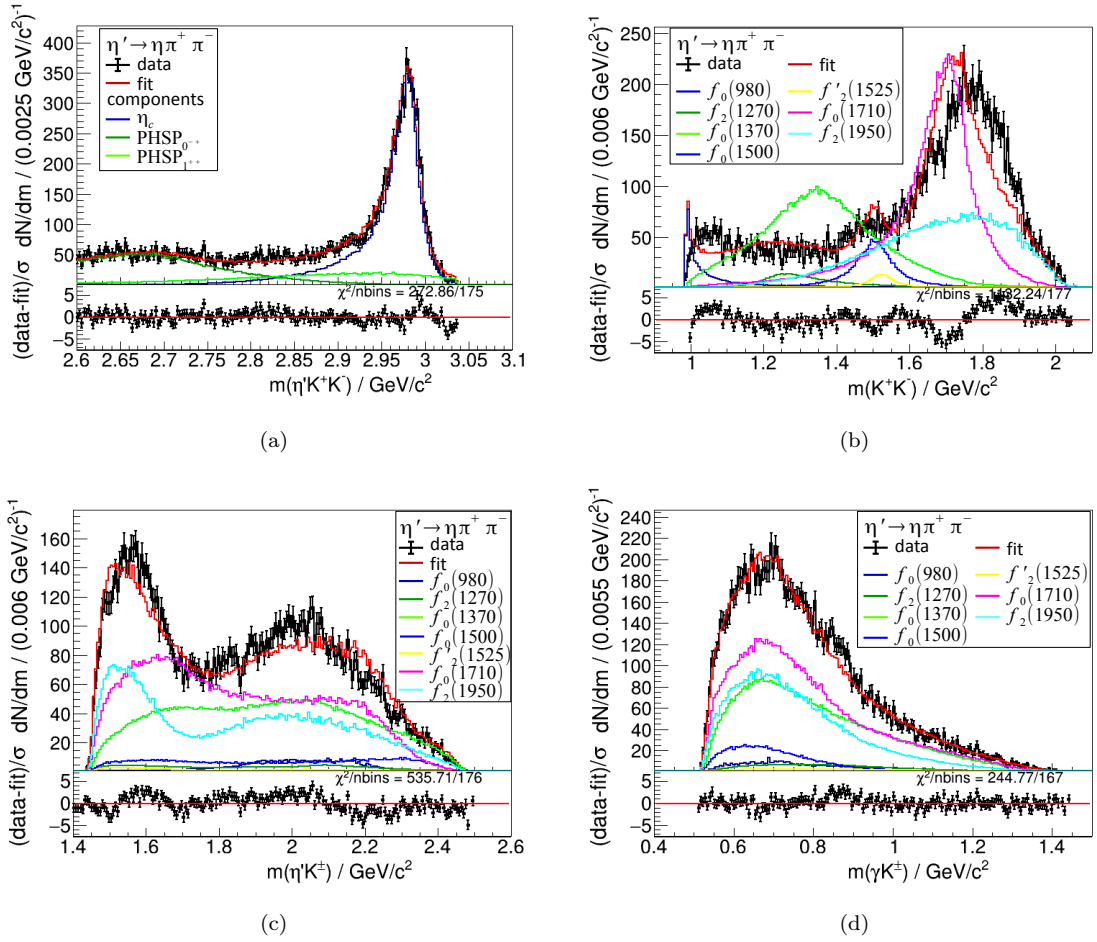

Figure 52: Projections of the PWA-fit results to different invariant masses for the "Breit-Wigner PWA" with "minimal background" for the $\eta' \to \eta\pi^+\pi^-$ channel. In (a) the invariant $m(\eta' K^+ K^-)$ mass distribution is shown, in (b) the $m(K^+K^-)$ mass spectrum, in (c) the $m(\eta' K^\pm)$ mass spectrum and in (d) the $m(\gamma K^\pm)$ spectrum. The identification of the plotted lines follows the legends pictured. Below the residuals are pictured.

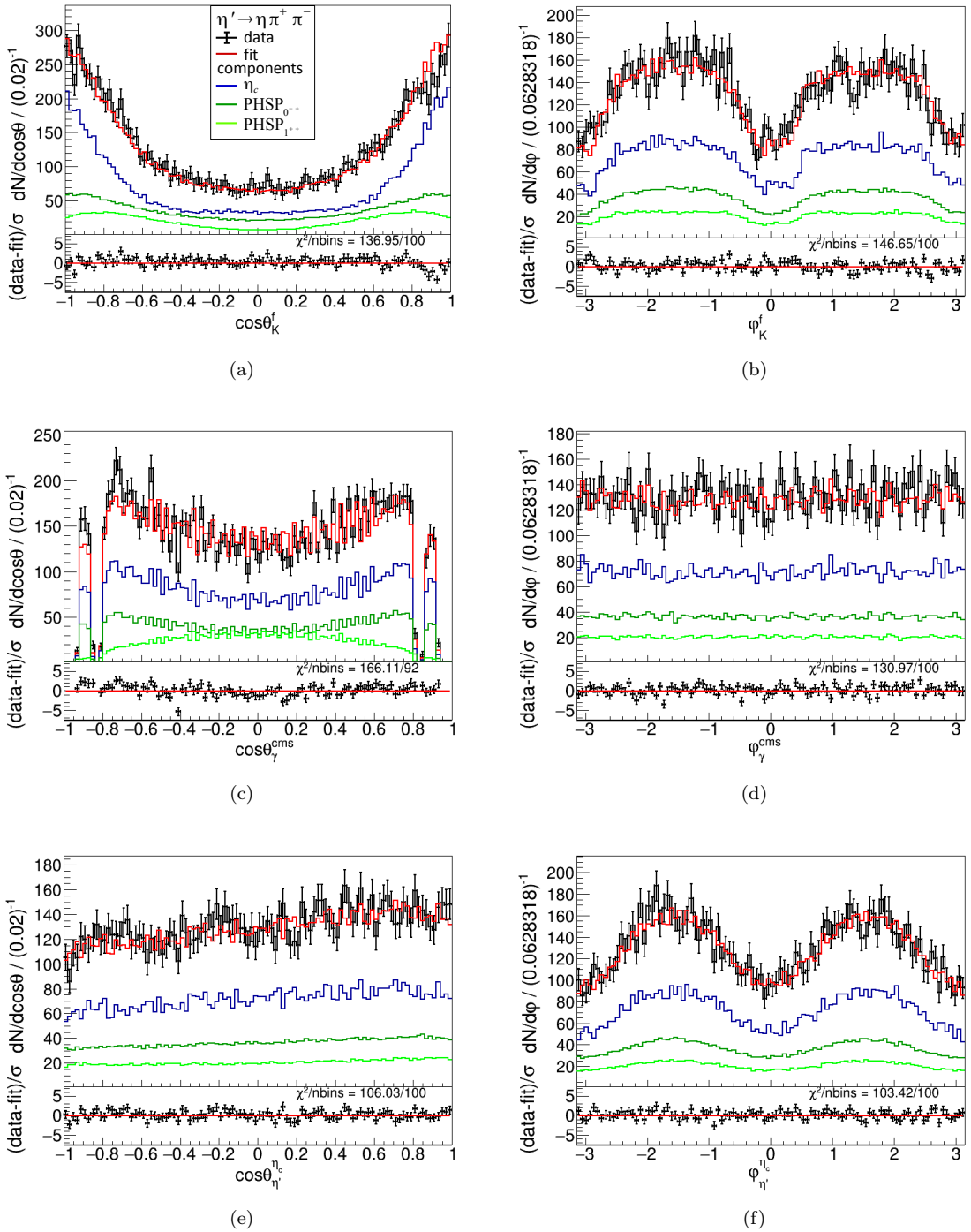

(a) (b) (c) (d) (e) (f)

Figure 53: Decay helicity angular distributions for the "Breit-Wigner PWA" with "minimal background" for the $\eta' \to \eta\pi^+\pi^-$ channel. On the left the projections to the polar decay angle θ are shown, on the right to the azimuthal angle φ. In (a) and (b) the angular distributions of $K^\pm$ in the f rest frame are pictured, in (c) and (d) of η' in the η_c rest frame and in (e) and (f) of the radiative γ in the center of mass system (cms). The identification of the plotted lines follows the legend pictured in (a). Below the residuals are shown.

"Breit-Wigner PWA" with "Maximal Significance" for the $\eta' \to \gamma\pi^+\pi^-$ Channel

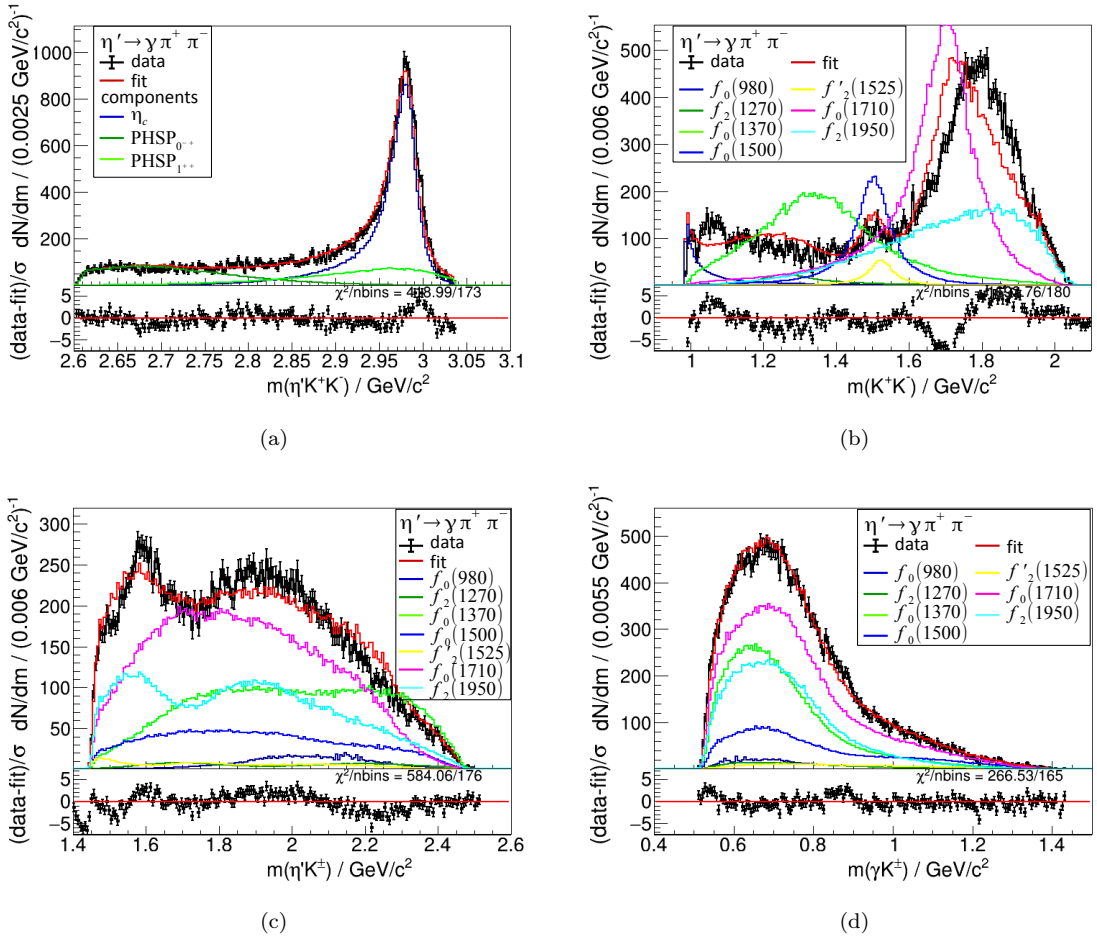

Figure 54: Projections of the PWA-fit results to different invariant masses for the "Breit-Wigner PWA" with "maximal significance" for the $\eta' \to \gamma\pi^+\pi^-$ channel. In (a) the invariant $m(\eta' K^+ K^-)$ mass distribution is shown, in (b) the $m(K^+K^-)$ mass spectrum, in (c) the $m(\eta' K^\pm)$ mass spectrum and in (d) the $m(\gamma K^\pm)$ spectrum. The identification of the plotted lines follows the legends pictured. Below the residuals are pictured.

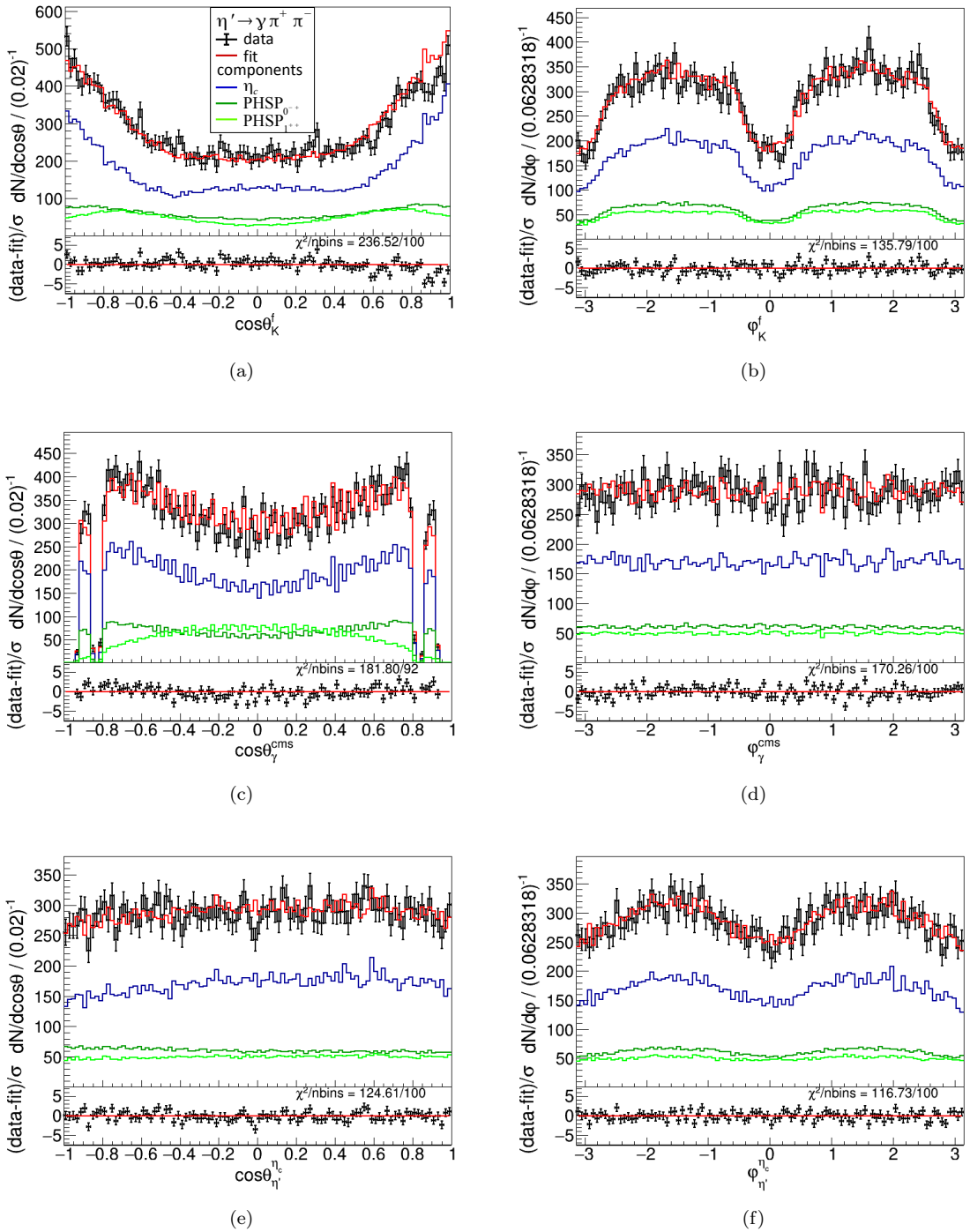

Figure 55: Decay helicity angular distributions for the "Breit-Wigner PWA" with "maximal significance" for the $\eta' \to \gamma\pi^+\pi^-$ channel. On the left the projections to the polar decay angle θ are shown, on the right to the azimuthal angle φ. In (a) and (b) the angular distributions of $K^\pm$ in the f rest frame are pictured, in (c) and (d) of η' in the η_c rest frame and in (e) and (f) of the radiative γ in the center of mass system (cms). The identification of the plotted lines follows the legend pictured in (a). Below the residuals are shown.

"Breit-Wigner PWA" with "Maximal Significance" for the $\eta' \to \eta\pi^+\pi^-$ Channel

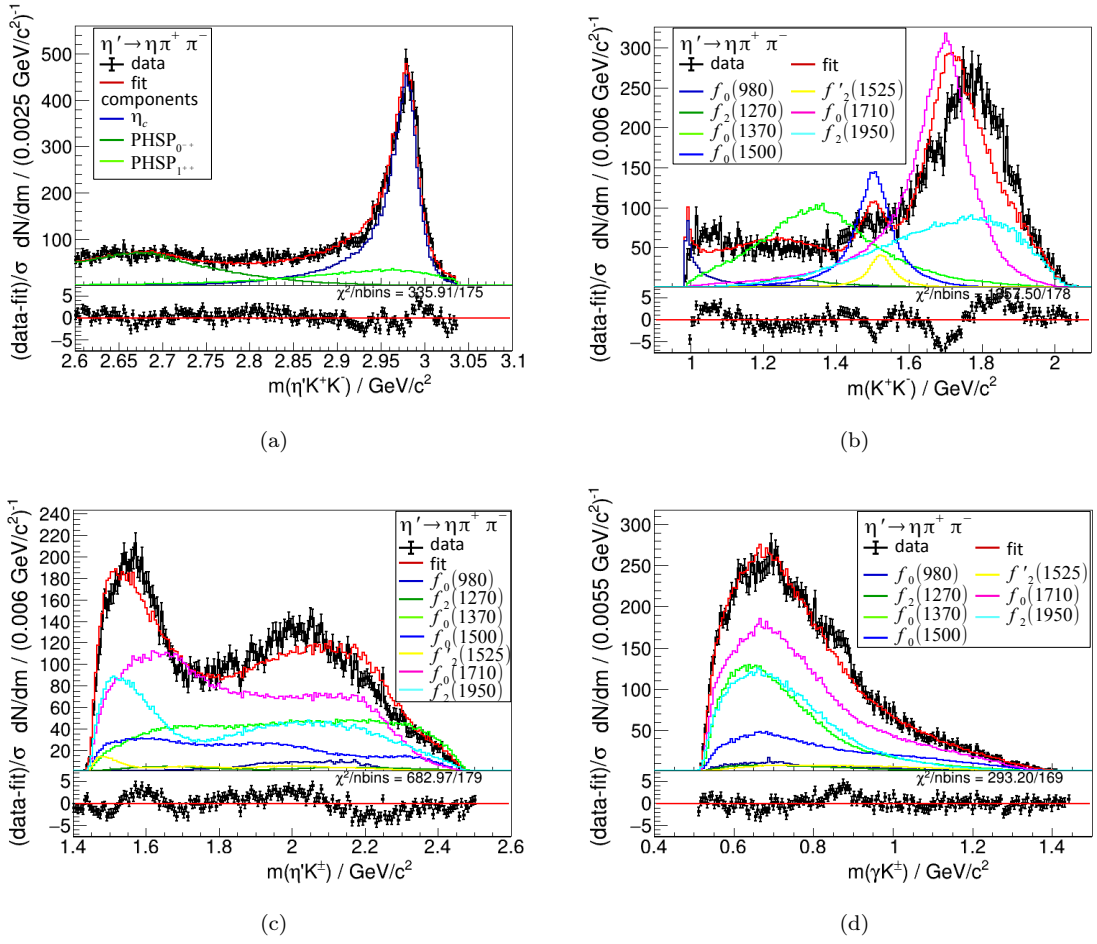

Figure 56: Projections of the PWA-fit results to different invariant masses for the "Breit-Wigner PWA" with "maximal significance" for the $\eta' \to \eta\pi^+\pi^-$ channel. In (a) the invariant $m(\eta' K^+ K^-)$ mass distribution is shown, in (b) the $m(K^+K^-)$ mass spectrum, in (c) the $m(\eta' K^\pm)$ mass spectrum and in (d) the $m(\gamma K^\pm)$ spectrum. The identification of the plotted lines follows the legends pictured. Below the residuals are pictured.

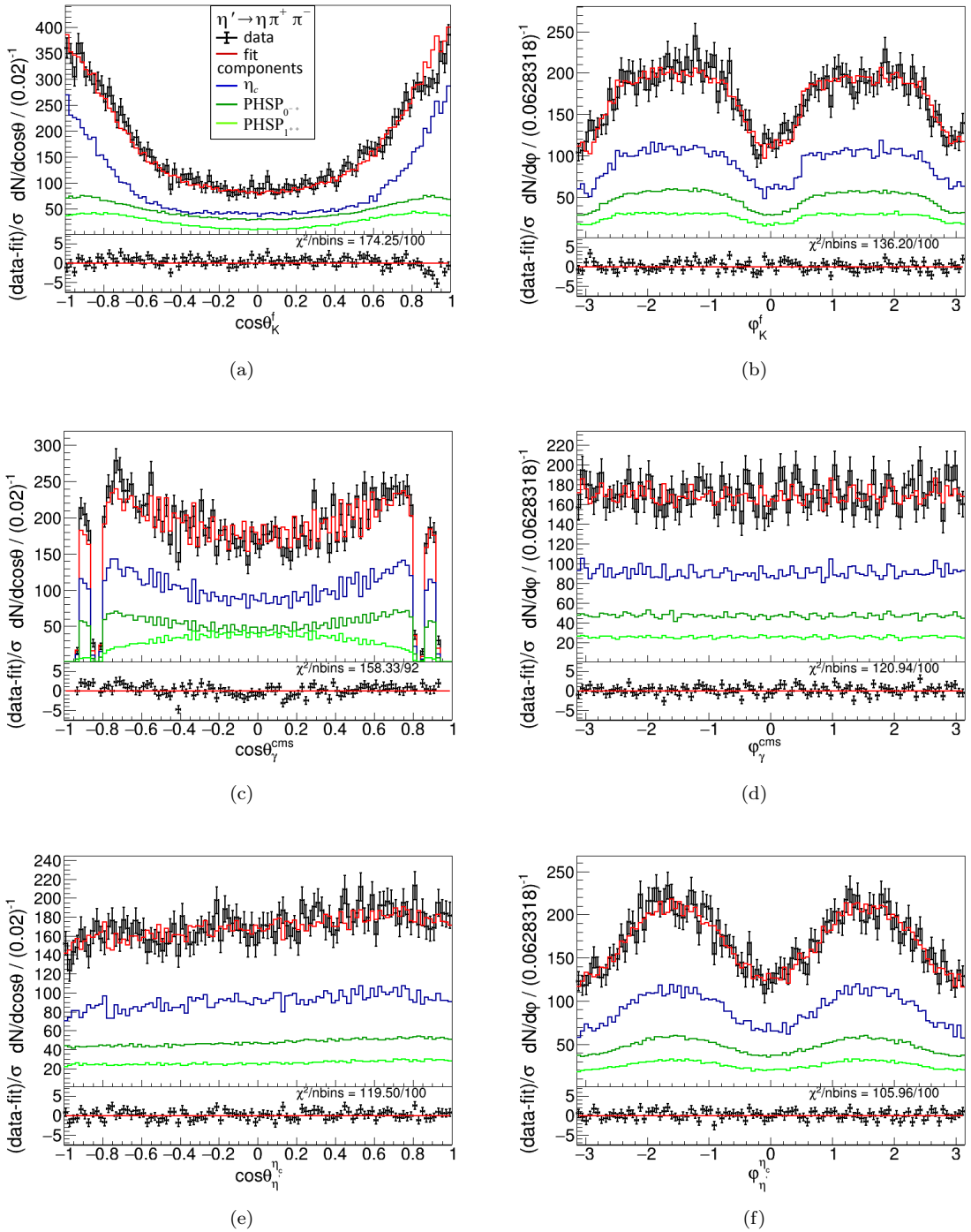

Figure 57: Decay helicity angular distributions for the "Breit-Wigner PWA" with "maximal significance" for the $\eta' \to \eta\pi^+\pi^-$ channel. On the left the projections to the polar decay angle θ are shown, on the right to the azimuthal angle φ. In (a) and (b) the angular distributions of $K^\pm$ in the f rest frame are pictured, in (c) and (d) of η' in the η_c rest frame and in (e) and (f) of the radiative γ in the center of mass system (cms). The identification of the plotted lines follows the legend pictured in (a). Below the residuals are shown.

References

[1] W. Demtröder. *Experimentalphysik 4: Kern-, Teilchen- und Astrophysik*. Springer-Lehrbuch. Springer Berlin Heidelberg, 2013.

[2] W. Demtröder. *Experimentalphysik 3: Atome, Moleküle und Festkörper*. Springer-Lehrbuch. Springer Berlin Heidelberg, 2010.

[3] J.J. Thomson. On the Structure of the Atom: an Investigation of the Stability and Periods of Oscillation of a number of Corpuscles arranged at equal intervals around the Circumference of a Circle; with Application of the results to the Theory of Atomic Structure. *The London, Edinburgh, and Dublin Philosophical Magazine and Journal of Science, Series 6*, 7(39):237–265, Mar 1904.

[4] E. Rutherford. The Scattering of α and β Particles by Matter and the Structure of the Atom. *The London, Edinburgh, and Dublin Philosophical Magazine and Journal of Science, Series 6*, 21:669–688, 1911.

[5] J. Chadwick. The Existence of a Neutron. *Proceedings Royal Society London*, A 136:692–708, Jun 1932.

[6] B. Povh, K. Rith, C. Scholz, and F. Zetsche. *Teilchen und Kerne*. Physics and Astronomy online Library. Springer Berlin Heidelberg, 2014.

[7] M. Gell-Mann. A Schematic Model of Baryons and Mesons. *Physical Letters*, 8:214–215, Feb 1964.

[8] P.A. Zyla et al. Review of Particle Physics: 15. Quark Model. *Progress of Theoretical and Experimental Physics*, 2020(8):083C01, 2020.

[9] P.A. Zyla et al. Review of Particle Physics: 78. Non-$q\overline{q}$ Mesons. *Progress of Theoretical and Experimental Physics*, 2020(8):083C01, 2020.

[10] M. Ablikim et al. (BESIII Collaboration). Observation of a Near-Threshold Structure in the K^+ Recoil-Mass Spectra in $e^+e^- \to K^+(D_s^- D^{*0} + D_s^{*-} D^0)$. *Physical Review Letters*, 126(10):102001, Mar 2021.

[11] W. I. Eshraim and C. S. Fischer. Hadronic decays of the (pseudo-)scalar charmonium states η_c and χ_{c0} in the extended Linear Sigma Model. *The European Physical Journal A*, 54(8):139, Aug 2018.

[12] P.A. Zyla et al. Review of Particle Physics. *Progress of Theoretical and Experimental Physics*, 2020(8):083C01, 2020.

[13] H. Fritzsch, M. Gell-Mann, and H. Leutwyler. Advantages of the Color Octet Gluon Picture. *Physics Letters B*, 47:365–368, 1973.

[14] A. Khoukaz, C. Klein-Bösing, C. Weinheimer, and J. Wessels. *Skript zur Vorlesung Kern- und Teilchenphysik II*. Westfälische Wilhelms-Universität, Institut für Kernphysik, Mar 2018.

[15] G. Münster. *Quantentheorie*. De Gruyter, 2010.

[16] J. C. Morrison. Chapter 13 - Particle Physics. In *Modern Physics (Second Edition)*, pages 303–352. Academic Press, Boston, second edition, 2015.

[17] H. S. Chung, J. Lee, and D. Kang. Cornell Potential Parameters for S-Wave Heavy Quarkonia. *Journal of the Korean Physical Society*, 52(4):1151–1154, Apr 2008.

[18] J. P. Lees. Light meson spectroscopy from Dalitz plot analyses of η_c decays to $\eta' K^+ K^-$, $\eta' \pi^+ \pi^-$, and $\eta \pi^+ \pi^-$ produced in two-photon interactions, 2021. submitted.

[19] T. Barnes, S. Godfrey, and E. S. Swanson. Higher Charmonia. *Physical Review D*, 72(5):054026, Sep 2005.

[20] R. E. Mitchell et al. (CLEO Collaboration). J/ψ and $\psi(2S)$ Radiative Decays to η_c. *Physical Review Letters*, 102:011801, Jan 2009.

[21] P.A. Zyla et al. Review of Particle Physics: 62. Scalar Mesons below 2 GeV. *Progress of Theoretical and Experimental Physics*, 2020(8):083C01, 2020.

[22] Z.-G. Wang. Analysis of the scalar nonet mesons with QCD sum rules. *The European Physical Journal C*, 76(8):427, Jul 2016.

[23] G.S. Bali, K. Schilling, A. Hulsebos, A.C. Irving, C. Michael, and P.W. Stephenson. A comprehensive lattice study of SU(3) glueballs. *Physics Letters B*, 309(3-4):378–384, Jul 1993.

[24] Y. Chen et al. Glueball Spectrum and Matrix Elements on Anisotropic Lattices. *Physical Review D*, 73(1):014516, Jan 2006.

[25] E. Gregory, A. Irving, B. Lucini, C. McNeile, A. Rago, C. Richards, and E. Rinaldi. Towards the glueball spectrum from unquenched lattice QCD. *Journal of High Energy Physics*, 2012(10):170, Oct 2012.

[26] F. Brünner, A. Rebhan. Nonchiral Enhancement of Scalar Glueball Decay in the Witten-Sakai-Sugimoto Model. *Physical Review Letters*, 115(13):131601, Sep 2015.

[27] M. Albaladejo and J. A. Oller. Identification of a Scalar Glueball. *Physical Review Letters*, 101(25):252002, Dec 2008.

[28] C. Amsler and F. E. Close. Is $f0(1500)$ a scalar glueball? *Physical Review D*, 53(1):295–311, Jan 1996.

[29] F. E. Close and Q. Zhao. Production of $f0(1710)$, $f0(1500)$, and $f0(1370)$ in J/ψ hadronic decays. *Physical Review D*, 71(9):094022, May 2005.

[30] S. Janowski, F. Giacosa, and D. H. Rischke. Is $f0(1710)$ a glueball? *Physical Review D*, 90(11):114005, Dec 2014.

[31] Q. Zhao. $\chi_{c0,2}$ decay into light meson pairs and its implication of the scalar meson structures. *Physics Letters B*, 659(1-2):221–227, Jan 2008.

[32] K. J. Peters. A Primer on Partial Wave Analysis. *International Journal of Modern Physics A*, 21:5618–5624, 2006.

[33] M. Albrecht. *Partial Wave Analysis of the Decay $J/\psi \to \gamma\omega\omega$ at BESIII and Developments for the Electromagnetic Calorimeter of the $\bar{P}ANDA$ Detector.* Doctoral Thesis, Ruhr-Universität Bochum, Universitätsbibliothek, 2016.

[34] M. A. Rump. *Search for couplings of exotic charmonia to light hadron final states involving a $p\bar{p}$ pair at BESIII.* Doctoral Thesis, Westfälische Wilhelms-Universität Münster, Institut of Nuclear Physics, 2019.

[35] S. U. Chung. SPIN FORMALISMS. *CERN Yellow Reports: Monographs*, Mar 1971.

[36] P.A. Zyla et al. Review of Particle Physics: 45. Clebsch-Gordan Coefficients, Spherical Harmonics, and d Functions. *Progress of Theoretical and Experimental Physics*, 2020(8):083C01, 2020.

[37] J. D. Richman. An Experimenter's Guide to the Helicity Formalism. *CALT-68-1148*, Jun 1984.

[38] M. Artuso et al. (CLEO Collaboration). Higher-order multipole amplitudes in charmonium radiative transitions. *Physical Review D*, 80:112003, Dec 2009.

[39] N. Wu. Centrifugal-Barrier Effects and Determination of Interaction Radius. *Communications in Theoretical Physics*, 61(1):89–94, Jan 2014.

[40] J. Back and et al. Laura++: A Dalitz plot fitter. *Computer Physics Communications*, 231:198–242, Oct 2018.

[41] V.V. Anisovich and A.V. Sarantsev. K-matrix analysis of the ($IJ^{PC} = 00^{++}$)-wave in the mass region below 1900 MeV. *The European Physical Journal A*, 16(2):229–258, Feb 2003.

[42] I.J.R. Aitchison. The K-matrix formalism for overlapping resonances. *Nuclear Physics A*, 189(2):417–423, 1972.

[43] M. Ablikim et al. (BESIII-Collaboration). Search for the rare semi-leptonic decay $J/\psi \to D^- e^+ \nu_e + c.c.$. *Journal of High Energy Physics*, Jul 2021. submitted.

[44] F. A. Harris. BEPCII and BESIII. *International Journal of Modern Physics A*, 24:377–384, 2009.

[45] M. Ablikim et al. (BESIII Collaboration). Design and Construction of the BESIII Detector. *Nuclear Instruments and Methods in Physics Research Section A: Accelerators, Spectrometers, Detectors and Associated Equipment*, 614(3):345–399, Mar 2010.

[46] D. M. Asner et al. Physics at BES-III. *International Journal of Modern Physics A*, 24:S1–794, 2009.

[47] Institue of High Energy Physics. BEPC & BEPCII, 2021. URL http://english.ihep.cas.cn/doc/1840.html (visited on 12.07.2021, 17:53 Uhr).

[48] Institue of High Energy Physics. BESIII, 2021. URL http://english.ihep.cas.cn/doc/2124.html (visited on 14.05.2021, 23:41 Uhr).

[49] Institue of High Energy Physics. MDC, 2021. URL http://english.ihep.cas.cn/doc/2156.html#ad-image-15 (visited on 15.05.2021, 23:49 Uhr).

[50] F.A. Harris et al. BES3 time-of-flight monitoring system. *Nuclear Instruments and Methods in Physics Research Section A: Accelerators, Spectrometers, Detectors and Associated Equipment*, 593(3):255–262, 2008.

[51] M. Ablikim et al. (BESIII Collaboration). Determination of the number of J/ψ events with inclusive J/ψ decays. *Chinese Physics C*, 41(1):013001, Jan 2017.

[52] B.F.L. Ward, S. Jadach, and Z. Was. Precision calculation for $e^+e^- \to$ 2f: the KK MC project. *Nuclear Physics B - Proceedings Supplements*, 116:73–77, 2003. Proceedings of the 6th International Symposium on Radiative Corrections and the 6th Zeuthen Workshop on Elementary Particle Theory.

[53] R.-G. Ping. Event generators at BESIII. *Chinese Physics C*, 32:599–602, 2008.

[54] A. Ryd et al. EvtGen: A Monte Carlo Generator for B-Physics. Jul 2007. URL https://docbes3.ihep.ac.cn/ offlinesoftware/images/6/6a/Guide_BesEvtGen.pdf (visited on 26.07.2021, 21:06 Uhr).

[55] S. Agostinelli et al. Geant4-a simulation toolkit. *Nuclear Instruments and Methods in Physics Research Section A: Accelerators, Spectrometers, Detectors and Associated Equipment*, 506(3):250–303, 2003.

[56] R.-L. Yang, R.-G. Ping, and H. Chen. Tuning and Validation of the Lundcharm Model with J/ψ Decays. *Chinese Physics Letters*, 31:061301, May 2014.

[57] R. Mitchell. The BESIII FSFilter Package, 2017. URL https://bes3.readthedocs.io/packages/analysis/FSFilter.html (visited on 26.07.2021, 22:28 Uhr).

[58] R. Aaij et al. (LHCb Collaboration). Amplitude analysis of the $B^+ \to D^+D^-K^+$ decay. *Physical Review D*, 102(11):112003, Dec 2020.

[59] B. Kopf, H. Koch, J. Pychy, and U. Wiedner. Partial wave analysis for $\bar{p}p$ and e^+e^- annihilation processes. *Hyperfine Interactions*, 229(1-3):69–74, Feb 2014.

[60] M. Albrecht, C. Amsler et al. (Crystal Barrel Collaboration). Coupled Channel Analysis of $\bar{p}p \to \pi^0\pi^0\eta$, $\pi^0\eta\eta$ and $K^+K^-\pi^0$ at 900 MeV/c and of $\pi\pi$-Scattering Data: The Crystal Barrel Collaboration. *The European Physical Journal C*, 80:453, May 2020.

[61] CERN. ROOT Reference Guide 6.07/01, Dec 2015. URL https://root.cern.ch/doc/v606/group__QuantFunc.html#gac0af234fc75caef88fcd6db900cb84e9 (visited on 26.07.2021, 20:22 Uhr).

[62] M. Ablikim et al. (BESIII Collaboration). Observation of $\eta_c \to \omega\omega$ in $J/\psi \to \gamma\omega\omega$. *Physical Review D*, 100:052012, Sep 2019.

[63] M. Ablikim et al. (BESIII Collaboration). Precision Study of $\eta' \to \gamma\pi^+\pi^-$ Decay Dynamics. *Physical Review Letters*, 120:242003, Jun 2018.

[64] D. Barberis et al. A coupled channel analysis of the centrally produced K^+K^- and $\pi^+\pi^-$ final states in pp interactions at 450 GeV/c. *Physics Letters B*, 462(3-4):462–470, Sep 1999.

Eigenständigkeitserklärung

Hiermit versichere ich, dass die vorliegende Arbeit *„Determination of the Branching Ratio of the Decay $\eta_c \to \eta' K^+ K^-$ and Search for Glueball Content in $K^+ K^-$ intermediate States at BESIII“* selbstständig von mir und ohne fremde Hilfe verfasst worden ist, dass keine anderen Quellen und Hilfsmittel als die angegebenen benutzt worden sind und dass die Stellen der Arbeit, die anderen Werken – auch elektronischen Medien – dem Wortlaut oder Sinn nach entnommen wurden, auf jeden Fall unter Angabe der Quelle als Entlehnung kenntlich gemacht worden sind. Mir ist bekannt, dass es sich bei einem Plagiat um eine Täuschung handelt, die gemäß der Prüfungsordnung sanktioniert werden kann.

Ich erkläre mich mit einem Abgleich der Arbeit mit anderen Texten zwecks Auffindung von Übereinstimmungen sowie mit einer zu diesem Zweck vorzunehmenden Speicherung der Arbeit in einer Datenbank einverstanden.

Ich versichere, dass ich die vorliegende Arbeit oder Teile daraus nicht anderweitig als Prüfungsarbeit eingereicht habe.

Münster, 27.07.2021 _____

Anja Brüggemann

Declaration of Academic Integrity

I hereby confirm that this thesis “*Determination of the Branching Ratio of the Decay $\eta_c \to \eta' K^+ K^-$ and Search for Glueball Content in $K^+ K^-$ intermediate States at BESIII“* is solely my own work and that I have used no sources or aids other than the ones stated. All passages in my thesis for which other sources, including electronic media, have been used, be it direct quotes or content references, have been acknowledged as such and the sources cited.

Münster, 27.07.2021 _____

Anja Brüggemann

I agree to have my thesis checked in order to rule out potential similarities with other works and to have my thesis stored in a database for this purpose.

Münster, 27.07.2021 _____

Anja Brüggemann